5-1-2023

Biological Neuron Voltage Recordings, Driving and Fitting Mathematical Neuronal Models

Jassem N. Bourahmah
Georgia State University

Biological Neuron Voltage Recordings Driving and Fitting Mathematical Neuronal Models

by

Jassem Bourahmah

Under the Direction of Andrey Shilnikov, PhD

A Dissertation Submitted in Partial Fulfillment of the Requirements for the Degree of

Doctor of Philosophy

in the College of Arts and Sciences

Georgia State University

2023

ABSTRACT

The manual process of comparing biological recordings from electrophysiological experiments to their mathematical models is time-consuming and subjective. To address this problem, we have created a *blended* system that allows for objective, high-throughput, and computationally inexpensive comparisons of biological and mathematical models by developing a quantitative measure of likeness (error function). Voltage recordings from biological neurons, mathematically simulated voltage times series, and their transformations are inputted into the error function. These transformations and measurements are the action potential (AP) frequency, voltage moving average, voltage envelopes, and the probability of post-synaptic channels being open. The previously recorded biological voltage times series are first, translated into mathematical data to input into mathematical neurons, creating what we call a *blended* system. Using the sea slug *Melibe Leonina's* swimming central pattern generator (CPG) as our circuit to compare and the source of our biological recordings, we performed a grid search of the conductance of the inhibitory and excitatory synapse found that a weighted sum of simple functions is required for a comprehensive view of a neuron's rhythmic behavior. The *blended* system was also shown to be able to act as rhythm directors like pacemakers and drivers of Dendronotus Iris swimming interneuron (Si) cells and was able to replicate the perturbations of biological recordings. After verification steps using different configurations, calculated mean and variance of rhythmic characteristics, as well as recordings created from data augmentation. The form of data augmentation introduced can be generalized to other biological recordings or any time series. With all these tools developed and expanding the parameter dimensions a hypothesis was posited that there is a contralateral electric synapse not previously included in the *Melibe* CPG model.

INDEX WORDS: Central Patter Generators, Neuron model, Melibe Leonina, Blended system, Error function, Synaptic models, Dendronotus Iris

Biological Neuron Voltage Recordings Driving and Fitting Mathematical Neuronal Models

by

Jassem Bourahmah

Committee Chair: Andrey Shilnikov

Committee: Yaroslav Molkov

Jordan Hamm

Sergey Plis

Electronic Version Approved:

Office of Graduate Services

College of Arts and Sciences

Georgia State University

May 2023

DEDICATION

I would like to dedicate this dissertation to my friends and family, without their love, support, and understanding I doubt I would have accomplished as much as I have. Thank you to my parents especially for being great role models of empathy, strength, and love.

ACKNOWLEDGEMENTS

I would like to acknowledge and thank my advisor and committee chair Dr. Andrey Shilnikov for his support and unquestionable belief in not only myself but my potential. I would also like to thank the other dissertation committee members: Dr. Yaroslav Molkov, Dr. Jordan Hamm, Dr. Sergey Plis for their time, patience, and feedback.

I would especially like to express my immense gratitude to Dr. Akira Sakurai who has been very generous with his time and experimental data. He has always been happy to answer my questions and explain his thought processes behind his experiments.

Finally, I would like to thank fellow members of the lab past and present: Deniz Alacam, Krishna Pusuluri, Huiwen Ju, Jack Scully, David Bloom, and Carter Hinsley.

TABLE OF CONTENTS

LIST OF TABLES

LIST OF FIGURES

LIST OF ABBREVIATIONS

AP: Action Potential

CPG: Central Pattern Generator

HCO: Half-Center Oscillator

PIR: Post-Inhibitory Rebound

3-CCN: 3-Cell Computational Network

Si: Swimming Interneuron

FTM: Fast Threshold Model

EI: Excitatory-Inhibitory

HH: Hodgkin-Huxley

TTX: Tetrodotoxin

ODE: Ordinary Differential Equation

CEF: Combined Error Function

AB: Anterior Burster

PD: Pyloric Dilator

LP: Lateral Pyloric

PY: Amalgamated Pyloric

BCI: Brain Computer Interface

ANN: Artificial Neural Network

SNIC: Saddle-Node on an Invariant Circle

MET: Minimum Error Time-series

1 INTRODUCTION

The dynamics involved in Neuroscience specifically the networks of neurons are complex and require new innovative methodologies to analyze and understand them. The complex dynamics seen in these networks of neurons are rhythmic. Neuronal behavior is seen in motor, sensory, and cognitive functions. One such behavior is rhythmic oscillations, and disruptions or non-normal behavior to these rhythms are associated with a number of brain disorders, namely Alzheimer's disease, Parkinson's disease, schizophrenia, epilepsy, and autism. Furthermore, sleep heartbeats, respiration, circulation, and locomotion like swimming, walking, and flying are all rhythms that are generated from networks of neurons [1-9]. Therefore, understanding the principles that generate the rhythms can offer hypotheses that could lead to treatments for these disorders. n addition to regulating motor movements, it has been suggested that transient forms of central pattern generators (CPGs) and their rhythmic patterns are involved in the functioning of the cortex [10].

Some neuronal networks create rhythms as an emergent behavior. In other words, rhythms are generated as a result of the interactions between the neurons in the networks as opposed to rhythms that rely on endogenous bursting neurons. These neurons create rhythms that go back and forth between a firing and quiescent phase when isolated from any input from other neurons. The study of emergent behavior has been the focus of studies currently. The importance of rhythms in various motor, sensory, and cognitive functions remain significant, irrespective of whether they originate from emergent or endogenous behavior [2].

These rhythm-generating neural networks are small biological neural networks called central pattern generators (CPGs) [1-3,7]. For example, the rhythms that control sleep, heartbeats, respiration, circulation, and locomotion such as swimming, crawling, walking, or flying originate

from CPGs [1-3, 6,7]. Bursting patterns like those seen in CPGs were also seen in disordered synchronization during epileptic seizures [11-13]. These CPGs are defined as small networks made of biological interneurons or motor neurons that create oscillations between an active action potential firing and a quiescent phase with the quiescent phase characterized by a lack of or minimal action potential firing. These interneurons of the CPG interact with each other for a CPG to create the different bursting biological rhythms mentioned.

1.1 Central Pattern Generators

Another important discerning feature of CPGs is that they create their rhythms in isolation from any external input, such as sensory feedback or from higher CNS levels [2, 14-22]. For instance, though a CPG can have a similar function its connectivity between its interneurons can be different from one species to another. However, even with varied connectivity, there are some connections between a small number of neurons that are always present [23]. Though the movement and internal patterns in invertebrates and vertebrates are sometimes dissimilar there are motifs that are believed to be shared. Therefore, the study of invertebrate CPGs, their operational mechanisms, and the creation of computational and mathematical tools to assist with the study of both will offer insights into vertebrate CPGs. Understanding these simple networks would be the first step to understanding more complex ones since there are preserved characteristics even between simple and complex CPGs.

There are two main parts of a CPG's behavior, the dynamical properties of the individual neurons and the dynamical properties of the synapses that connect them to one another. CPGs create many vital rhythmic motor behaviors, and the rhythms can be created by a minimal number of interneurons [1-3,7]. There is a consensus among researchers that though CPGs may not create their rhythms exactly alike they still have certain characteristics that are still seen in

both vertebrates and invertebrates [1, 2, 4, 5, 7, 8, 24-31]. The fact that these characteristics are preserved in both vertebrates and invertebrates indicates their evolutionary importance and the need to study the characteristics. Furthermore, creating tools that would help study and analyze them would assist in the quest of understanding the preserved characteristics of CPGs in vertebrates and invertebrates. The dynamic robustness of CPGs has recently been a topic of study in the field alongside whether a single CPG can generate multiple rhythms. The question of how multiple rhythms can be generated by a single circuit has been researched and shown to be possible through mathematical modeling and shown to also be true for biological CPGs. For the mathematical model, it was shown that with the proper stimulation a CPG can transition the CPG from one attractor rhythm to another, for example, the switching of gaits of horses from walking to trotting to canter to bound.

There are different types of CPG designs such as the pacemaker configuration which is characterized by an endogenous bursting neuron that directs the other neurons of the CPG which in turn can modulate the rhythm of the pacemaker neuron. Another type of CPG produces rhythms from a network of interneurons that do not burst isolation. Since there are no endogenous bursting neurons in this CPG type then the rhythm emerges entirely from the synaptic interaction between the non-rhythmic neurons, called emergent rhythms. These emergent rhythms in a CPG dictate how their target organ moves, such as the stride made by leg muscles. In the field of CPG research, the rhythms dictating these movements of organs are assumed that both invertebrate and vertebrate CPGs have generalized components, which can be functional or structural. Understanding these generalized components is a priority for researchers.

1.1.1 Half-Center Oscillator

Another type of CPG is known as a half-center oscillator (HCO) which is made of two neurons or groups of neurons that create an antiphase bursting because they reciprocally inhibit one another. In other words, when one of the neurons fires action potentials the other does not, and when the action potential firing stops the quiescent neuron begins firing action potentials. HCOs were first hypothesized to explain the rhythmic movements of flexion and extensor muscles on the limbs of mammals. Since they were first proposed HCOs have been found in many CPG rhythms such as the leech heart, lamprey, tadpole, zebrafish larvae, and sea slug swimming. Since HCOs are seen across a wide variety of locomotive organisms it points to the importance of HCOs in CPGs and their ability to create locomotive rhythms.

HCOs are seen in both invertebrate and vertebrate CPGs. HCOs were posited as the mechanism by which the extensor and flexor muscles in vertebrates interact to create limb locomotion. Furthermore, to create the locomotive rhythm of multi-limbed, multi-jointed limbs and multiple gaits of multi-limbed organisms multiple HCOs were combined by synaptically coupling the interneuron group of one HCO to another. Sometimes coupling them in a reciprocal inhibition configuration creates an HCO between HCOs [8, 14, 32-36]. Even with CPGs and HCOs being observed in organisms and modeled in mathematical simulations, the role of the synaptic dynamics on CPGs remains unclear [26, 37-41]. The emergent rhythms of CPGs and HCOs are still being researched using biological and mathematical methods [8, 9, 14, 28, 32, 34, 35, 36, 42]. Though HCOs are important to CPGs' production of rhythmic behaviors, a single HCO does not explain how CPGs create multiple rhythmic motifs which for instance explains the different gaits of vertebrates [43-45].

An HCO alone can be considered a kind of CPG. However, in the case of the sea slugs Melibe and Dendronotus' swimming CPG, many HCOs combine to create the rhythm for their lateral bending swimming. Therefore, gaining any insight into the mechanisms of how rhythms are generated in Melibe and Dendronotus will also give us an understanding of an essential component of CPGs, namely the HCO [8, 9, 14, 28, 32, 34, 35, 36, 42]. Another testament to the importance of HCOs is their widespread presence in diverse organisms even in both vertebrates and invertebrates [14, 31, 46-49].

The mechanisms of HCOs have been studied previously and have been shown to run on two principles, namely escape and release [50-56]. One neuron is inhibited until it escapes while the depolarized neuron releases the inhibited neuron. By using these two principles HCO models are developed. However, there are other factors at play in developing HCO models, such as whether the individual neurons are intrinsic bursters. Some CPGs such as those of Melibe and Dendronotus were found to be non-intrinsic bursters [36, 57]. As one interneuron of the Melibe CPG is inhibited its contralateral counterpart fires action potentials tonically. The assumption is that having a diverse combination of neurons with differing intrinsic combinations conserves energy more efficiently. This is because endogenous bursters might require more energy and complexity to transition from being quiescent to firing in isolation. HCOs consisting of non-bursters that are synaptically coupled have been shown to be theoretically possible.

By modeling HCOs from non-endogenous bursters previous studies have gone about creating non-bursters, modeling the synaptic connections, exploring how the characteristics of the non-bursters and synaptic connections affect the model HCO, finding the working range of HCO for two parameters, and toggling the HCO from quiescent to antiphase bursting through synaptic dynamics [58]. An HCO has also been shown to theoretically hold multiple rhythms if

the neurons are endogenous bursters [59]. All the rhythms produced are still bursting however they burst in a synchronized fashion or with slightly shifted phases [60]. There is another mechanism that assists in making an HCO, post-inhibitory rebound (PIR) [61-63]. This is the depolarization caused by the overcompensation of an inhibited cell after it ceases to be inhibited. This mechanism can make an intrinsic quiescent cell fire in the absence of any external excitation.

2 MELIBE LEONINA SWIM CPG

There are common dynamics shared in the motion between invertebrates and vertebrates, including humans, therefore study of the Melibe swim CPGs would give us insight into the mechanisms of human locomotion. Neurological disorders have been linked to the disruption of CPGs. Furthermore, vertebrates also have a similar forebrain circuit to invertebrates [64]. The simplicity of invertebrate CPGs offers an opportunity to study the rhythmogenesis of more complex vertebrate CPGs, like those of mammals. The level of complexity seen in vertebrate CPGs is higher than in vertebrates, however, the study of simple invertebrate CPG will give us a foundation for understanding complex ones in the future.

CPGs can be found throughout the nervous system whether in the spinal column of vertebrates, the brains of invertebrates, or the peripheral nervous system. Previous research has already shown that vertebrates and invertebrates share mechanisms to create rhythms [64]. Since the mechanisms are shared it can therefore be inferred that understanding the workings of simple CPGs will lead to insight into the more complex CPGs.

For example, invertebrate CPGs are simpler than mammalian CPGs in both their circuitry and the experiments required to study them. One CPG that is representative of the simplicity of invertebrate CPGs is the sea slug swim CPG. The initial assumption was because of the simple locomotion sea slugs use to swim than their CPG would reflect their locomotive simplicity [65]. This characteristic makes the sea slug swim CPG a prime candidate to start understanding simple CPGs and the first step in understanding complex CPGs. How to compare a sea slug's swimming locomotion to that of four-limbed mammalian locomotion may not be obvious, however, understanding how simple locomotion is generated will no doubt give us an understanding of more complex locomotion. There are several sea slugs that swim in a similar fashion and are

well-studied, such as Tritonia, Aplysia, Dendronotus, Clione, Lymnaea, and Melibe [35, 49, 57, 66-68]. The sea slug swims CPG chosen for this study is that of Melibe Leonina.

Melibe, like other sea slugs, swims by moving their body from side to in locomotion called lateral bending. As mentioned previously, lateral bending is a simple locomotion whose simplicity was believed to be reflected in its swim CPG's configuration [69]. Furthermore, since CPGs are an essential part of the nervous system then understanding them would lead to a better understanding of the underwriting mechanisms of the nervous system, much like how understanding CPGs that produce simple locomotion would allow us to comprehend CPGs that are responsible for complex locomotion like that seen in four-limbed mammals [24, 70-72]. CPGs are seen throughout the nervous system since they are the origins of biological rhythmic activity. Which is why they are unavoidable when studying locomotion.

Previously, three-cell networks were able to be configured to create multiple rhythms from a single network of a 3-cell computational network(3-CCN) [73]. This 3-CCN is a network of computational neurons coupled together by computationally modeled chemical and electrical synapses, with the chemical synapses being either excitatory or inhibitory. A 3-CCN with these chemical and electrical synapses was able to produce multiple distinct patterns. The goal of the research was to ascertain how the coupling configuration of the synapses in a 3-CCN affects its ability to produce multiple distinct patterns [74-76].

These networks were also put together in a way that resembles that of biological CPGs. As an obvious next step, CPGs consisting of four cells were studied. The biological examples of four-cell network CPGs were the crustacean stomatogastric ganglion (STG) [77, 78] and sea slug swim CPGs of Melibe Leonina and Dendronotus iris. Though it was later discovered that the Melibe swim CPG consisted of eight cells and the Dendronotus swim CPG of six cells. Though

the rhythms of CPGs might appear to be orderly and regular with little variation, they actually have been shown to create nonregular bursting patterns that are described as chaotic [79].

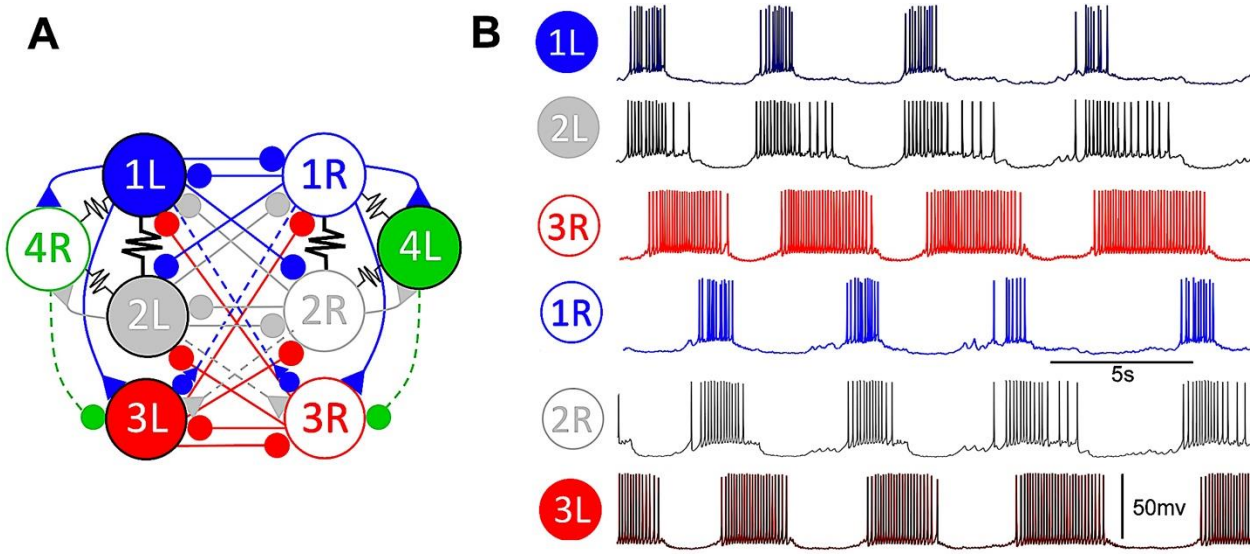

Figure 2.1 Biological recordings from Melibe electrophysiological experiments done by Sakurai. (A) Postulated circuitry of Melibe swimming CPG circuit grouped into the two neuron populations that make up the half-center oscillator (HCO), where R and L denote the right and left swimming interneuron, respectively. The first group consists of the first left swimming interneuron(1L), the second left swimming interneuron(2L), the third right swimming interneuron(3R), the fourth right swimming interneuron(4R), while the second group has their contralateral interneurons (B) Electrophysiological Voltage recording of Melibe swimming CPG neurons. Shows that the 1L, 2L, and 3R neurons have similar burst phases, 4R also has a similar phase but is not shown here. The dashed axons represent slowly activated synapses, the jagged lines the electrical synapse, and the solid synapse fast activated synapse.

It was originally believed that the Melibe swim CPG was made up of four neurons but was later found to have four more for a total of eight [33, 35]. Electrophysiological recordings and experiments gave researchers the evidence to diagram and map out the intrinsic nature and synaptic configuration of the Melibe swim CPG. Initially, the interneurons of the CPG were assumed to consist of tonic spikers and quiescent neurons, though it was later found to consist of only tonic spikers. The eight neurons are organized in four pairs with each neuron in the pair being contralaterally symmetrical in the Melibe brain. Each pair of contralateral have a

configuration of mutual inhibition between the pair, in other words, an HCO configuration. By definition, an HCO has the least amount of neurons and synaptic connections to be called microcircuits.

These four pairs of swim interneurons are labeled Si1 (swimming interneuron 1), Si2, Si3, and Si4 with each neuron of a pair being contralateral to the other in the brain (Figure 2.1A). For instance, the Si2s consists of the left Si2 (LSi2) and the right Si2 (RSi2) [36]. The Si pairs connect to each other through a combination of chemical and electrical synapses. The chemical synapses consist of both inhibitory and excitatory synapses. There are electrical synapses connecting the two Si1s to each other along with their mutual inhibition. In addition to the electrical synapses between Si1s, there are also electrical synapses between all Si1s and Si2s. Finally, there are electrical synapses between the Si4s and their contralateral Si1s and Si2s. For example, there is an electric synapse between the left Si4 (LSi4) and the right Si1 (RSi1) as well as between the LSi4 and the right Si2 (RSi2). Some of these electrical synapses are critical for the first steps of the mathematical modeling of the Melibe swim CPG.

The chemical synapses were also found to differ not only in terms of their neurotransmitter release but also in the relative speed at which the presynaptic release affects the postsynaptic interneuron. Furthermore, the intrinsic properties of the interneurons in isolation, i.e., tonic spiking or quiescent were also different. The circuit today came about after several adjustments to the configuration or the intrinsic properties of the interneurons because of new experimental results [65].

2.1 Melibe Leonina swim CPG models

Previously, the mathematical model of the biological CPG was reduced in complexity in order to ease the computational cost of simulating the mathematical model [63]. Because the

models were being developed alongside the biological the mathematical models were updated with the new findings of the electrophysiological experiments. When the modeling of the Melibe swimming CPG began there were no experiments showing the activity of the Si cells in isolation and were believed to be endogenous bursters. Though they were found to be nonendogenous bursters the mathematical CPG was able to generate similar rhythms to those seen in the biological CPG. In the next iteration of the model all the mathematical neurons were set to fire action potentials in isolation, i.e., tonic spikers. To connect the mathematical neurons fast-threshold model (FTM) synapses were used for simplicity and any changes between the synapses were in their conductance and reversal potentials.

2.1.1 Previous models

However, as subsequent electrophysiological experiments were conducted it became apparent that the Si cells differed in their activity in isolation [65]. Furthermore, it was found that the CPG consists of two HCOs bursting in antiphase though each has a different approach. In terms of the different activity of the Si cells in isolation, the electrophysiological experiments showed that one pair of Si cells were tonic spikers as previously set, however, the other was altered to be quiescent in isolation.

In addition to the model needing updating after the electrophysiological experiments, the simulations using the mathematical CPG could not accurately replicate the rhythms seen in the biological recordings. This inability to accurately replicate the biological rhythms was believed to be because FTM synapses were not sufficiently biophysically realistic. This led to a change in the synapses in the model. Since, the FTMs were binary and lacked any dynamics, meaning they were instantaneous in their change from being off or on, they were replaced with alpha synapses.

This replacement did lead to an improvement in the model's performance; however, more updates were needed after more experiments were done.

For instance, Si2s and Si3s were thought to have categorically different activity in isolation, however, both were found to be tonic spiking in isolation though they differed in spike frequency and inhibitory reversal potential. Specifically, Si3s were first thought to be quiescent in isolation.

2.1.2 Simplification of the model

As previously mentioned, the Melibe swim CPG is a network of biological neurons. Initially, the Melibe swim CPG was believed to be consisting of four interneurons that were designated into two contralateral pairs. However, later experiments discovered two new pairs of interneurons. Each of these pairs has shown to be mutually inhibitory between their contralateral counterpart, each of which can be hypothesized to be HCOs. The synapses that connected one pair to another were excitatory, electrical, inhibitory, slow, and fast. The electrical synapses connect the Si1s to ipsilateral Si2s, and contralateral Si4s. In addition, Si2s also electrically synapse to and chemically excite their contralateral Si4s. The Si1s also chemically excite their ipsilateral Si3s and contralateral Si4s. On the other hand, the Si2s excite the contralateral Si3s and Si4s. Furthermore, the Si1s have an atypical synaptic connection to their contralateral Si3s. This synapse has a biphasic postsynaptic response to the stimulation from the Si1s, meaning the Si3s initially become hyperpolarized and then become depolarized during the stimulation. The Si3s also inhibit their contralateral Si1s. As mentioned previously, the electrical synapses are critical for the first steps of the mathematical modeling of the Melibe swim CPG.

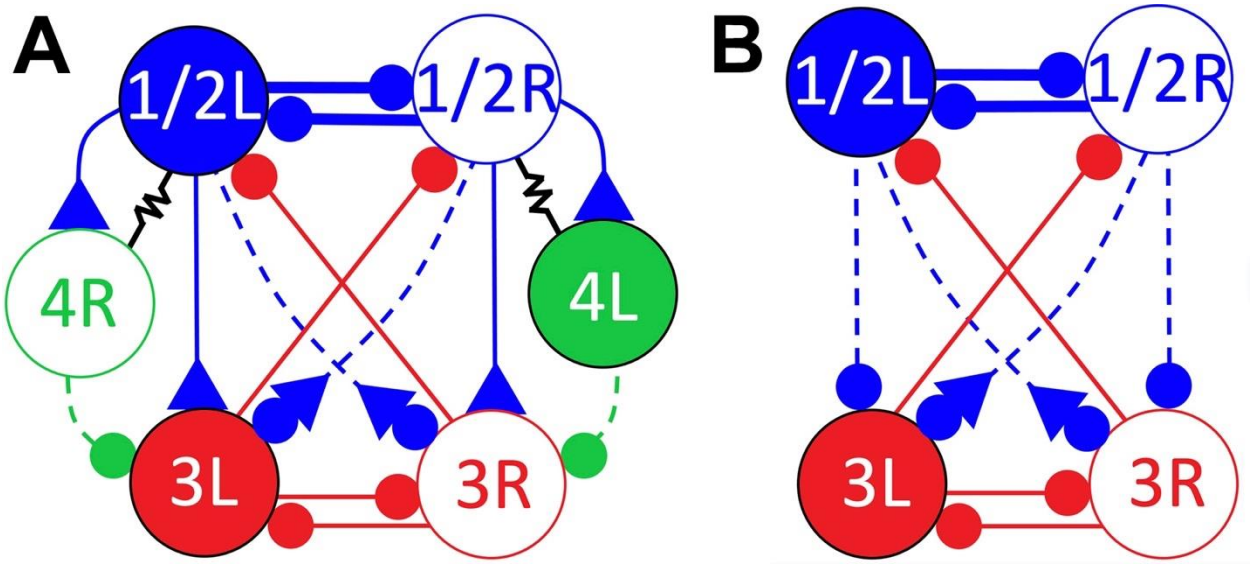

Figure 2.2 Simplification steps of Melibe swim CPG previously done by Alacam [1]. The left diagram (a) represents a reduced configuration of the ipsilateral interneuron 1 and 2 into a single neuron(1/2L,1/2R) because of their identical bursting phase. The right diagram (b) is reduced by replacing neuron 4 with a strong synapse also because of its similar bursting phase. The dashed axons represent slowly activated synapses, the jagged lines the electrical synapse, and the solid synapse fast activated synapse.

In previous studies, a reduction in the complexity of the Melibe circuit was posited since complexity made mathematical modeling more difficult [65]. This reduced mathematical model was done in two steps. The first step is merging the Si2s and their ipsilateral Si1s (Figure 2.2A). This is done because of the strong electrical synapses between them which results in them firing in phase of each other. This time however because the Si1s mutually inhibit each other, the same as the Si2s, when they are merged the mutual inhibition between the aggregate Si1/2 neurons was set to be three times stronger than they were before the merging.

Second, replacing the effect of Si4s on the CPG with a strong inhibiting synapse from their contralateral Si1/2s to their ipsilateral Si13s (Figure 2.2B). This is done because of the strong electrical and excitatory synapse between the Si1/2s and their contralateral Si4s. Also because the Si4s inhibit their contralateral Si3s. In terms of rhythmic behavior, the Si4s also

burst in phase with the Si1/2s, therefore the Si1/2s could be seen as indirectly synapse to their ipsilateral Si3s, which also causes a slowing of the synaptic effect. The indirect synapse, in-phase bursting, and electrical synapse lead the authors to replace the Si4s with a slowly growing and decaying synapse from Si1/2s to their ipsilateral Si3s. With this the eight-interneuron network is reduced to four; a pair of aggregate Si1/2 and a pair of Si3 cells.

This model was verified experimentally by comparing the effects of one variable that can be changed in the biological CPG and the mathematical model, namely the activity of cells [65]. Simulations showed that the strength of the inhibition between the amalgamated Si1/2s control burst duration, which was verified in experiments by suppressing Si1s decreases burst durations. Si1s suppression mutes the synapses between Si1s and their contralateral Si2s, this is equivalent to reducing the synaptic strength of the Si2s. Therefore, the experiments verified the mathematical model's assumption. One further step of simplification involves exposing the CPG to curare, but this will be expounded upon when the curare case is introduced.

2.1.3 Network Bursting

We briefly touched on the concept of network bursting as the hypothesis for the main mechanism of rhythmogenesis in the biological CPG. Some experiments were done that showed that perturbing the network changed the network's rhythm but did not stop the bursting from happening [65].

Previous work has shown how network bursting emerges, usually from tonic spiking cells [79]. Three mechanisms were found to generate and maintain network bursting in HCOs: post-inhibitory rebound (PIR), escape, and release. Post-inhibitory rebound we have already defined as a depolarization after inhibition from another neuron has ceased to inhibit which possibly causes an intrinsic quiescent neuron fire in the absence of any external excitation. PIR generates

a rhythm by sequentially rebounding the counterpart of one HCO neuron by inhibiting the counterpart, much like a perpetual motion machine. The escape and release mechanisms have also been discussed briefly as an inhibited neuron “escapes” its inhibition while the depolarized neuron releases the inhibited neuron. HCOs have been observed to be bistable, network bursters when the mutual inhibition is sufficiently strong, and initiating while maintaining network anti-phase bursting when the balance of initial phases must be fulfilled [80]. An HCO consisting of two tonic spiking neurons is bistable since the neurons can either tonically spike or network burst.

Another coupling configuration other than the mutual inhibition seen in HCO is that of the excitatory-inhibitory (EI) module [81]. In this module, a tonic spiking neuron excites a quiescent neuron that in turn inhibits the exciting tonic spiking neuron. This indirect negative feedback under certain conditions has been shown to create network bursting. However, both neurons can be tonic spiking if there is a balance between the initial phases and coupling strength, which is the same condition for a tonic spiking and quiescent neuron configuration. EI-modules were also found to be bistable, and their phase lag can fluctuate between one-quarter and one-half if the inhibitory synapse becomes more delayed. his configuration is also seen in Dendronotus iris with the addition of an electrical synapse between them. However, this configuration has not been seen in Melibe Leonina specifically. Though it could be present in an indirect manner as seen in the simplified diagram (Figure 2.2B), where the amalgamated can be the excitatory neuron and its contralateral Si3 neuron as the inhibitory neuron in an EI-module. However, there is no evidence of any electrical synapse between them, unlike Dendronotus iris swim CPG.

2.1.4 Plant model

To examine these different coupling configurations mathematical models were used and arguably could only be done using mathematical models. However, new mathematical and computational techniques are necessary to understand the many different types of behavior seen in biological neural networks. Mathematical models are one such tool that has long been used in many ways by different fields, from biology to computer science. Mathematical modeling has been done in biology since Fibonacci modeled the population growth of rabbits. Today, mathematical models have more complex and more accurate models for population dynamics in addition to creating models that assist in drug development, robotics, and neuroscience.

Mathematical modeling in neuroscience is used to help with the interpretation of experimental results as well as forming hypotheses that can be tested by biological experiments. One goal of our work is to create useful mathematical and computational tools that can be used to study neurons. Computational and mathematical tools are more time and cost-efficient methods than biological experiments, which can also be used to study and predict neuronal behavior.

To understand the generalized components of CPGs, modelers have used mathematical and computational techniques to discover and categorize the principles under which CPG networks work. Researchers elucidate the principles using test studies from experiments and models which have been key in unlocking CPGs' functional and structural components [15, 51, 82-86]. Mathematical models have been useful in gaining insight into the principles that all CPGs operate under. These mathematical models can be divided into the biophysically realistic and the phenomenological. The biophysical models describe the known molecular mechanisms

used in the neuron to recreate electrical activity, such as ion channel behavior. On the other hand, the phenomenological models simplify the activity to on or off [51, 82-84, 87].

To recreate the CPG of Melibe Leonina and Dendronotus iris initially a mathematical model that parabolically burst and endogenously burst was searched for. This was because the Si cells in the Melibe Leonina CPG were hypothesized to be endogenous bursters. Parabolic bursting is when the spike frequency at the beginning and end of the burst were lower than the middle. This led the researchers to the Plant model [88-90]. The model was created to simulate the R15 neurons in the abdomen of the sea slug Aplysia Californica and has been linked to their ability to lay eggs [91-97].

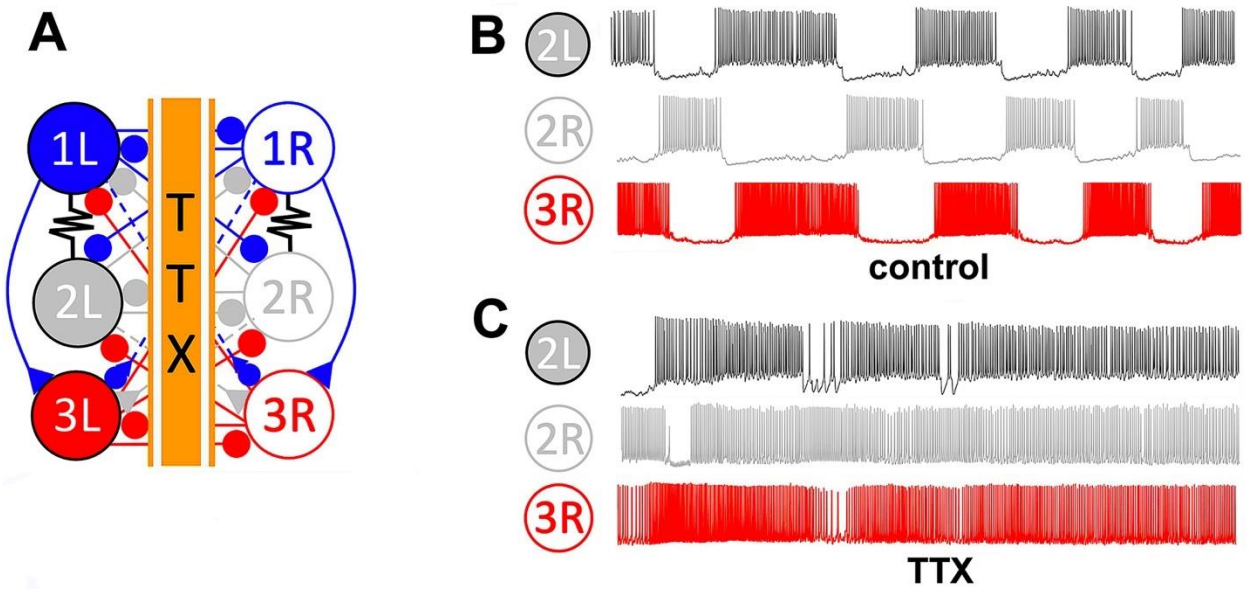

Figure 2.3 Melibe swim CPG using TTX on the axons crossing contralaterally in the pedal commissure showed that the Si cells were tonic spiking. (A) Diagram showing the synapses that were chemically lesioned using the sodium channel blocker tetrodotoxin (TTX). (B) Bursting shown in electrophysiological voltage recordings done on the Si2L, Si2R, and Si3R cells under normal conditions. (C) Loss of bursting and observed tonic spiking of isolated neuron shown in electrophysiological voltage recordings done on the Si2L, Si2R, and Si3R cells after TTX application to the pedal commissure where the axons project along.

The Plant model has been partitioned into a fast and slow component [90]. The fast component comprises the currents that are present in the original Hodgkin-Huxley (HH) model, namely the fast sodium-calcium inward, fast potassium, and a leak current. Specifically, the fast mechanisms responsible for the quick firing of action potentials are taken from the HH model. The additional currents placed into the slow component which differentiate the Plant model from the original HH model affect both the action potentials and the source of the action potential adaptation and voltage recovery needed for the endogenous bursting seen in R15 neurons. These currents are the tetrodotoxin (TTX)-resistant sodium-calcium inward and calcium-dependent potassium currents. TTX stands for neurotoxin called Tetrodotoxin that blocks sodium channels which are necessary for action potential and mostly responsible for the depolarizing current of a neuron. Therefore, any depolarizing current are from channels that are TTX-resistant. However, as previously stated, it was later found that the neurons in Melibe's swim CPG were not endogenous bursters. In other words, the neurons in Melibe's swim CPG did not burst independently. Furthermore, swimming interneuron (Si) cells were found to not burst in isolation and cannot burst when perturbed by a non-rhythmic external current making it a "latent" burster. This rhythmic characteristic was shown in TTX experiments using TTX on the axons crossing contralaterally in the pedal commissure of the Melibe swim CPG, the Si cells were found to be tonic spiking, even in the presence of a non-rhythmic injected current (Figure 2.3A). These findings then bring us to the previously stated understanding that the Melibe swim CPG is an emergent-network-level burster, meaning the bursting created by the swim CPG is achieved by the interaction between the Si cells, not any one interneuron (Figure 2.3B). The TTX experiments also showed that the action potential frequency in Si3 neurons is higher than in the Si2s.

To reiterate, the Plant model is an HH model with two additional currents, the original HH currents are categorized as fast components while the two additional currents are placed into the slow category [1]. In terms of the fast mechanisms, they are responsible for simulating a neuron's action potentials. Later the Plant model was modified to allow the neuron to switch between being an endogenous bursting, tonic spiking, or quiescent neuron, called an Si-model [65]. To modify the Plant model the dynamics of the slow currents were altered to prevent the model from bursting, whether endogenously or latently. Therefore, by definition, the Si-model either spikes tonically or is quiescent. To achieve this change in its dynamics two bifurcation variables were added [3]&[4]. Once this change is achieved and a network of Si-model neurons are connected to create a rhythm we can now say it is an emergent network-level rhythm. Furthermore, a tonic spiking Si-model only differs from a quiescent one in the intrinsic parameters and external perturbations from other mathematical neurons or externally applied currents.

The mathematical model we use for our neurons is the Si model, which is still a conductance-based Hodgkin-Huxley model [65]. The Si model and the original Plant model in terms of currents are identical. The model consists of an inward sodium and calcium (I_I), outward potassium (I_K), slow TTX-resistant calcium (I_T) and an outward calcium-sensitive potassium (I_{KCa}), and leak currents:

$$C_m \frac{dV}{dt} = -I_I - I_K - I_h - I_{KCa} - I_T - I_{leak} - \Sigma I_{syn}. \quad [1]$$

The h-current (I_h) is another depolarizing current that activates when the membrane voltage falls under -50mV. The h-current is added to this model to prevent the deep hyperpolarization that was observed in the Plant model. The I_{syn} is synaptic currents from presynaptic to the postsynaptic neurons.

The Si model makes its adjustments in the outward calcium-sensitive potassium current (I_{KCa}).

$$I_{KCa} = g_{\kappa Ca} \frac{Ca}{Ca + 0.5} (V - E_K), \quad [2]$$

The first bifurcation parameter (Δ_{Ca}) is added to the reversal potential for the differential equation of [Ca]:

$$\frac{d[Ca]}{dt} = \rho[K_c \, x \, (E_{Ca} - V + \Delta_{Ca}) - Ca]. \quad [3]$$

The second bifurcation parameter (Δ_x) is added to the steady state of the x gating variable:

$$x_\infty(V) = \frac{1}{1 + e^{-0.15(V+50-\Delta_x)}}. \quad [4]$$

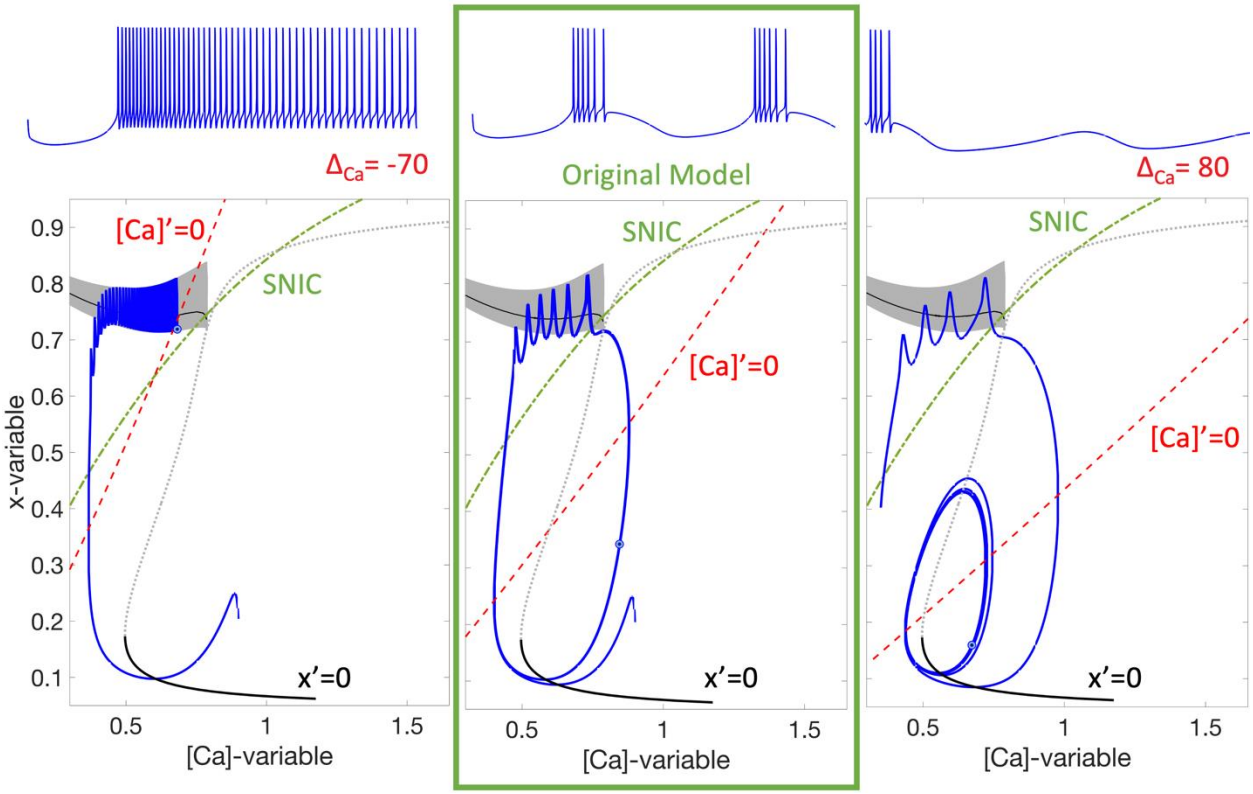

Figure 2.4 Si model phase space at x-shift = 0. 2 dimensional projections of a single modified Plant model neuron that is 6 dimensions. The calcium concentration is taken as the x-axis with the x-variable taken as the y-axis. These two variables were chosen for their close relation to the two added bifurcations parameters (x-shift and calcium-shift) in the modified Plant model and part of the slow subsystem of the model. The x-nullcline, seen in black, the calcium concentration nullclines, seen in red, and the saddle node on an invariant circle (SNIC) line in green show where the rate of change of a particular variable is zero. The calcium concentration nullcline which is the dashed red line is an attracting equilibrium and it intersects with the x-nullcline. The x-nullcline has different branches, the bottom branch illustrated as a solid black line is an attracting equilibrium while its grey dotted branch is repelling. The SNIC line, for the purposes of the plant model, separates where the model fires action potentials above the SNIC and is quiescent under the line. Above the SNIC the large grey area represents the projections of the periodic orbit manifold, the black line that runs through the manifold is average x along the periodic orbit. The bursting of the Plant model is due to the hysteresis which when the attracting lower branch of the x-nullcline overlaps x-average curve along the calcium concentration axis. A) When the calcium-shift is set to negative 70mV the slope of the calcium concentration nullcline intersects with the periodic orbit manifold projection and stays orbiting at the intersection of the calcium concentration nullcline and the x-average, resulting in a tonic spiker even when it starts as quiescent. B) In the original Plant model, the calcium concentration nullcline intersects the unstable branch of the x-nullcline this results in a trajectory of a bursting periodic orbit shown in blue. C) When the calcium-shift is set to 80mV the calcium concentration nullcline's slope decreases and edges close the bottom branch of the x-nullcline it begins subthreshold oscillating, and the trajectory never goes above the SNIC once it falls from above the SNIC.

Adding the two bifurcation parameters to the slow currents of the Plant model was to modify the slow dynamics and prevent it from bursting. Biologically, these bifurcation parameters are possible deviations of the reversal potential. For instance, Δ_{Ca} shifts the reversal potential of calcium, which can range from 80mV to 140mV. The Δ_{Ca}, Δ_x parameter area has been explored in a previous study [81]. Specifically, if the Δ_x=-2mV then the bursting of the model begins to be eliminated and only bursts when Δ_{Ca} is in a narrow range of [-45, -43] mV. Anything less than this range the model becomes a tonic spiker and anything above the range makes the model quiescent. As the Δ_x decreases the endogenous bursting is eliminated for all Δ_{Ca} values. Furthermore, to account for the difference in action potential frequencies of Si2s and Si3s their Δ_{Ca} was set to -44mV and -54mV, respectively.

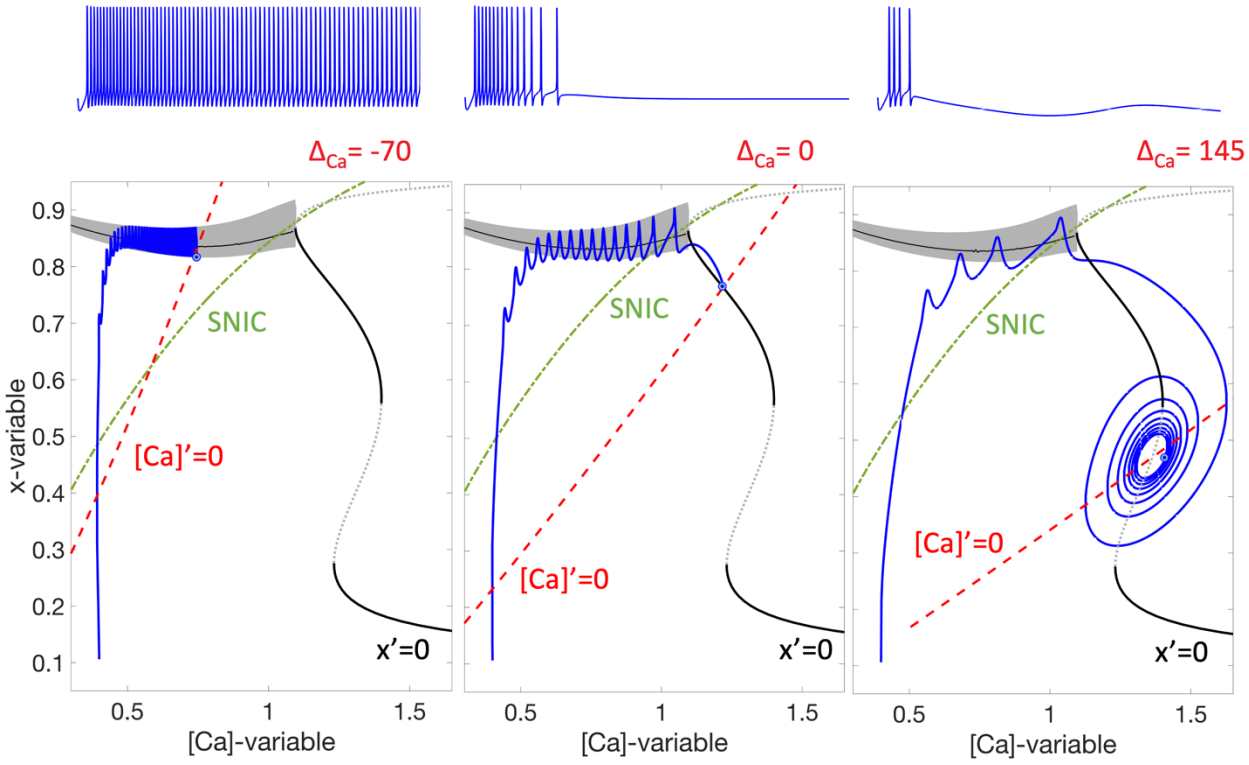

Figure 2.5 Si model phase space at x-shift = -4. 2 dimensional projections of a single modified Plant model neuron that is 6 dimensions, at x-shift = -4. The calcium concentration is

taken as the x-axis with the x-variable taken as the y-axis. Note the shape of the x nullcline when you set the x-shift to -4. The three changes of note are first the shifting of the intersection of the x average where the x nullcline moves up and to the right along the SNIC (dashed green line), second the appearance of another stable branch (solid black line) that begins at the intersection of the x nullcline and the x average, third the lower stable branch (solid black line) is moved to the right and no longer overlaps the x average. This lack of overlapping causes a loss of hysteresis and therefore a loss of bursting. This is apparent in the three phase planes shown with three different calcium-shift values. A) the phase plane when the calcium-shift is set at negative 70 again the neuron again becomes a tonic spiker though it is now in firing at a higher frequency. B) When the calcium-shift equals zero the calcium concentration nullcline intersects with the newly formed stable branch which results in a quiescent neuron even when it begins firing. C) The calcium-shift is set to 145mV and the calcium concentration nullcline now intersects with the unstable branch of the x nullcline leading to subthreshold oscillations even when it begins in a firing start point.

A single Plant model neuron is 6 dimensional in terms of the number of differential equations in the model. However, the dynamics of the whole system can be illustrated in the 2-dimensional slow system, namely by having the calcium concentration and the x variable as the two axes [81]. On the 2D plane, we plot the x-nullcline, seen in black, the calcium concentration nullclines, seen in red, and the SNIC line in green (Figure 2.4). The nullclines are simply the values at which the rate of change of a particular variable (in this case either the x-value or calcium concentration) these nullclines can either be stable or unstable in other words they are either attracting or repelling the system's state. The SNIC line stands for saddle node on an invariant circle, for the purposes of the plant model it separates where the model fires action potentials above the SNIC and is quiescent under the line. The center is the original Plant Model where calcium-shift and x-shift are both equal to zero. The calcium concentration nullcline which is the dashed red line is an attracting equilibrium and it intersects with the x-nullcline. At this point let me describe the different branches of the x-nullcline, the bottom branch illustrated as a solid black line is an attracting equilibrium while its grey-dotted branch is repelling. Also, above the SNIC, the large grey area represents the projections of the periodic orbit manifold, the

black line that runs through the manifold is average x along the periodic orbit. One last concept that is relevant is hysteresis which in simple terms is a system whose state depends on its history. In terms of the Plant model hysteresis is possible when the attracting lower branch of the x-nullcline overlaps the x-average curve along the calcium concentration axis. So, in the original Plant model the calcium concentration nullcline intersects the unstable branch of the x-nullcline this results in a trajectory of a bursting periodic orbit shown in blue. When the calcium-shift is set to negative 70mV the slope of the calcium concentration nullcline increases and intersects with the periodic orbit manifold projection. This causes the system to stay orbiting the intersection of the calcium concentration nullcline and the x-average, resulting in a tonic spiker even when it starts as quiescent. Now, when the calcium-shift is set to 80mV on the right, the calcium concentration nullcline slope decreases and edges close to the bottom branch of the x-nullcline, it then begins subthreshold oscillating, and the trajectory never goes above the SNIC once it falls from the x average.

The transformation of the shape of the x nullcline is what happens to the x nullcline when you set the x-shift = -4 (Figure 2.5). The three main changes are first the shifting of the intersection of the x average and the x nullcline moves up and to the right along the SNIC, second is the appearance of another stable branch that begins at the intersection of the x nullcline and the x average, third the lower stable branch is moved to the right and no longer overlaps the x average. This lack of overlapping causes a loss of hysteresis and therefore a loss of bursting. This is apparent in the three-phase planes shown with three different calcium-shift values, in the center when the calcium-shift equals zero the calcium concentration nullcline intersects with the newly formed stable branch which results in a quiescent neuron even when it begins firing. On the left phase plane when the calcium-shift =-70 again the neuron again becomes a tonic spiker

though it is now firing at a higher frequency. Now on the right, the calcium-shift = 145mV and the calcium concentration nullcline now intersects with the unstable branch of the x nullcline leading to subthreshold oscillations even when it begins in a firing start point.

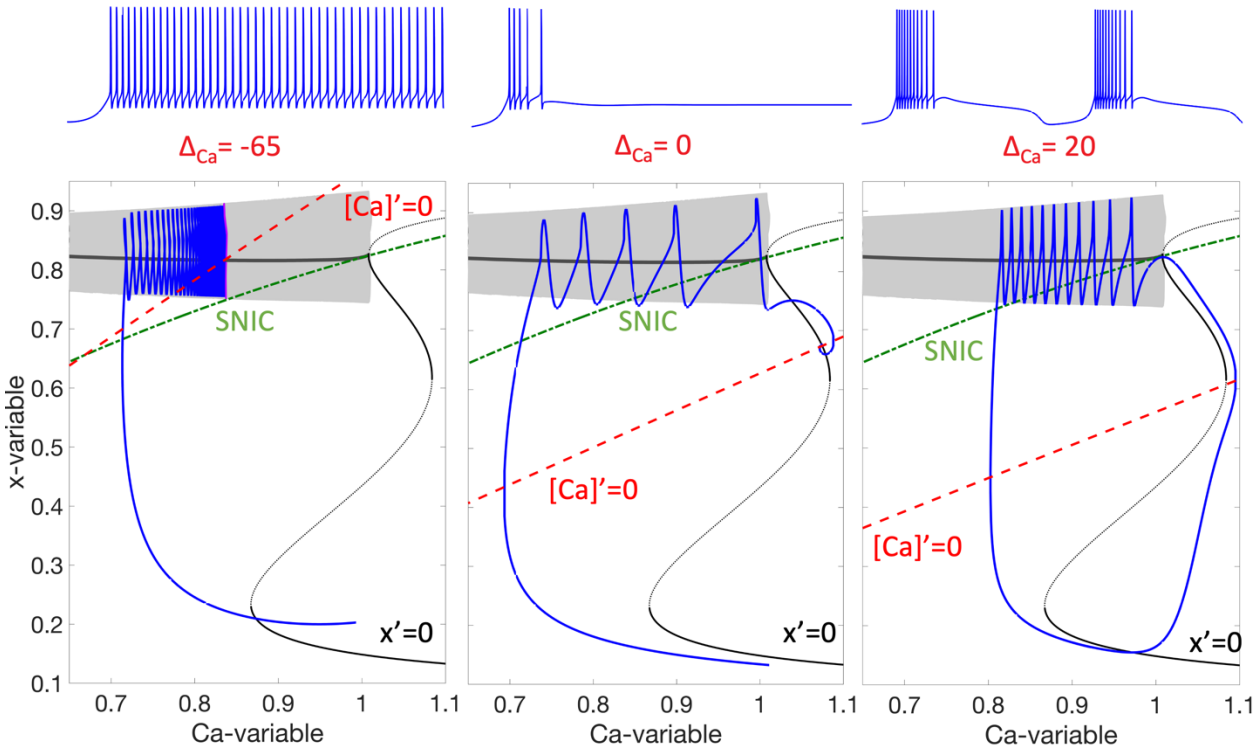

Figure 2.6 Si model phase space at x-shift = -1.7. 2 dimensional projections of a single Plant model neuron that is 6 dimensions, at x-shift = -1.7. The calcium concentration is taken as the x-axis with the x-variable taken as the y-axis. The x-nullcline, seen in black, the calcium concentration nullclines, seen in red, and the saddle node on an invariant circle (SNIC) line in green show where the rate of change of a particular variable is zero. At x-shift = -1.7 is an intermediate case where the x nullcline has an upper stable branch but the model still bursts. A) Shows a tonic spiker due to the calcium concentration nullcline intersecting with the x average both cases are like when x-shift = -4. B) The phase plane figure with the calcium-shift = 0 it intersects with the upper branch and reaches a quiescent stable state. C) However, unlike the x-shift=- 4 case when the calcium concentration nullcline intersects with the unstable branch of the x nullcline the neuron bursts and creates and a bursting periodic orbit. The bursting still happens here because the overlapping of the x average and the lower stable branch of the x nullcline allows for hysteresis to happen.

An intermediate case where the x nullcline has an upper stable branch but still bursts at x-shift =-1.7 offers an illustration of hysteresis (Figure 2.6). The middle phase plane figure with the

calcium-shift =0 intersects with the upper branch and reaches a quiescent stable state and the left figure shows a tonic spiker due to the calcium concentration nullcline intersecting with the x average both cases are similar to when x-shift =-4, however unlike when the x-shift =- 4 cases when the calcium concentration nullcline intersects with the unstable branch of the x-nullcline the neuron bursts and creates a bursting periodic orbit. The bursting still happens here because the overlapping of the x-average and the lower stable branch of the x-nullcline allows for hysteresis to happen.

2.1.5 Synapse model

Once the Si-model was appropriately configured the proper synaptic model was initially believed to be the FTM synapses. The FTM synaptic model simplifies the entire workings of a synapse into a current that instantaneously opens and closes dependent on the presynaptic membrane potential. Though there are benefits to using the FTM synaptic model such as simplifying the dynamics of the networks they have no temporal dynamics. Without these dynamics, it precludes any slow synapses and if slow synapses are needed for the proper function of a circuit, then FTMs will not be appropriate. These slow synapses were found to be in the biological Melibe swim CPG and were shown to be necessary for their rhythms. Specifically, the FTM synapses would work in a control case but not when the swim CPG was exposed to a curare bath. The curare and other experiments will be discussed later.

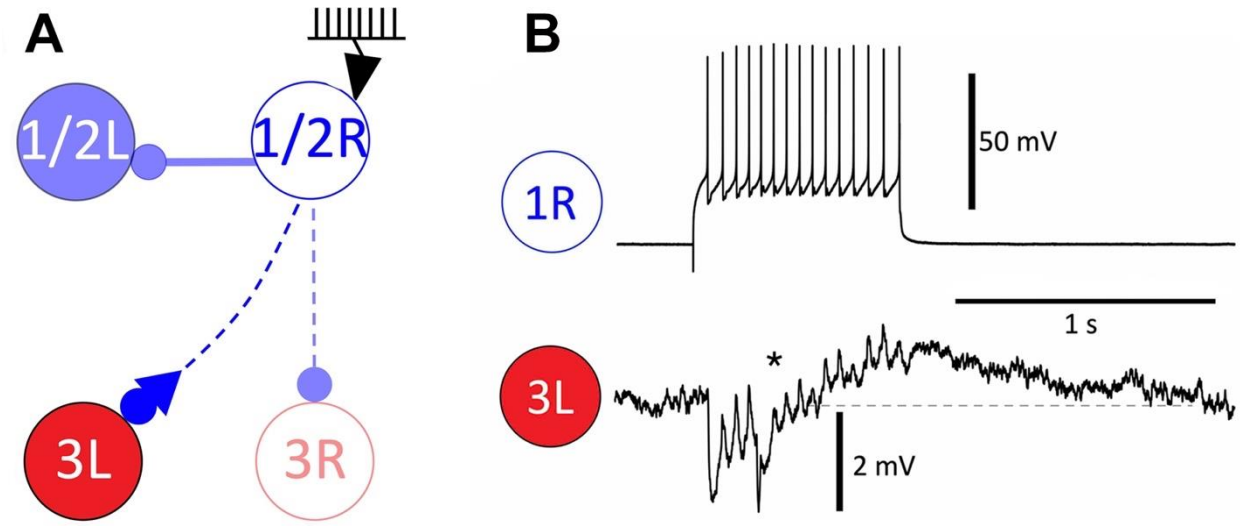

Figure 2.7 Observed biphasic synaptic response from a Melibe sea slug. (A) Diagram showing the experimental setup of stimulating the 1R neuron while recording the voltage of the 3L neuron. With the biphasic response being represented in the diagram as an inhibitory circle then an excitatory triangle terminal illustrating the biphasic response starts with an inhibition then excitation. (B) A stimulation that causes an AP frequency of 15 Hz, the 1R synapses to the 3L initially causes a hyperpolarization of 2mV, however, at around 0.25 seconds after the hyperpolarization the 3L neuron begins to depolarize by the 1R action potentials marked by the asterisk (*). Once 3L reaches its pre-perturbed voltage level (dashed line), it continues to depolarize.

However, the synaptic coupling from the Si1 cells to the contralateral Si3 cells in the Melibe swimming CPG is not a simple excitatory or inhibitory synapse. As mentioned previously, the synapse is dynamic with a biphasic response (Figure 2.7). This means that when the right Si1 fires action potentials this initially causes hyperpolarization in postsynaptic left Si3 then becomes excitatory so it's a mix of inhibition and excitation. To simulate a realistic synaptic variable the model synapse must meet specific requirements. The first property is summation which can be divided into spatial and temporal summation. The synaptic current and the key variable that differentiates it is the S variable. However, because of FTM's simplicity, it also is not dynamic, which prevents it from any summation.

To properly model the synaptic behavior of the Melibe swim CPG the FTM synapses were replaced with alpha synapses because they were more biologically plausible as well as slowly growing and decaying as needed to replace the slow indirect synapse from the Si4 to its contralateral Si3.

Here is the current equation for synapses:

$$I_{syn} = g_{syn}S(t)\big(V_{post}(t) - E_{rev}\big), \qquad [5]$$

Previous work found the dynamics in the Wang and Rinzel posited alpha synapse by making the S equation into a differential equation [51, 92].

$$\frac{\mathrm{dS}}{\mathrm{dt}} = \frac{\alpha(1-\mathrm{S})}{1+\mathrm{e}^{-\mathrm{k}(\mathrm{V_{pre}}-\mathrm{V_{th}})}} - \beta\mathrm{S}. \qquad [6]$$

Biologically, alpha corresponds to the strength of the binding of the neurotransmitters to the post-synaptic receptors. In contrast, beta corresponds to the combination of diffusion, enzymatic metabolizing or inactivation, and re-uptake into the presynaptic neuron of the neurotransmitters in the synaptic cleft. While the synaptic reversal potentials dictate whether the synapses are inhibitory or excitatory. For example, a synapse will be inhibitory when V (t) > Erev, or excitatory with V (t) < Erev. Therefore, setting the reversal potential less than the spike threshold the synapse will always be inhibitory and can be set to above a spike's peak to always make the synapse excitatory. Though this is a much more biologically realistic representation of the synaptic process, it does not offer a delay that would be necessary for a biphasic response seen in the CPG.

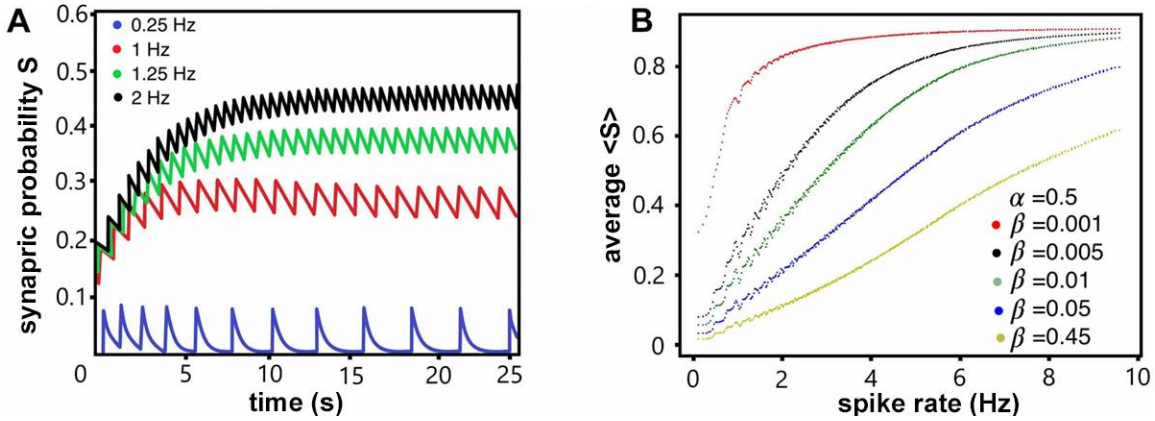

Figure 2.8 Setting up a mathematical synapse to simulate the neuromodulatory activity of the 2R neuron synapsed to the 3L neuron. (A) The stimulation frequency of 0.25 Hz is too low to accumulate in the synapse function but does begin accumulating at 1 Hz. (B) At α = 0.5 and β = 0.01, the S average begins to saturate at 9 Hz frequency stimulation and has a low S average at 2 Hz. This simulates the activity in figure 5B.*

The desired response of the average S to action potential frequency is a nonlinear one with an apparent inflection point. At low frequencies which include the beginning of an action potential train, the S average should be zero or near zero then increase and saturate in a sigmoidal fashion [98]. This ideal response is contrasted with the closest the alpha synapse can get to the shown ideal (Figure 2.8). This was done by sweeping different alpha and beta values and using a curve-fitting machine learning algorithm to find the optimum alpha and beta values that fit a logistic function with the shown maximum slope.

In search of a appropriate synaptic model to recreate the delay of a biphasic response, one further synapse is the dynamic synapse which was used to model facilitated synapses. This was done by presenting another variable M to the synaptic current:

$$I_{syn} = g_{syn}S(t)M\big(V_{post}(t) - E_{rev}\big), \qquad [7]$$

$$\frac{\mathrm{dM}}{\mathrm{dt}} = \left(\frac{1}{1 + \mathrm{e}^{-(\mathrm{V}+40)}} - \mathrm{M}\right)/\tau_M, \qquad [8]$$

where τ_M= 4000. The inserted variable M did allow the synapse to delay as well as potentiate.

However, because slow synapses operate secondary messenger cascades, they create a nonlinear relationship between the pre-synapse and post-synapse that possibly results in a nonlinear delay or high pass spike frequency filter. The logistic synapse was then created, named for its similarity to the logistic model of population and its sigmoidal shape [81]. This logistic synapse offers modelers the ability to have a nonlinear delay that can be used as a high pass filter. To produce a synapse with this, delay the solution was relatively simple in that we just multiplied the rising term by S which resulted in the very slow initial rise we were looking for.

$$S'(t) = \alpha\, S\,(1 - S)\, f_{\infty}\left(V_{pre}\right) - \beta(S - S_0), \qquad [9]$$

2.1.6 Control, curare, and TTX cases

There were three cases that were pivotal in furthering the understanding of the dynamics and rhythmic characteristics of the neurons and their synapses of the Melibe swim CPG. These cases were the control, curare, and TTX. The control case denotes voltage recordings that were taken when the CPG is in a saline solution. In this case, the Si2s and contralateral Si3s are phase locked. With a burst duration lasting 2-4 seconds. This is the case that FTM synapses were able to recreate. The final rhythmic characteristic of the control case is that there is a delay between the Si2s and contralateral Si3s.

The curare case is when the Melibe swim CPG is bathed in curare. Curare is a neurotoxin that can cause paralysis found in some south American plants. The distinguishing feature of curare is that it works only on cholinergic neurons, meaning neurons that release acetylcholine by working as a competitive acetylcholine antagonist. In the Melibe swim CPG, the Si3 cells are the only cholinergic neurons, therefore when the biological CPG is bathed in curare, the Si3 cells are not able to send synaptic signals but still able to receive signals. Experiments with curare

were done to take advantage of the fact that Si3s were the only cholinergic to further simplify and reduce the Melibe swim CPG. Furthermore, the resulting further simplified CPG (Figure 3.2A) still produces an anti-phase HCO even without the inhibition coming from the Si3s. Specifically, the reciprocal inhibitory synapses between the Si3s and the contralateral inhibitory synapses to the contralateral Si2s are muted (**Error! Reference source not found.**A). Now, we have a simplified Melibe CPG model, that is still able to produce an antiphase HCO rhythm.

The curare case is simpler since Si3s are muted then the Si1/2 amalgamated cells are solely responsible for the rhythm's generation in the CPG. The hypothesis therefore was that Si3s were simple followers of their contralateral Si1/2 amalgamated cells because of the excitation form the Si1/2 amalgamated cells to the contralateral Si3s. However, the HCO rhythm during a curare bath does have different characteristics from the control case. For instance, the burst duration of the CPG increases in curare from 2-4 seconds to 12-13 seconds. The burst duration is controlled by the Si2s, specifically it was found that it was controlled by their slow components and mutual inhibitory synaptic strength. In terms of the slow components influence on the burst duration because the slow components dictate the recovery period of a neuron going from quiescent to active. Additionally, the synaptic strength also affects the recovery period as was shown that with the increase of the synaptic strength the burst duration increases. However, once the inhibitory synaptic strength reaches a certain degree one cell completely inhibits the other.

Computational experiments showed that increasing the synaptic strength alone between the Si2s were unable to recreate a 2-4 second burst duration in the curare case [65]. Therefore, the CPG requires the contralateral inhibition from the Si3s (muted in the curare case) to Si2s to shorten the burst duration according to the computational models. This was also verified in

electrophysiological experiments that hyperpolarized the Si1 cells that resulted in the reduction of the burst duration. By hyperpolarizing the Si1s this is equivalent to reducing the synaptic strength between the Si1\2 amalgamated cells in the reduced model. Therefore, the electrophysiological experiments were in line with the computational models.

As previously mentioned, the curare case is also where the use of FTM synapses break down in their ability to recreate the rhythm. Namely, the slow synapse that replaces the slow indirect synapse from the Si4 to its contralateral Si3 cannot be an FTM synapse. FTM synapses cannot be slow since they lack any dynamics, in other words they are always fast. In terms of rhythmic behavior, the Si4s also burst in phase with the Si2s, therefore the Si2s could be seen as indirectly synapse to their ipsilateral Si3s, which also causes a slowing of the synaptic effect. The indirect synapse, in-phase bursting, and electrical synapse lead the authors to replace the Si4s with a slowly growing and decaying synapse from Si2s to their ipsilateral Si3s.

The third and final case of this section is the TTX experiment. In this experiment TTX was injected into the pedal commissure of the Melibe brain (Figure 2.3). The pedal commissure in the Melibe brain houses the axons that are crossing contralaterally to their Si counterparts. As previously mentioned, TTX blocks the depolarizing sodium-calcium current. This experiment essentially isolates all the Si cells and allowed previous modelers to correct the assumptions of their initial models. For instance, the Si cells were found to be “non-latent” bursters, meaning they do not burst in isolation or when perturbed by a constant current. Additionally, the endogenous state of the neurons was all tonic spiking. This result led to the realization that the Melibe swim CPG is an emergent-network-level burster, i.e., the CPG’s bursting rhythm is generated by the coordination between the Si cells, not orchestrated by one single endogenously

bursting neuron. Finally, it was observed that Si2s had higher action potential firing frequency than the Si3 cells from the TTX experiments.

3 BLENDED SYSTEM

To examine those CPGs that are multicellular new analytical tools were necessary to analyze the multidimensional problem of CPGs. By leveraging mathematical models many experiments on the mathematically modelled CPG can be done in a fraction of the time compared to biological experiment. These new tools should allow modelers to offer hypotheses from their analysis on the biological CPGs. Furthermore, as mentioned previously, the ability to change specific parameters are not currently possible or is prohibitively difficult to be done on biological models, mathematical models on the other hand can change parameters with relatively no difficulty. This therefore makes mathematical modeling necessary to the understanding of CPGs.

Modeling CPGs using mathematical techniques has been used to examine the emergent rhythms of the Melibe CPG. Specifically, to search for principles that can be generalized to all CPGs. The emergent behaviors of CPGs can be modeled using simple mathematical models. Furthermore, techniques have also been developed to identify these complex behaviors through bi-parametric sweeps. However, sweeping only two parameters is not ideal for systems as complex as a CPG. Nonetheless, sweeping more than two parameters comes with inherent difficulties namely being able to visualize or interpret the data. Another use of new tools would be for parameter optimization though using cost-function based parameter optimization requires an appropriate cost function, optimizing algorithm, and initial conditions. Nonetheless, these new tools can be used to creating biologically realistic mathematical models that recreate the rhythmic characteristics of the biological counterpart.

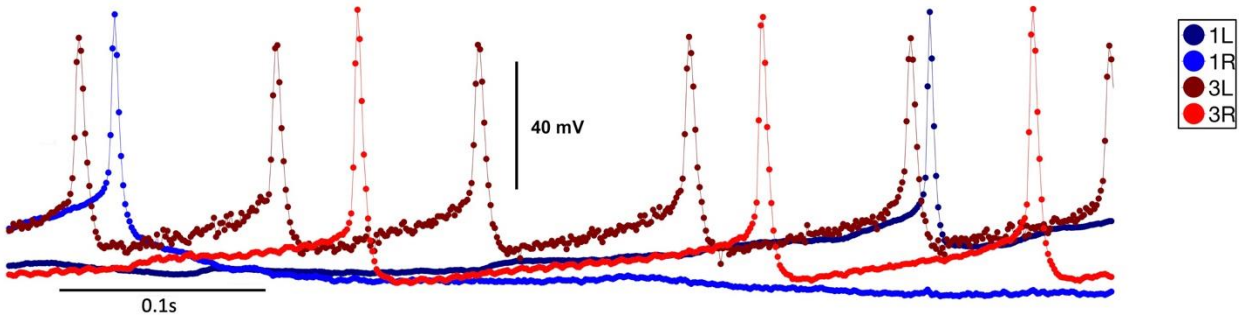

Figure 3.1 Converted electrophysiological recordings from Spike2 version 8 software. The recordings are subsequently made into a time-series figure (shown here). One vector is the time that each voltage sample was taken. For each time value there is a voltage value of the samples of the first left swimming interneuron (Si1L), first right swimming interneuron (Si1R), third left swimming interneuron (Si3L), third right swimming interneuron (Si3R), respectively. The sampling rate is also shown as 1.05 milliseconds.

3.1 Blended synapse

Comparing biological voltage recordings from electrophysiological experiments to the mathematical models that are attempting to simulate them when done manually can at best be time-consuming and worst subjective. To tackle the issue inherent in manual processing we posit a different type of system, called a *blended* system. The goal of this system is to allow for objective, high-throughput, and computationally expensive comparisons of biological and mathematical models. Using this *blended* system coupled with a quantitative measure of likeness (i.e., error or cost function) gives modelers the ability to examine the parameter space in an objective and automated process that is not computationally expensive or time-consuming. The inputs of the error function are measurements of the voltage recordings from biological Si cells, mathematically simulated voltage time series, along with their transformations. These transformations are the action potential (AP) frequency, voltage moving average, voltage envelopes, and the probability of open post-synaptic channels. The first step of the blending is the previously recorded biological voltage time series are translated into mathematical data via a synaptic model that are input into mathematical neurons (Figure 3.1).

Therefore, using the curare reduced model that is still able to produce antiphase HCO rhythms a *blended* synapse model is created. Recall that the curare reduced model "mutes" the Si3 cells in the Melibe swim CPG since the Si3 cells are the only cholinergic neurons in the CPG and curare works as a competitive acetylcholine antagonist (Figure 3.5A). At this point is where the methodology posited in this study differs from the past methodologies of computational neuronal modeling. The usual mode of operation would be to recreate the proposed 4-cell network by recreating four computational neurons and synaptically connecting in the same configuration which is what has been done previously with this model [32]. On the other hand, the methodology proposed in this study first takes one further step of simplification. This simplification is done by finding a way to translate the voltage values of a biological recording to a form that can be input into mathematical neurons. Biological voltage recordings are taken from the Si cells of Melibe's swimming CPG shown in (Figure 3.2A). To translate these recordings, we input the voltage values, into a synaptic function [6]. This can be done because the voltage recordings can be output and saved which in turn can be read by program functions. The synaptic function is the previously mentioned alpha synapses that simulate the synaptic output, in terms of the probability of post-synaptic channels opening, since it is a probability, it will be a value of 0 to 1. By input of the voltage recordings into the alpha synapse and integrating the equation, we have what we dubbed a *blended* synapse where the biological recordings are outputting computational synaptic probability (Figure 3.2C).

In other words, in a non-*blended* synapse (i.e., fully computational synapse) the presynaptic voltage (V_{pre}) [6] in a mathematical neuronal circuit would be from another mathematical neuron's voltage. However, the *blended* synapse replaces a mathematical neuron's voltage with the sequential voltage values from the biological voltage recording. The integrating

happens at each time step, for every sequential voltage value the synaptic equation is solved. This process will be given in more detail and discussed later. However, the parameters of the computational components for the *blended* synapse must be adjusted for the dynamics observed in experiments.

The dynamics here refers to the delay of the biphasic response seen between the Si2 and contralateral Si3 cell (Figure 2.7). As previously mentioned, the nonlinear relationship between the pre-synapse and post-synapse possibly caused by secondary messenger cascades results in a nonlinear delay or high pass spike frequency filter. This need for a high pass filter synapse brought about the creation of the logistic synapse, named for its similarity to the logistic population model's sigmoidal shape in relation to spike frequency. This logistic function can function as an alpha synapse but also has the ability for the synapse to delay the voltage.

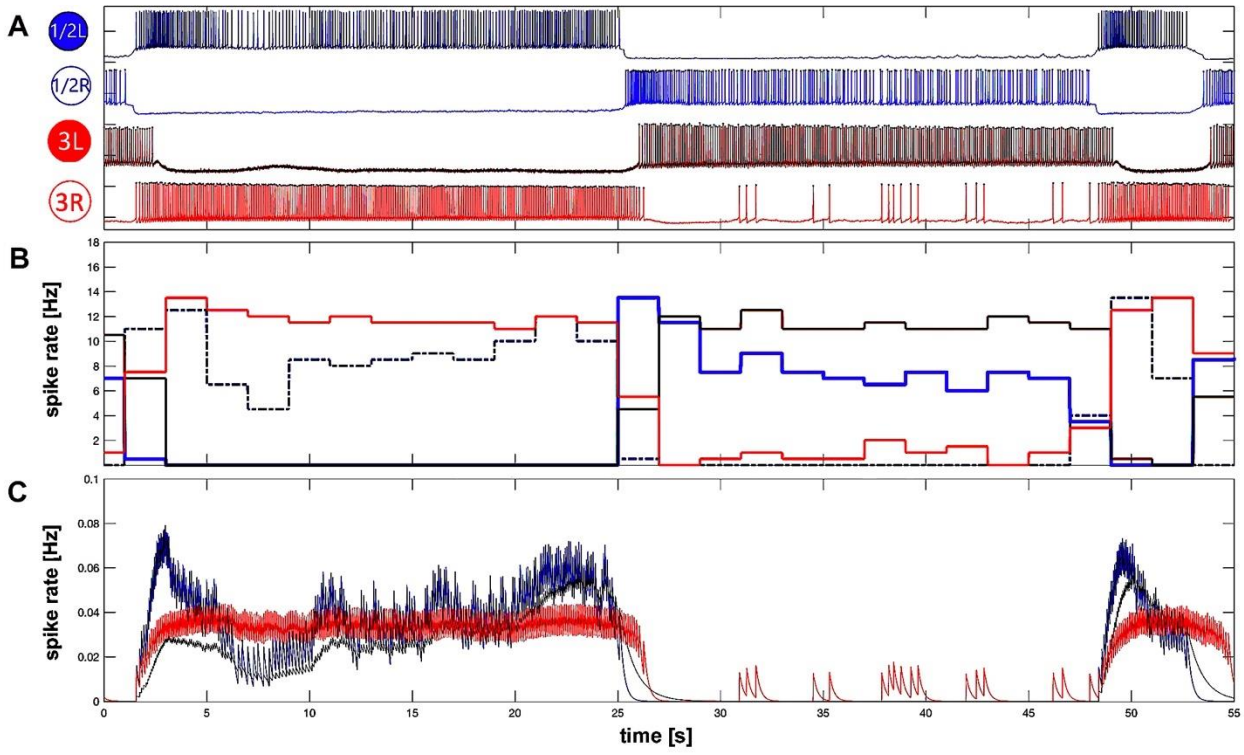

Figure 3.2 Blended synapse in curare bath: transforming the biological voltage recordings taken in curare bath to mathematical synaptic probability. (A) Previously recorded biological voltage recordings of 1L, 1R (which represent the voltages 1/2L and 3L), 3L, and 3R

in a curare bath. (B) Action potential frequency of the voltage recordings seen in (A). (C) The synaptic probability of 1/2R and 3R transformed from the biological voltage recordings in (A).

Now using the logistic synapses along with the synaptic blending, a CPG that is a mix of biological recordings and the Si-model mathematical neurons. When a network of biological recordings and mathematical neurons are connected to each other synaptically, said network we call a *blended* system. A diagram of the *blended* system when configured like that of the simplified Melibe CPG (Figure 3.3A). The configuration of the *blended* system is composed of two recordings of biological neurons (blue and shaded red circles) and two mathematical neurons (red circles). The biological neurons are illustrated as strongly mutually inhibited because they represent a neuron that is an amalgamation of Si1, 2, &4 nonendogenous bursting neurons that generate an HCO rhythm and are mutually inhibiting each other in each individual pair. The blue synapses that synapse to the mathematical neurons denote the *blended* synapse while the blue portions represent the biological recordings. These synapses represent the *blended* synapses that are translating the biological recordings into a synaptic input to mathematical neurons. As a reminder, the Si-model neurons are set as nonendogenous bursters or latent bursters. The mathematical synapses (blue synapses on math neurons) “project” from the two recordings of biological neurons (blue circles) onto the mathematical neurons, with triangle and circle synaptic terminals representing excitatory and inhibitory *blended* synapses, respectively.

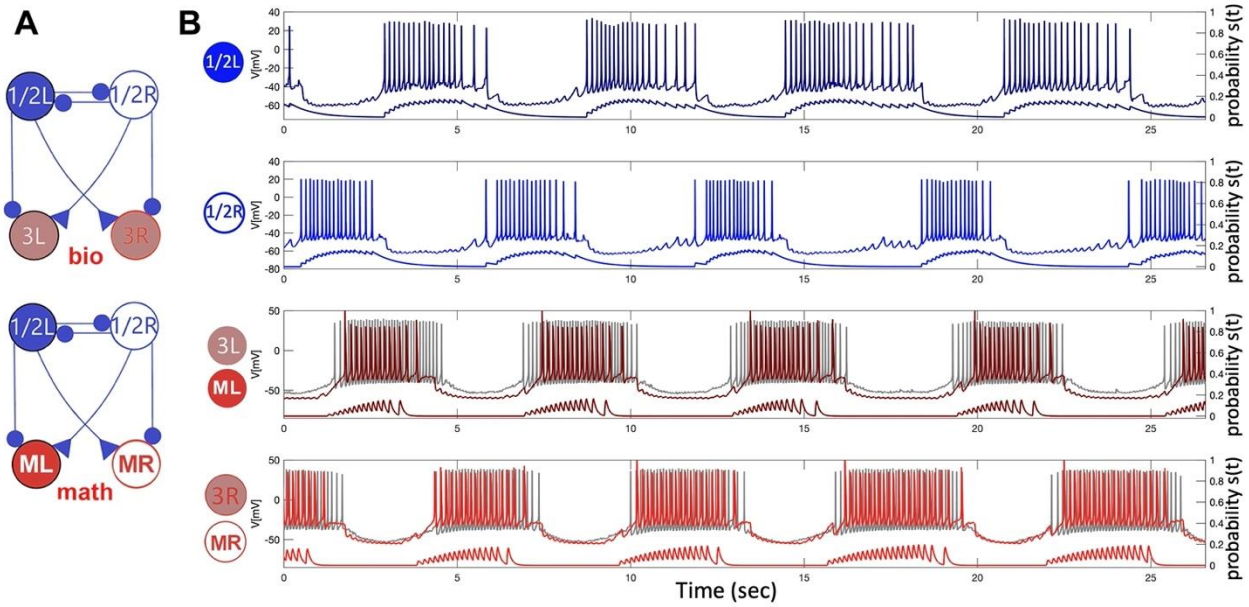

Figure 3.3 The 4-cell blended system with 2 bio and 2 math interneurons in normal swim. (A) The 4-cell swim CPG in a normal case and blended network where the biological bursters 1/2R and 1/2L project counter-laterally an excitatory dive and bi-laterally an exhibition resp., onto the interneurons 3L/R and the mathematical models ML/MR. (B) In vitro, strong inhibitory reciprocation between 1/2L and 1/2R electrically bonded into an HCO generating slow 12-14s bursting in the absence of feedback inhibition from 3L/R. An excitatory drive from the alternating bursters 1/2L and 1/2R makes the counter-lateral quiescent interneurons of both types follow, while the bilateral inhibition cuts them off into even spike trains. Superimposed underneath the biological traces are the corresponding synaptic probabilities emulated through [6]to model excitatory and inhibitory currents (via [5]) injected in the (red) mathematical neurons in the blended circuitry, whose traces (red) are overlaid with the biological originals (in grey).

The biological recording is also shown (Figure 3.3), seen in blue along with the translated synaptic probability in the same time series. The two-time series shown in grey are mathematical neurons after they were hand-tuned to create a mathematical voltage trace that passes the "eye test." The integration for the simulation of mathematical portions occurs in parallel to the biological recording (Figure 3.4). In other words, at each integration step, mathematical portions are updated with the biological voltage value of the corresponding time. When using this method, it is imperative to adjust the integration step as it should be equal to the sampling rate of the biological recordings, so they operate at the same "speed."

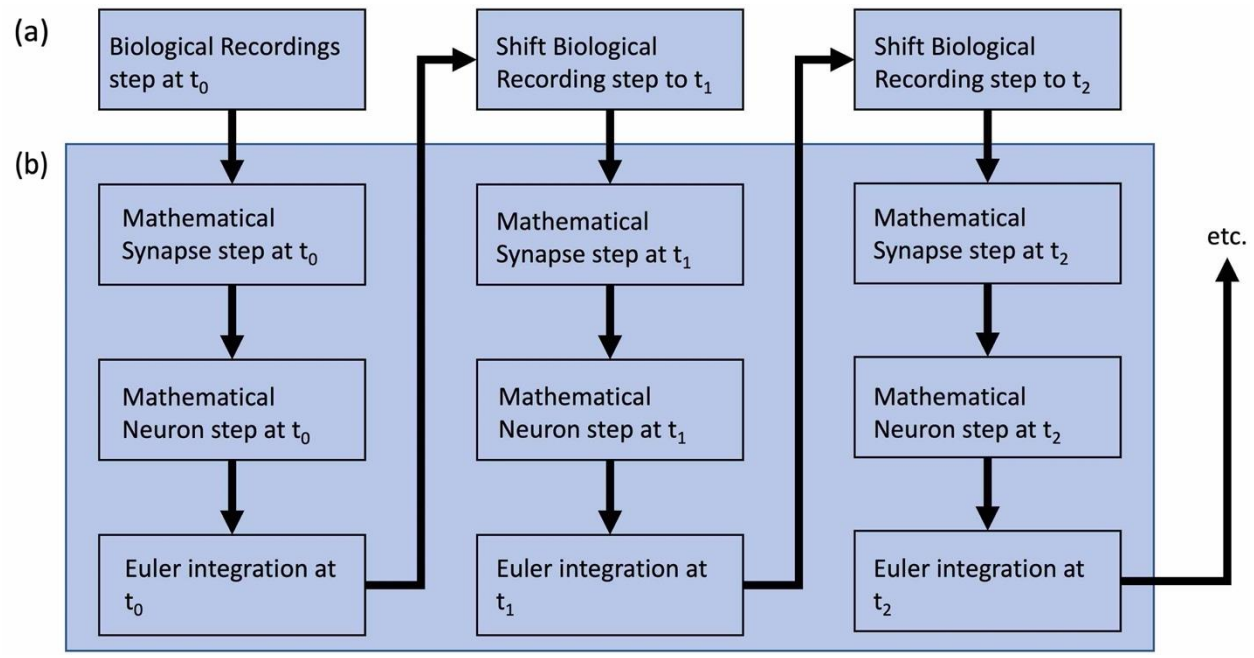

Figure 3.4 A flowchart of how a blended synapse and mathematical neurons are integrated simultaneously to create a blended system. (a) Shows the added step of shifting a predetermined biological voltage recording that is not part of a standard ODE solver. (b) The standard integration of a numerical integration algorithm.

Furthermore, the integration of the *blended* synapse must be done concurrently with the mathematical neurons to input the *blended* synapse current into the mathematical neurons. This simultaneous integration poses a problem for the standard functions that solve ordinary differential equations (ODEs) and are found in programming libraries. Those ODE solvers that are found in libraries cannot integrate a system while having a given variable that changes at every interaction outside the standard integration algorithm, in the case of this study the given variable is the biological recording, shown in Figure 3.4. An ODE solver integrates at each time step, beginning with an initial value. After the initial value, each subsequent time-integration step relies solely on the results of the previous time-integration step. However, the combined synapses integrate according to the results of biological recordings. This approach is comparable to setting an initial value at each time step.

To address this problem, an ODE solver was developed employing the iterative Euler method of integration approximation iterative method. At each cycle of integration, this ODE solver makes an approximation. Once one integration step is solved, the *blended* synapse integrates the mathematical neuron while simultaneously solving the *blended* synapse at the same integration step which follows the voltage time series from biological measurements in each consecutive iteration. When the *blended* system produces its voltage time series for the mathematical neurons, we can compare it to the voltage time series of the Si3L and Si3R cells, which are the biological neurons that the *blended* system is intended to imitate. The flowchart diagram in Figure 3.4 describes this procedure and illustrates the differences between the two ODE solvers.

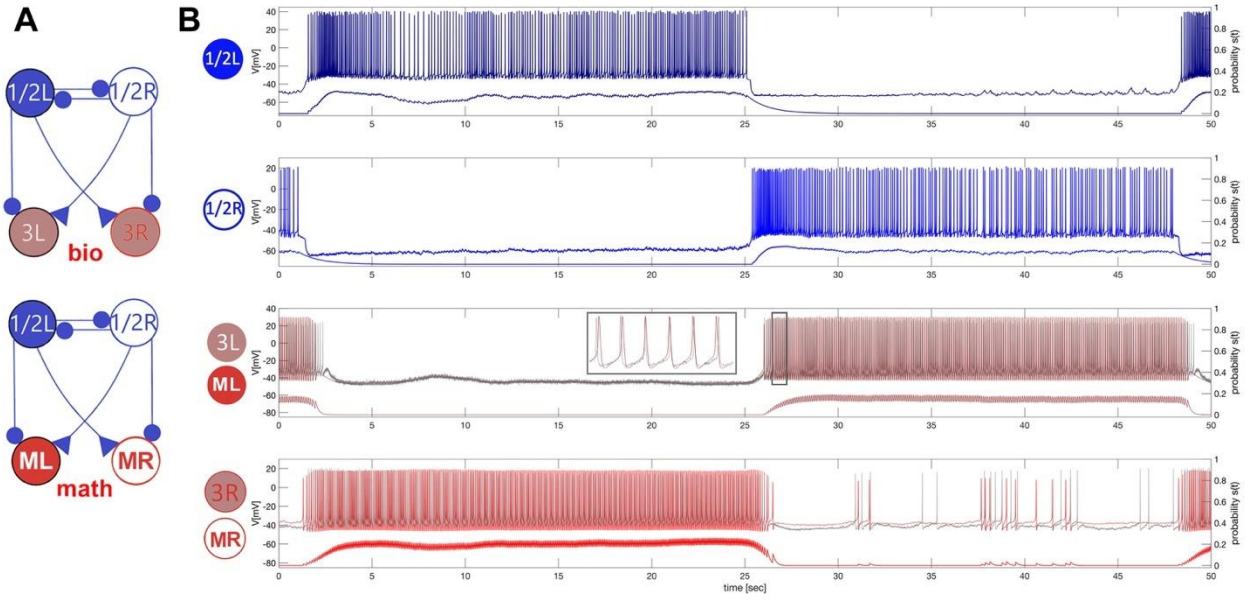

Figure 3.5 Superimposing mathematical traces onto the goal biological voltage recordings. (A) The 4-cell swim CPG in a curare bath and blended network where the biological bursters 1/2R and 1/2L project counter-laterally an excitatory dive and bi-laterally an exhibition resp., onto the interneurons 3L/R and the mathematical models ML/MR. (B) In vitro, strong inhibitory reciprocation between 1/2L and 1/2R electrically bonded into an HCO generating slow 12-14s bursting in the absence of feedback inhibition from 3L/R. An excitatory drive from the alternating bursters 1/2L and 1/2R makes the counter-lateral quiescent interneurons of both types follow, while the bilateral inhibition cuts them off into even spike trains. Superimposed underneath the biological traces are the corresponding synaptic probabilities emulated through

[6]to model excitatory and inhibitory currents (via [5]) injected in the (red) mathematical neurons in the blended circuitry, whose traces (red) are overlaid with the biological originals (in grey) .

Next, we move onto the *blended* system in the condition of curare bathe. To reiterate, the Si3 cells (red) in the Melibe swim CPG are the cholinergic neurons and therefore muted in curare. These Si3 cells are the neurons that the mathematical neurons are trying to simulate. A voltage time series of the biological Si3 recordings is superimposed on the mathematical neurons' voltage time series trying to emulate the Si3 cells Figure 3.5. From the temporal resolution shown in Figure 3.5 the two-time series appear to be good fits, the bursts begin and end at the same time, much like the normal swim condition it passes the "eye test." However, at a higher temporal resolution, you can tell that the action potentials do not align. This brings us to an important point and question. What dictates the similarity between these time series? What characteristics should we consider? The spike frequency of the action potentials? Their spike amplitudes or width? The synaptic probability? And what other characteristics and measurements should be considered?

4 ERROR FUNCTIONS

Initially, the S variable was used to compare the biological recording and the mathematical neuron that is trying to emulate it. To achieve this an objective function that can differentiate between the biological recording and the computational neuron was required, i.e., an error function. The error initially used is the Euclidian distance of the difference between the S variable of the computational neuron and the biological recording it is trying to emulate. An initial high throughput process for parameter optimization was also used.

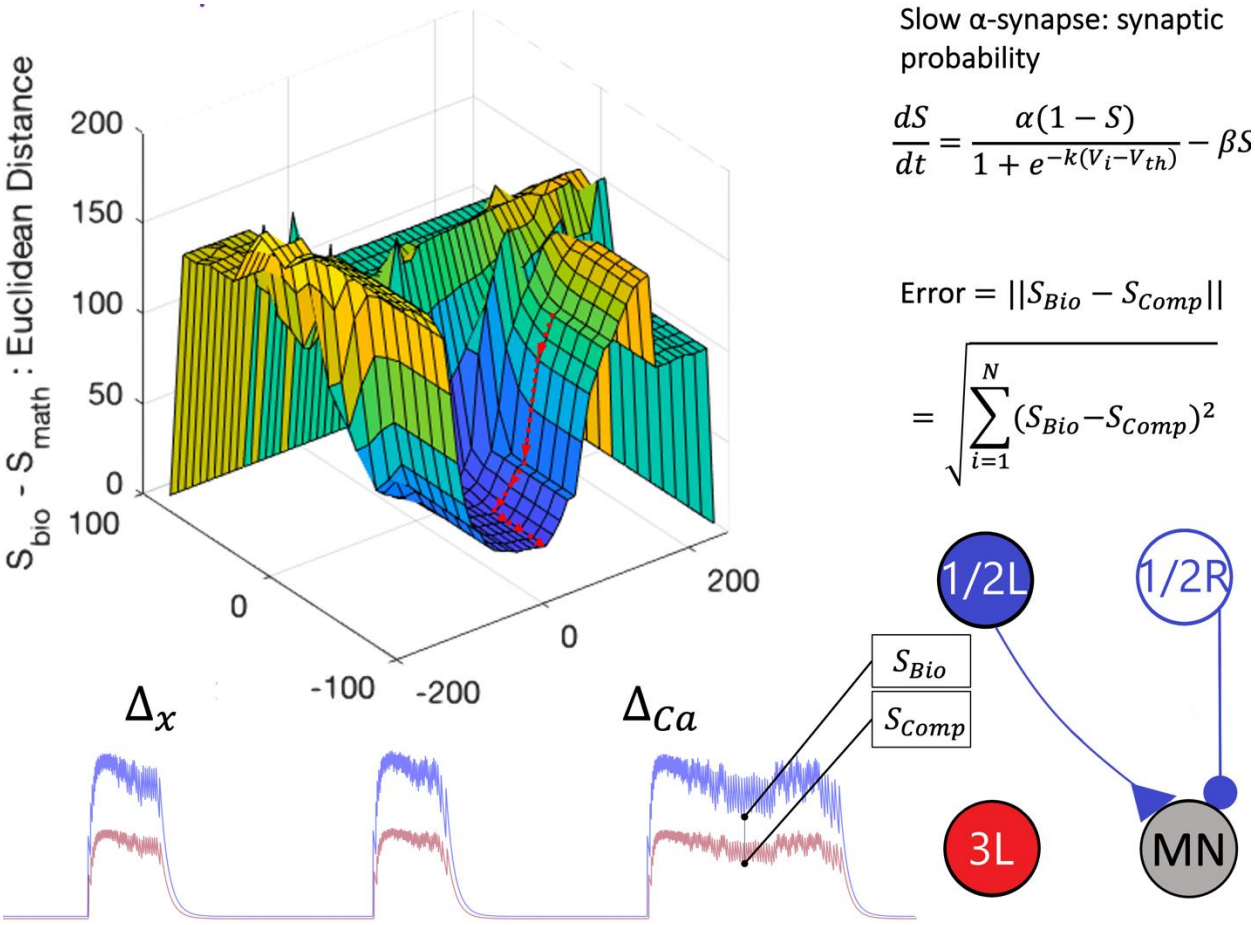

Figure 4.1 Figure showing the error space of the error according to the S variable distance, the calcium-shift, and the x-shift. The S variable distance is the Euclidian distance of the difference between the S variable of the mathematical neuron and the biological recording it is trying to emulate. An iterative optimization method called coordinate descent was used to optimize a mathematical neuron to emulate the biological recordings of a neuron in the Melibe CPG, namely a right SI3 neuron. This is done while blending the biological recordings to the

mathematical neuron. The descent is straightforward, a change of one parameter at an iteration and find the minimum value of the error while keeping the other parameters constant once the minimum error value of the changing parameter is found the same is done to the next parameter and find its minimum value and cycle through all the parameters until it converges to the minimum of the parameters. In this case the number of parameters is two, the calcium-shift and the x-shift. Therefore, once it finds the minimum it has found the parameter values that produce the least error. The limitations of this method of optimization are discussed in the text.

An iterative optimization method called coordinate descent was used to optimize a computational neuron to emulate the biological recordings of a neuron in the Melibe CPG, namely a right Si3 neuron (Figure 4.1). This is done while blending the biological recordings to the computational neuron that is attempting to be optimized using *blended* synapses seen in Figure 3.2. The descent is straightforward, you change one of the parameters at an iteration and find the minimum value of the error while keeping the other parameters constant, once you find the minimum error value of the changing parameter you switch to the next parameter and find its minimum value and cycle through all the parameters until it converges to the minimum of the parameters. In this case, the number of parameters was limited to two, the calcium-shift and the x-shift. Therefore, once the algorithm finds the minimum it has found the parameter values that produce the least error. However, this coordinate descent has some limitations one of which is that the objective function must be smooth, or it runs into the possibility of getting stuck in nonstationary points. And like other optimization methods, it runs the risk of settling in a local minimum rather than a global minimum if the error function is not convex. For instance, if the initial values for x-shift and calcium-shift are set to being outside this potential well there is no guarantee that it will find its way to the global minimum.

4.1 Transformations

So, the question is not only how we define similarity, but also how to ensure that there is a potential well that guarantees to settle at the global minimum. This characteristic is known as

convexity. In other words, what measurements should be used to differentiate one voltage time series from another that will also be convex? First, the options are limited since only voltage recordings are available, therefore, all the information must be either transformed or the original voltage time series.

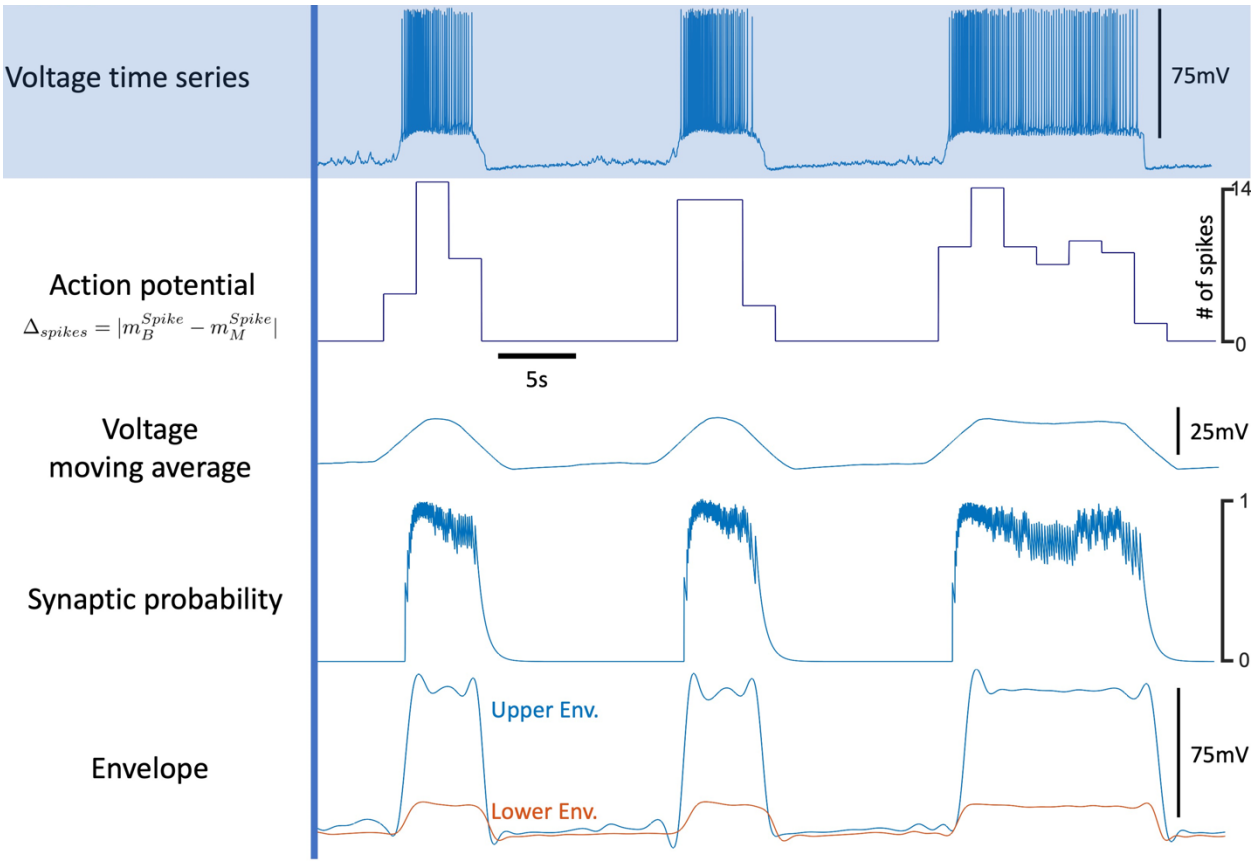

Figure 4.2 Transformations on voltage time series. At the top, the original recording of the voltage time series. Directly under the original recording is the first transformation, the action potential frequency count that counts the number of action potentials within a certain time frame. Next time series down is the moving average of the voltage. The result of the moving average smoothens the original voltage time series resulting in the loss of action potentials. Next is the synaptic probability that is a blended synapse S variable when transforming biological recordings and the S variable of the mathematical neuron. Synaptic probability like the voltage moving average smoothens the voltage time series though not to a similar degree. The final transformation is the Envelope function that outlines the signal and gives an upper and lower outline, spline interpolation over local maxima or minima. The envelope function is discussed in more detail in the text.

The original recording of the voltage-time series is shown in the first panel of Figure 4.2. The first transformation (Figure 4.2 second panel), is the action potential frequency count, which counts the number of action potentials within a certain time frame. Next is the moving average of the voltage (Figure 4.2 third panel), for those unfamiliar with moving averages, it is calculated by taking the average of a time frame and then taking the average of the next time frame which is a time frame shifted single step:

$$\hat{V} = \frac{1}{k} \sum_{i=N-k+1}^{N} V_i, \qquad [10]$$

As is evident, the result of the moving average smooths the original voltage time series (Figure 4.2 third panel). The most striking result of the transformation is the loss of action potential. Next is the synaptic probability that has previously been mentioned (Figure 4.2 fourth panel), this is basically a *blended* synapse S variable when transforming biological recordings and the S variable of the mathematical neuron. Synaptic probability like the voltage moving average smooths the voltage time series though not to a similar degree. The last transformation is the envelope function (Figure 4.2 fifth panel), the main function of this transformation is to outline the signal and it gives you an upper and lower outline, using spline interpolation over local maxima or minima. A spline is a piecewise polynomial, which is a polynomial that has different definitions at different intervals. Interpolation, for the uninitiated, is a type of estimation that finds new data points based on a set of known points in our case these known points are the local maxima or minima. For example, when there are action potentials firing, the envelope function will connect the top of one action potential to another. Resulting in the outline shown (Figure 4.2 fifth panel).

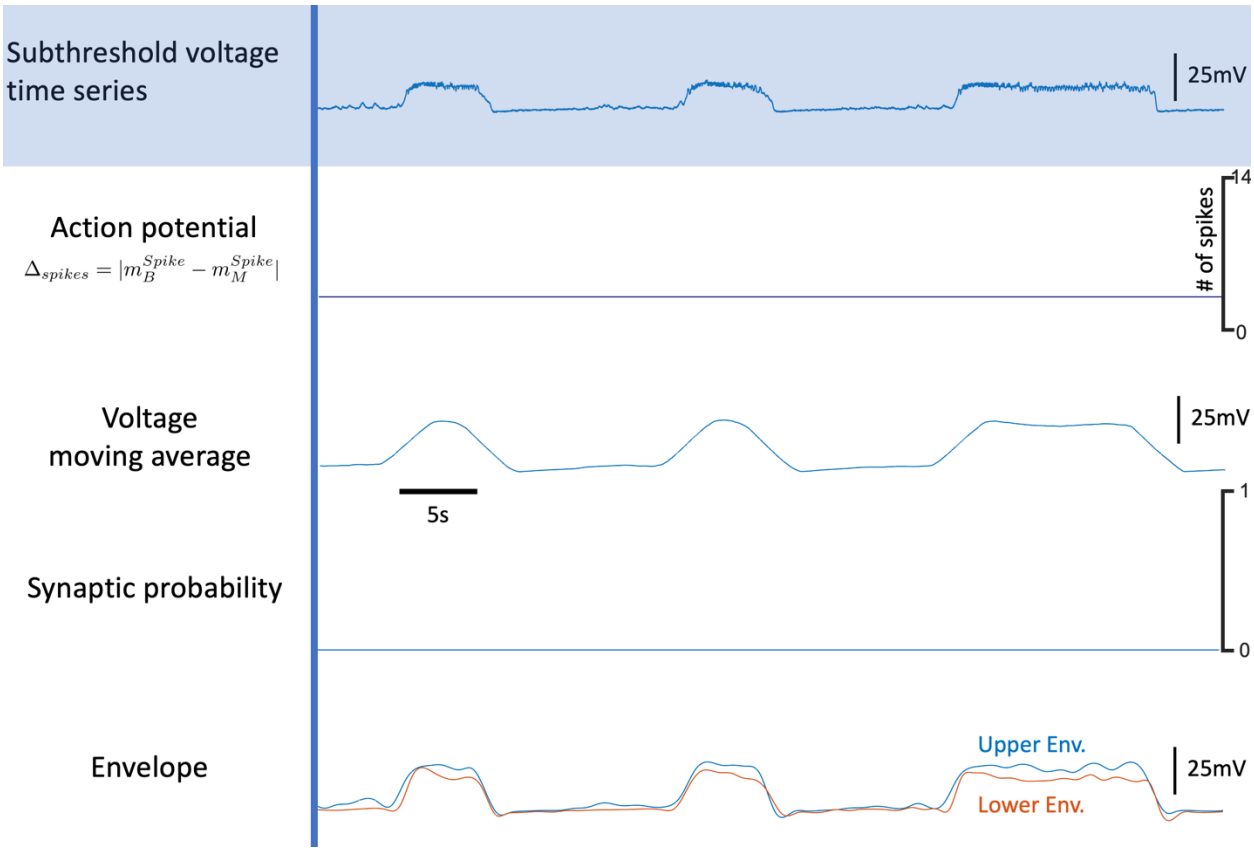

Figure 4.3 Transformations on voltage time series with no action potentials. Shows the limitations and information missed by the transformations. At the top, the original recording of the voltage time series that does not have action potentials. Directly under the original recording is the first transformation, the action potential frequency count that counts the number of action potentials within a certain time frame and does not differentiate between subthreshold oscillations. Next time series down is the moving average of the voltage. For this time series the moving average voltage has no action potentials to smoothen. Next is the synaptic probability that is a blended synapse S variable when transforming biological recordings and the S variable of the mathematical neuron. Synaptic probability like action potential frequency does not differentiate between subthreshold oscillations. The Envelope function that outlines the signal and gives an upper and lower outline, spline interpolation over local maxima or minima appears to be able differentiate between the two relatively easily. The envelope function is discussed in more detail in the text.

However, these transformations have inherent limitations. Specifically, there is a loss or missing of information because of the transformation. To first illustrate these limitations, we observe their effect on a different voltage time series. This times series only has subthreshold oscillations, in other words, there are no firing action potentials (Figure 4.3 first panel). Each

evidently show a loss of information, especially the action potential frequency and synaptic probability transformations (Figure 4.3 second and fourth panel). The voltage moving average transformation though not as obvious also missed information and will be discussed in more detail later (Figure 4.3 third panel). Similarly, the envelope transformation appears to be able to a good candidate for an error function, but this claim does not stand up to scrutiny as will also be shown (Figure 4.3 fifth panel).

Let us begin with how to investigate the transformations and compare the transformations of the biological voltage recordings with its corresponding mathematical neuron time series. To change the mathematical neuron two parameters were swept, the conductance of the contralateral excitatory and ipsilateral inhibitory *blended* synapses seen in the simplified diagram Figure 3.5A. Each of these coordinates represent the conductance of the synapses on the x and y axes with their respective value in terms of the error function used on the z axis. In other words, for each point a simulation is run where the biological recordings of the Si1 cells are inputted into the mathematical neurons via *blended* synapses at their respective conductance and have a certain error value for the difference between the Si3 neurons and the mathematical neurons that are trying to emulate them. For all the figures in (Figure 4.4Figure 4.8) with each point of the figures using the same biological recording, in other words all the mathematical recording are being compared to one biological recording. The first error function (Figure 4.4) used to measure the difference between the two times series was the action potential frequency count. With this function the absolute value of the action potential count within a certain time frame of the biological recording is subtracted by the action potential frequency count of the corresponding mathematical neuron. Next the moving average voltage and calculated the L2 norm difference between the biological and mathematical voltage average was used (Figure 4.6). The L2 norm or

Euclidean norm is the square root of the sum of squares of the coordinates of a vector. In this case, the moving average voltage difference between biological and mathematical is the vector. The third function (Figure 4.7) also used the moving average voltage difference; however, it measures the variance of the difference's absolute value. The fourth function (Figure 4.5) like the second takes the L2 norm difference between the biological and mathematical but uses their synaptic probability. The fifth and final function (Figure 4.8) uses the envelope function and takes the L2 norm difference of the lower envelope and adds the L2 norm difference of the upper envelope then apply the sigmoid function to them. A sigmoid function is a function that has a characteristic S shape curve. Note that the figures don't seem to be similar, so they are each capturing different rhythmic characteristics that are not equivalent. Therefore, different information is being measured in each case.

4.2 Individual Error Functions

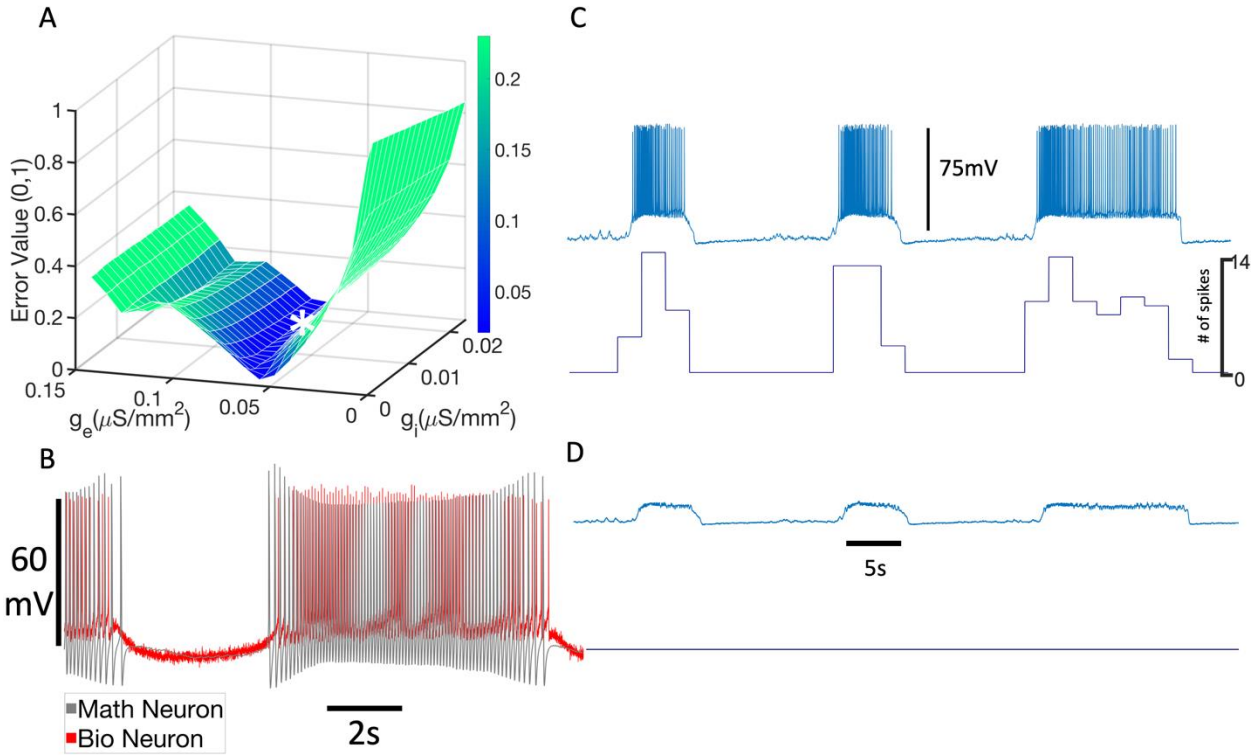

Figure 4.4 Error space of action potential frequency and the limitations of its respective transformation. A) The error with the excitatory and inhibitory conductance parameter space. The minimum error time series' (MET) value in the excitatory and inhibitory conductance parameter space is shown by the white asterisk (g_i = 0.0171, g_e = 0.0711). B) The mathematical neuron's MET (in grey) is juxtaposed over the corresponding biological recording (in red) it is meant to simulate and shows a similarity. C) The time series where the action potential frequency works as a transformation. D) However, when the action potentials are removed from the voltage times series the limitation of the action potential frequency error function is revealed. The transformation cannot differentiate between various "inactive" phases.

Nonetheless, the different information being measured by each of the transformations show benefits as well as limits. Beginning with the action potential frequency (Figure 4.4), with the minimum error shown by the white asterisk in the excitatory and inhibitory conductance parameter space. In other words, it is the trace with the least error and therefore the most similar according to the action potential frequency error function. The mathematical neuron's voltage times series (in grey) is shown juxtaposed over the corresponding biological recording (in red)

that it is meant to simulate and shows a similarity. The time series that the action potential frequency works is shown in (Figure 4.4C), for each time interval in the voltage time series with action potentials they are counted. However, suppose the action potentials are removed from the voltage times series as seen previously (Figure 4.3 first panel) and shown in (Figure 4.4D). The removal of action potentials reveals the limitation of the action potential frequency error function. Any change in the voltage under threshold is completely missed (Figure 4.4D), which is expected since this error function counts action potentials and action potentials don't fire under threshold. Resulting in an action potential frequency transformation that is flat even when there is a subthreshold burst of activity in the voltage time series. Meaning the transformation cannot differentiate between any inactive phases.

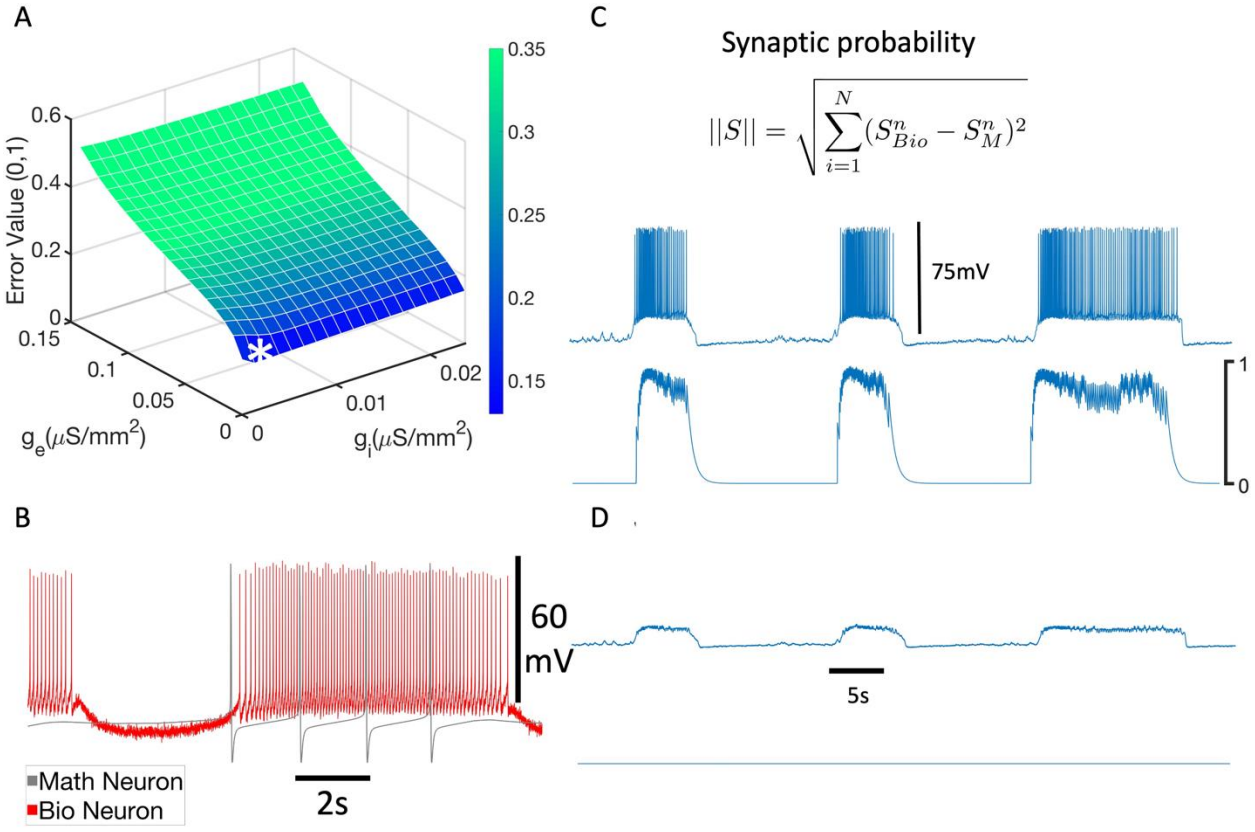

Figure 4.5 Error space of synaptic probability distance and the limitations of its respective transformation. A) The error with the excitatory and inhibitory conductance parameter space. The minimum error time series' (MET) value in the excitatory and inhibitory

conductance parameter space is shown by the white asterisk (g_i = 0.0013, g_e = 0). B) The mathematical neuron's MET (in grey) is juxtaposed over the corresponding biological recording (in red) though the action potential firing frequency was much lower than the biological recording. C) The time series where the synaptic probability works as a transformation. D) However, when the action potentials are removed from the voltage times series the limitation of the synaptic probability distance error function is revealed. The transformation does not differentiate between various "inactive" phases much like the action potential frequency.

The next function is the synaptic probability. Again, the minimum error shown by the white asterisk in the excitatory and inhibitory conductance parameter space (Figure 4.5). The mathematical neuron's voltage times series juxtaposed over the corresponding biological recording is also shown (Figure 4.5B) (red and note that the biological recording is the same as in all these simulations). However, unlike the action potential error function the minimum error simulation doesn't fit very well. This is likely due to the alpha being too high while the beta is too low, which makes the probability rise quickly and decay slowly. The synaptic probability error function can be seen to work because when every action potential in the voltage time series fires the synaptic probability rises and decays between those action potentials. Again, after removing the action potentials from the voltage times series (Figure 4.5D). Just like the action potential frequency function, the removal of action potentials reveals the limitation of the synaptic probability distance error function. Again, like the action potential frequency, any change in the voltage under threshold is completely missed. Resulting in a synaptic probability transformation that is flat even when there is a subthreshold burst of activity in the voltage time series. Meaning the transformation cannot differentiate between various "inactive" phases like the action potential frequency.

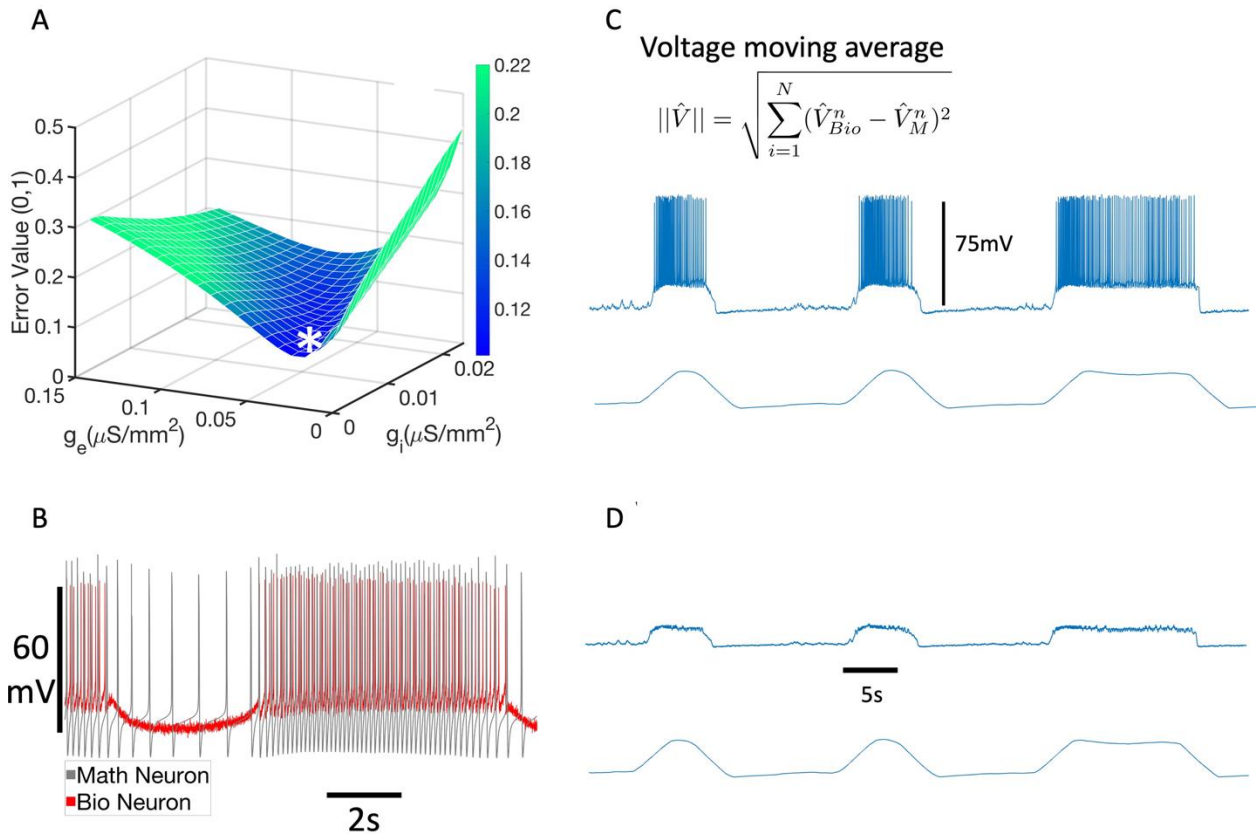

Figure 4.6 Error space of voltage moving average distance and the limitations of its respective transformation. A) The error with the excitatory and inhibitory conductance parameter space. The minimum error time series' (MET) value in the excitatory and inhibitory conductance parameter space is shown by the white asterisk (g_i = 0026, g_e = 0.0237). B) The mathematical neuron's MET (in grey) is juxtaposed over the corresponding biological recording (in red) and shows action potentials firing during the quiescent phase. C) The time series where the voltage moving average works as a transformation. D) The transformation seen in C is essentially the same as the time series in D. Meaning the transformation cannot differentiate between a subthreshold rise of action potential and that of a burst of action potential firings.

The third error function is the voltage moving average distance. The minimum error shown by the white asterisk in the excitatory and inhibitory conductance parameter space (Figure 4.6A). The mathematical neuron's voltage times series juxtaposed over the corresponding biological recording is also shown (Figure 4.6B). However, unlike the two previous error functions the minimum error simulation doesn't stop firing action potentials. The reason for this can be seen in on how the transformations view the two voltage traces (Figure 4.6C&D). How

the voltage moving average distance works is apparent when seeing the transformation trace, as the voltage raises for an extended time the moving average will raise in a lagging manner (Figure 4.6C). Furthermore, after removing the action potentials from the voltage times series as seen in Figure 4.6D. Unlike the two previous error functions, the removal of action potentials doesn't change the moving average transformations. Though change in the voltage under threshold is preserved to a degree, however, the transformations of the two voltage times series are essentially the same. Meaning the transformation cannot differentiate between a subthreshold rise of action potential and that of a burst of action potential firings. In other words, it doesn't pick up individual action potentials, which is a serious limitation.

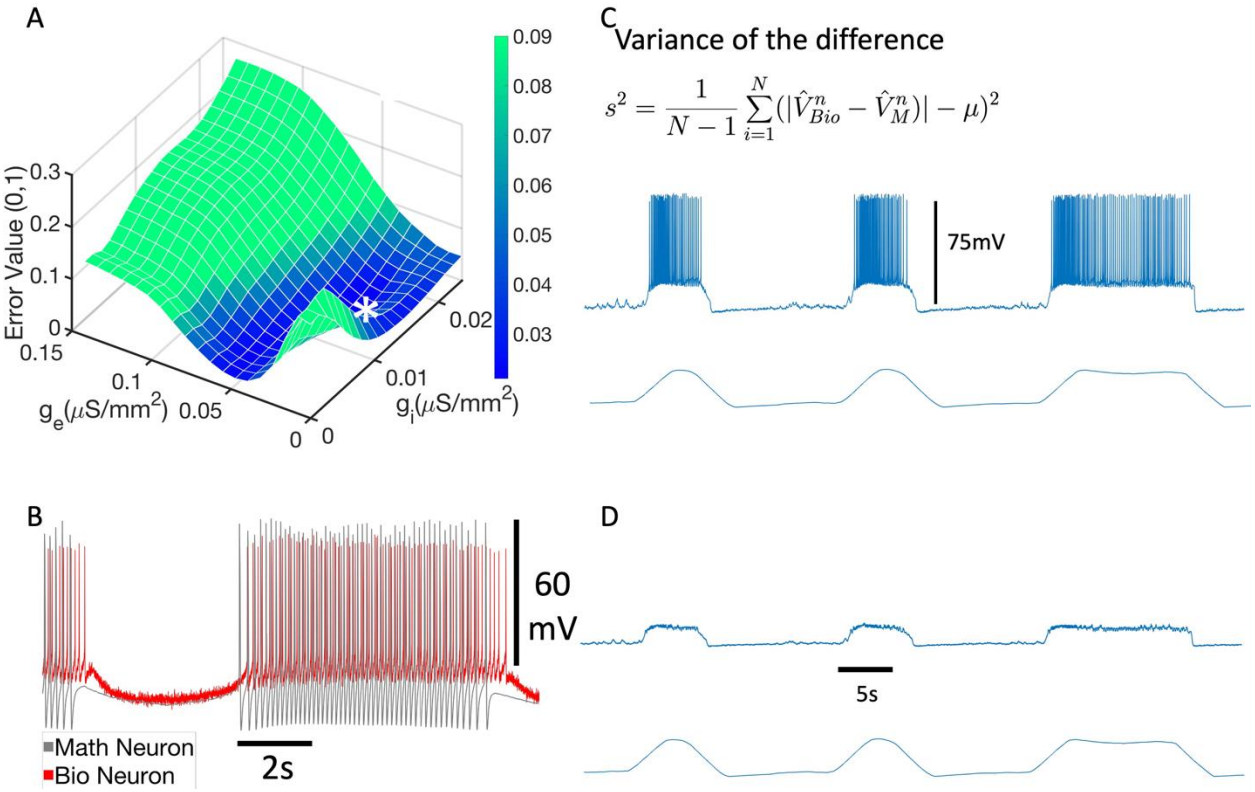

Figure 4.7 Error space of voltage moving average difference variance and the limitations of its respective transformation. A) The error with the excitatory and inhibitory conductance parameter space. The minimum error time series' (MET) value in the excitatory and inhibitory conductance parameter space is shown by the white asterisk (g_i = 0.0145, g_e = 0.0237). B) The mathematical neuron's MET (in grey) is juxtaposed over the corresponding biological recording (in red). C) The time series also uses the voltage moving average transformation therefore it

should have the same limitations. D) The transformation seen in C is essentially the same as the time series in D. Meaning the transformation cannot differentiate between a subthreshold rise of action potential and that of a burst of action potential firings.

The fourth function also uses the voltage moving average transformation, however instead of taking the distance it takes the variance of the difference. This measures the phase difference between two voltage time series without regard to absolute voltage value. So, if they are perfectly juxtoposable regardless of voltage then the error will be zero. As before, the minimum error shown by the white asterisk in the same parameter space (Figure 4.7A). On the other hand, the mathematical neuron's voltage times series juxtaposed over the corresponding biological recording (Figure 4.6B). However, unlike the previous error function that measures the voltage moving average distance the minimum error simulation stops firing action potentials. Nevertheless, this error function shares the same blind spot that is present in the voltage moving average distance. In other words, it doesn't pick up individual action potentials as is evident from the similarity of the two transformation time series.

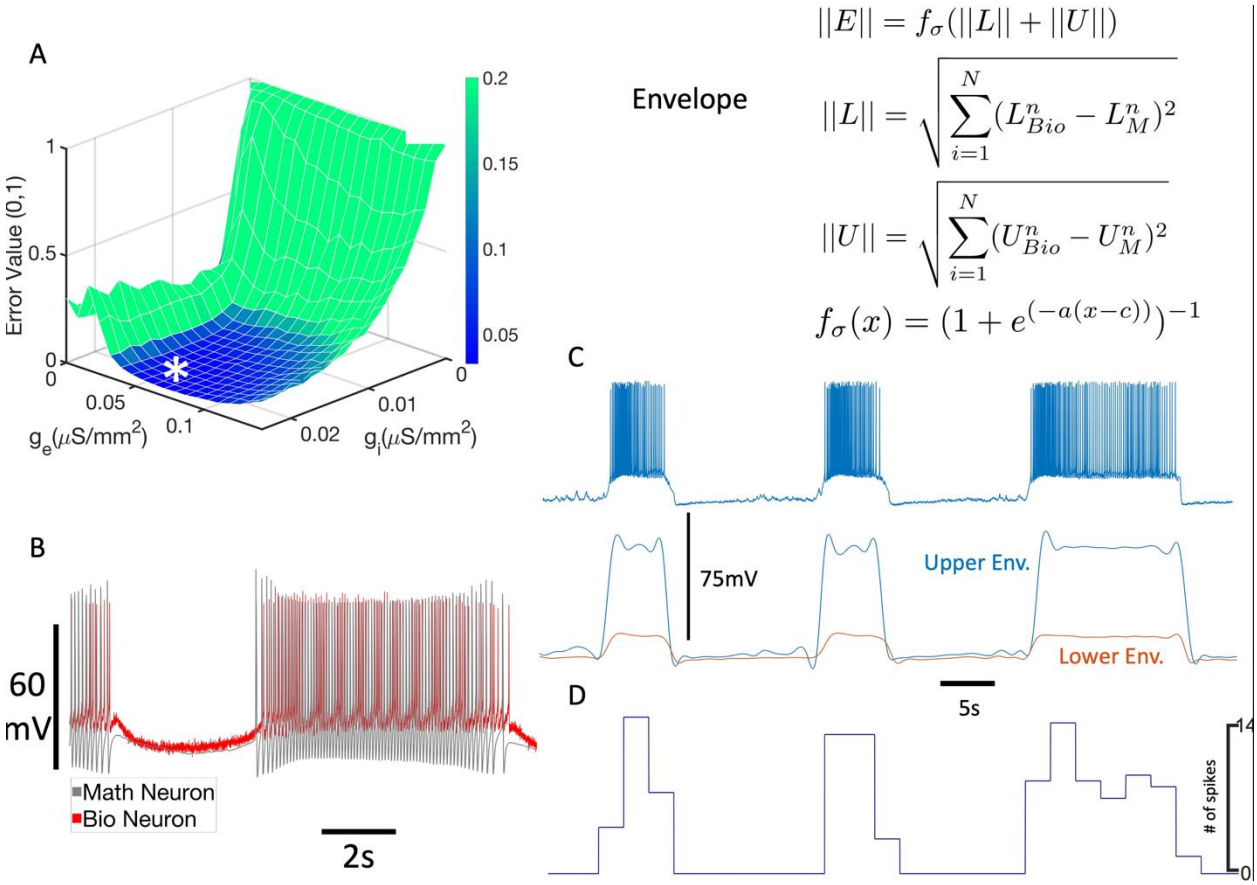

Figure 4.8 Error space of envelope distance and the limitations of its respective transformation. A) The error with the excitatory and inhibitory conductance parameter space. The minimum error time series' (MET) value in the excitatory and inhibitory conductance parameter space is shown by the white asterisk (g_i= 0.0197, g_e= 0.0553). B) The mathematical neuron's MET (in grey) is juxtaposed over the corresponding biological recording (in red). C) The time series shows the envelope transformation though the limitation is not immediately apparent. D) The limitation can be found while looking at the action potential frequency transformation of the third burst. The beginning of the burst has a higher frequency which then reaches a lower frequency; therefore, it is unable to perceive action potential frequency adaptations or action potential frequencies in general.

The final single error function is the envelope distance. Again, the white asterisk represents the minimum error in the parameter space Figure 4.8. And the juxtaposed mathematical and biological time series under of the minimum error time series. Here it can be seen what the transformations look like with the blue being the maximum outline and the red being the minimum outlines. Unlike all previous error functions, the limitation of the envelope

distance error function is not apparent when contrasted with voltage time series that have their action potentials removed, since the upper envelope would have less distance between it and the lower envelope during the active phases (Figure 4.6C). Furthermore, the inactive phases are represented well and are not missed. The limitation of this error function is not obvious. However, the limitation becomes apparent when compared with the action potential frequency transformation, specifically during the third burst of action potentials. The beginning of the burst has a higher frequency which then reaches a lower frequency (Figure 4.6D). Therefore, this error function though it captures the timing for the commencement and termination of the burst, it is unable to perceive action potential frequency adaptation. Which is an essential rhythmic characteristic of oscillations in the Melibe CPG and oscillators in general. So, this last single error function also has a critical limitation.

4.3 Combined Error Functions (CEF)

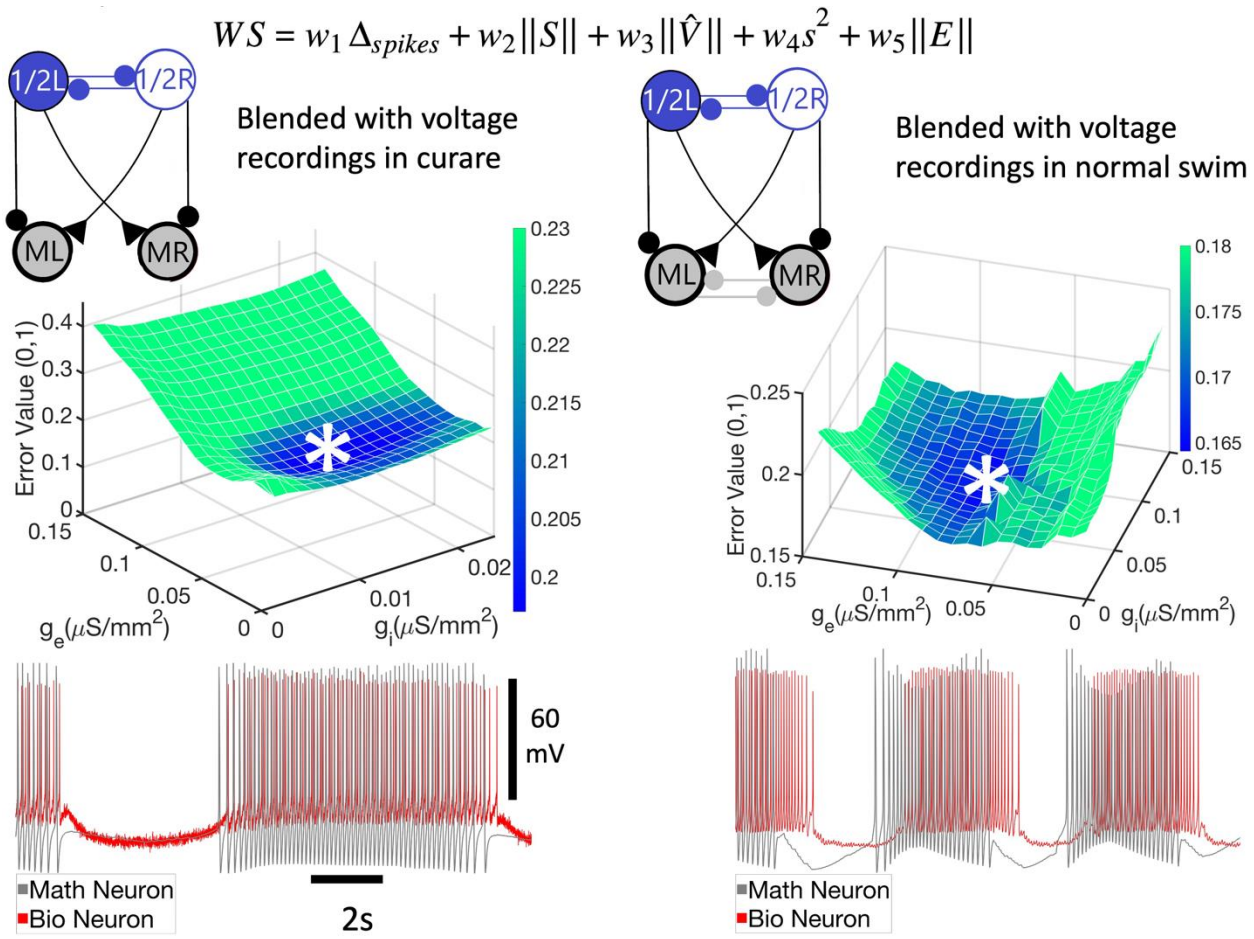

Figure 4.9 The combined error function can adjust to the cellular properties of the mathematical neuron. (a) Error space of excitatory and inhibitory synaptic conductance. z-axis is the rescaled value error of the error function, the x-axis is the conductance of the inhibitory synapses, and the y-axis is the conductance of the excitatory synapse. All best-fit time series (whether tonic spiking, borderline or quiescent) find qualitatively similar voltage time series. The minimum error shifts lower along the inhibitory conductance as the mathematical neuron shifts from a tonic spiking at $g_i = 0.01579$, $g_e = 0.0316$; borderline at $g_i = 0.0118$, $g_e = 0.0316$; to quiescent at $g_i = 0.0066$, $g_e = 0.0395$ neuron. Much like the curare the minimum error shifts lower along the inhibitory conductance as the mathematical neuron shifts from a tonic spiking at $g_i = 0.0711$, $g_e = 0.0711$; borderline at $g_i = 0.0789$, $g_e = 0.0789$; to quiescent at $g_i = 0.0237$, $g_e = 0.0474$ neuron. Furthermore, as should be expected, the minimum error shifts higher along the excitatory conductance.

To compensate for each of the single error functions a combined error function (CEF) was made. To combine the functions a simple weighted sum with each singular error function

having a coefficient and added to the others was made. Again, the location of the minimum error in the parameter space and below it the minimum error time series juxtaposed over the biological recording Figure 4.9.

Though an objective regularization is not possible in this case through the error function. To reduce over-fitting and test the flexibility and validity of the combined error function (CEF) we explored the error space of three different endogenous states of the mathematical neuron and their METs; that is we found the MET for a tonic spiking, borderline, and quiescent neuron according to the CEF. We found that the CEF can find a different g_i and g_e coordinate with a minimum error for each of the three endogenous states (Figure 4.9). We blended the same biological recordings first with tonic spiking mathematical neurons, then borderline neurons, followed by quiescent neurons. The MET for the *blended* system to tonic spiking mathematical neurons was at g_i= 0.01579, g_e= 0.0316, while the blending with borderline neurons had a MET at g_i= 0.0118, g_e= 0.0316. Finally, the quiescent neurons when blended with the biological recordings at g_i= 0.0066, g_e= 0.0395 neurons. Each of these different g_i and g_e coordinates had similar METs, so much so that there was no discernible difference (Figure 4.9, other METs not shown). On the other hand, there was a difference in the error space between each blending with the different mathematical neurons found. Specifically, the minimum error shifts lower along the inhibitory conductance as the mathematical neuron shifts to less intrinsically active (i.e., from a tonic spiking to borderline to quiescent neuron). This is expected since the more quiescent a neuron is intrinsic, the less need for an inhibition to suppress spiking during the goal inactive phases.

Now as a form of validation for the CEF, it was applied to another recording but this time without curare. And as can be seen the parameter space is not as smooth and the minimum error

time series is around a quarter out of phase with the recording (Figure 4.9). The *blended* system with normal swimming biological recordings were recordings where the CPG was not bathed in curare. In the absence of curare, the configuration of the biological CPG would be that of (Figure 4.9 right); the main difference from (Figure 4.9 left) being the mutual inhibitory synapse between the Si3 cells are present. In the case of the *blended* system, this means that the mathematical neurons would have two mathematical synapses added to recreate the mutual inhibition. This was done by adding mathematical synapses with the conductance kept conductance to not add another parameter dimension to sweep along. However, this minimum was found by sweeping only two parameters and neither change the dynamics of the synapses.

When the normal biological recording was used in the *blended* system the CEF was able to find the best-fit minimum time series for the normal swimming recording (Figure 4.9 right). Much like the *blended* system with the curare voltage time series and configuration the best fit minimum time series lower along the inhibitory conductance and higher along the excitatory conductance as the mathematical neurons change from being endogenous tonic spiking to borderline to quiescent. However, the inhibitory and excitatory conductance for the normal *blended* system is not the same as the conductance for the curare *blended* system and is discussed in the next section as seen when comparing the conductance values in (Figure 4.9).

4.4 Validating CEF

As a further form of validation, the CEF was compared to other forms of fitting. The first fitting method chosen was a fitting that was done on the pyloric central pattern generator in the stomatogastric ganglia of lobsters [77]. Also created was a simplified model of the pyloric CPG made of three neurons with an amalgamated pacemaker neuron that is an endogenous burster consisting of the anterior burster (AB) neuron electrically coupled to two pyloric dilator (PD)

neurons, and two types of follower neurons: a single lateral pyloric (LP) neuron and an amalgamated pyloric (PY) neuron made up of five to eight neurons. Using this model, they created a computational model network of the CPG and searched for combinations of synaptic strengths and intrinsic properties that produced patterns within the range of the observed rhythmic characteristics in the biological recordings. Some of these rhythmic characteristics were burst periods, the delay between the burst onsets, the gap between the termination and the burst onsets, and the duration of the burst active phase. So, they recorded from 99 lobsters, calculated the mean and standard deviation, and defined a good fit as those within two standard deviations of the mean.

4.4.1 High variance in curare voltage recordings

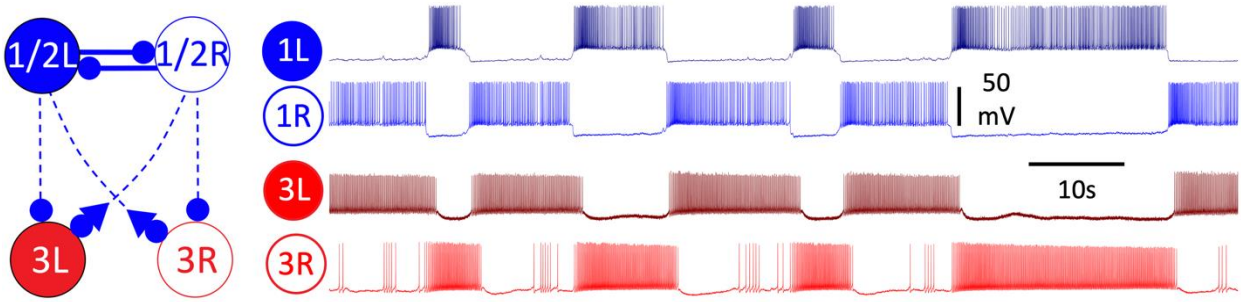

Figure 4.10 High variation of rhythmic characteristics seen in Melibe CPG recordings while in curare bath.

However, as can be seen in a recording of Melibe's swim CPG in curare Figure 4.10 there is too much variance and makes using two standard deviations of the mean as a good-fit-definition inclusive of most rhythmic characteristic measurements difficult. Another thing of note that might be asked is why not start with this method as my error function. The limitation of this method is looking at means and variance requires prior familiarity with the biological recordings' rhythmic characteristics, while the CEF can differentiate without prior knowledge of the rhythmic characteristics (in this case this means the bursts). However, calculating mean and

variance is an excellent way to define a good fit though and can be used to validate my error function. However, using means and standard deviations of the Melibe swim CPG rhythmic characteristics in curare are possible, but a different method must be used than that was to analyze the rhythmic characteristics of the pyloric CPG.

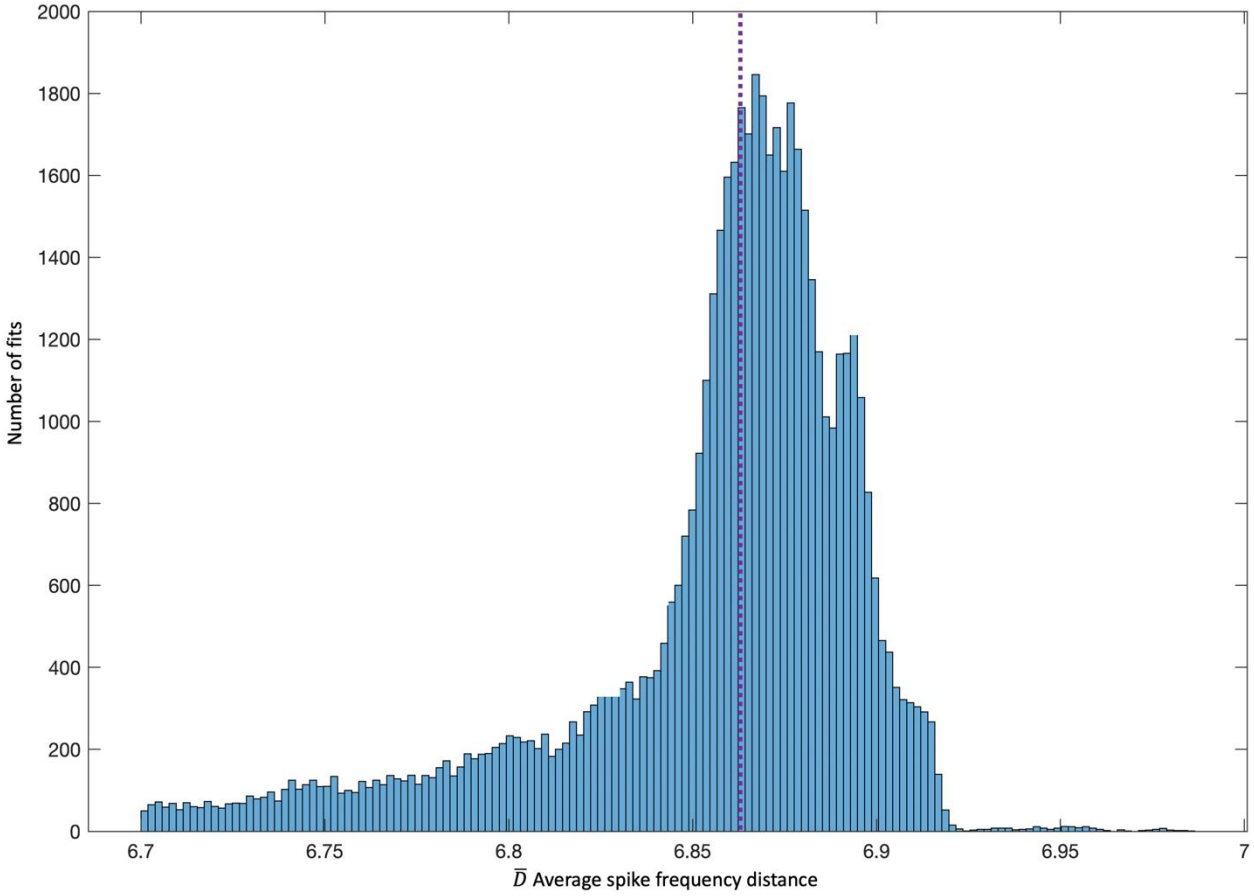

Figure 4.11 Bi-parametric sweep of the inhibitory and excitatory conductance at a 250 by 250 resolution measuring the average spike frequency distance per burst period of the mathematical neuron. This results in 62500 mathematical time series and each average spike frequency distance was measured against the same biological recording. A) The histogram of the distance per burst for the mathematical times series with outliers removed (μ = 6.8564). This sweep doesn't differentiate between good or bad fits therefore it is a distribution of the average spike frequency distance per burst period in inhibitory and excitatory conductance space. B) Bar graph showing the mean and the standard error of the mean. Also shows the CEF defined best fit (red dot). The CEF's average spike frequency distance per burst value equals 1.9 and the z-score of the error function's best fit of -119.

To overcome the high variance seen in Melibe swim CPGs and some of the limitations of rhythmic characteristics mean and variance calculations the spike frequency was used. To illustrate, as seen in Figure 4.12 the biological voltage recording of the right Si3 neuron in red with the mathematical neuron that is meant to simulate the recording in black below it. Under these two traces (Figure 4.12 bottom) is their spike frequency transformation in their respective colors. The Euclidean distance of the spike frequency difference between the two is taken. First, the difference between the mathematical frequency and the biological for an ordinal bin was taken. For example, in the fourth ordinal bin seen in the bottom of Figure 4.12 takes the difference of the spike count, then squares it, then sum all the bins and take the square root of the sum. So far this is just the action potential frequency transformation.

$$||\mathrm{D}|| = \sqrt{\sum_{\mathrm{i}=1}^{\mathrm{N}} \left(\mathrm{f}_{(n)}^{math} - \mathrm{f}_{(n)}^{bio}\right)^2}, \qquad [11]$$

But to calculate an average that is generalizable to any time series the total distance of the entire trace by the number of periods must be divided, giving the average spike frequency distance per burst,

$$\overline{D} = \frac{\left|\left|D\right|\right|}{P}. \qquad [12]$$

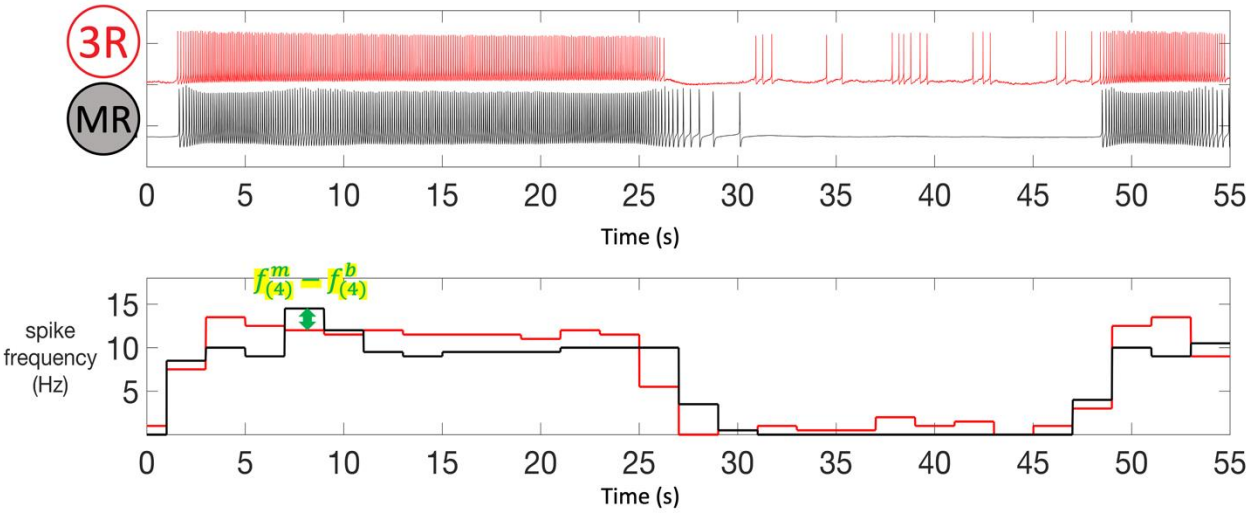

Figure 4.12 Measuring the performance of the mathematical neuron using spike frequency.

To address the high variance of the recordings in curare the average spike frequency distance from the mathematical neuron were taken and tested against the whole parameter space's performance. This was done by doing another bi-parametric sweep of the inhibitory and excitatory conductance at a 250 by 250 resolution. This results in 62500 mathematical time series and the average spike frequency distance to the biological recording for each mathematical times series was measured. A histogram of the distance per burst for the mathematical times series with outliers removed is shown in Figure 4.12, with the mean being 6.8564. This sweep gives the average of all times series including the bad fits. So, it gives a distribution of the mean distance per burst of a parameter couple. This means that the less the error value is compared to the mean the better the mathematical times series, so we want a good fit to much less than the mean.

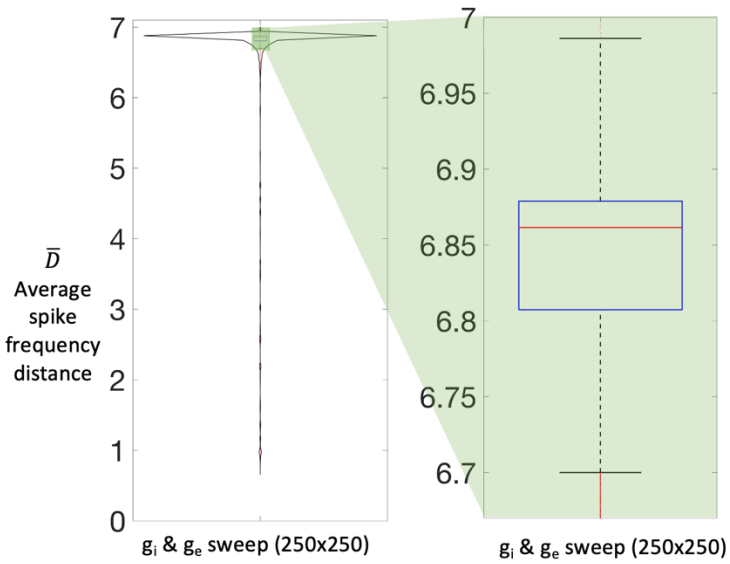

Figure 4.13 Violin plot showing the distribution of the $\bar{D}$ across the 250 by 250 g_i&g_e sweep (left). A box plot showing the distribution of with outliers removed (right).

The violin and box plot showing the mean (Figure 4.13). With its average spike frequency distance value being 1.9 and the more pronounced Z-score of the CEF best fit of -119. This is a significant z-score which shows how much better the CEF best fit is compared to the rest of the parameter space. This takes care of the variance between the bursts because it tests against the performance of the mathematical neuron rather than the bursts of the biological recording. This is an important step in the analysis because it's only been shown that the CEF passes the eye test but with this Z- score, the first objective validation for the CEF.

But all of these are still compared to only a few voltage recordings. Therefore, to produce a solution for computational neuroscientists in the future that do not have the access to a treasure trove of recordings. Voltage was intentionally left out from the term recordings because the technique posited in the next section could work for any time series, like calcium imaging recordings.

4.5 Data Augmentation

To solve the lack of data inspiration was taken from a data analysis technique called data augmentation. There are two ways in data analysis to augment data, one is creating synthetic data which is not being used so details of which will be forgone, and the other is by adding slightly modified copies of the data. For data analysis, data augmentation is used to reduce overfitting by acting as a regularizer, which means that it makes its answer simpler and therefore more generalizable. There are several ways used to augment data when training machine learning models. For example, to create more images from an image, they can horizontally be flipped and still be recognized as the image, yet it is still a different picture. The image can be cropped and still be recognizable, or rotate, blur, brighten, or darken. Therefore, from a single image, there are now seven. However, which one of these can be used to usefully augment the data depends on the data. Let's take the voltage time series as an example, horizontal flipping wouldn't be appropriate since that would mean looking at the recording in backward time. Rotating, brightening, and darkening are not characteristics that have parallels in the voltage times series. Rescaling could be done by decreasing the sampling rate however any downscaling could possibly miss action potentials. That leaves cropping and though vertical cropping doesn't make sense in voltage time series, but horizontal cropping does.

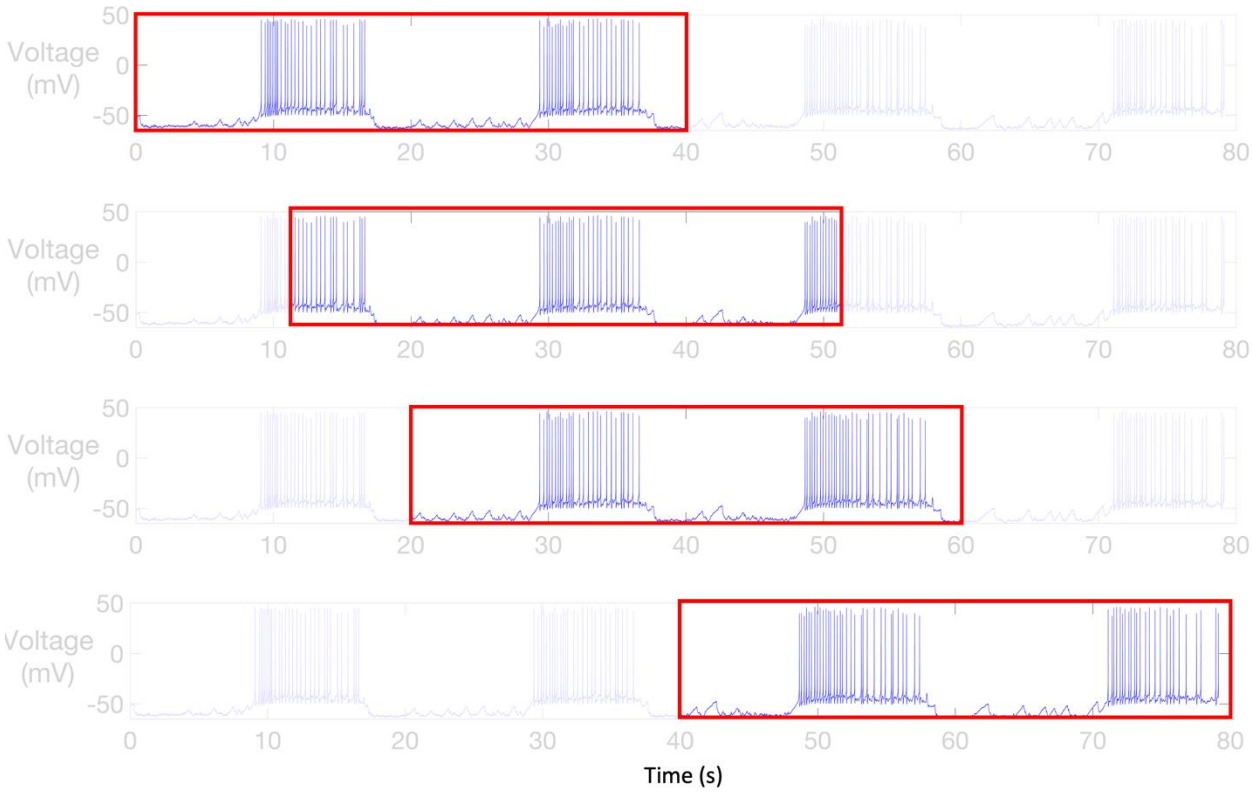

Figure 4.14 Examples of cropped shorter windows from a larger time series. Each one taken as a separate time series for a blended system. Shown here is an 80-second-long time series with 40 second windows that slide by ten seconds for every window. The first window would be from the zero to forty seconds, sliding to another from ten to fifty, another from twenty to sixty, and so on until you have the last 40 second window from forty to eighty seconds.

The time series is cropped at different parts to create several shorter time series (Figure 4.14). For example, a 40-second window is taken from an 80-second-long time series and slides by ten seconds for every window. The first window would be from zero to forty seconds, sliding to another from ten to fifty, another from twenty to sixty, and so on until the last 40-second window from forty to eighty seconds. This was done in practice with longer widows but shorter sliding jumps from one window to the next. In other words, 78-second intervals were taken that slide 0.01 seconds. This would result in a single time series augmented to 200 windows. Once these 200 windows were produced, they would be used for the *blended* system and measure the average distance per burst and their error value according to the CEF.

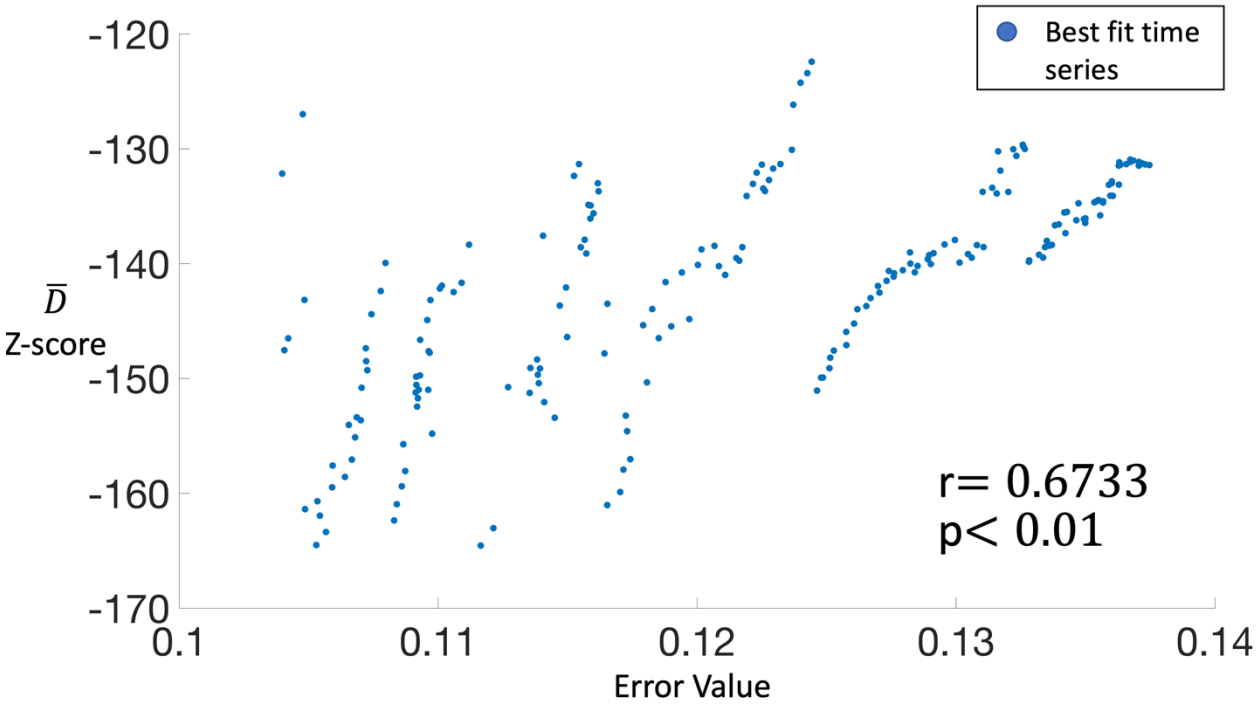

Figure 4.15 Scatter plot of the CEF value against the corresponding z-scores of each of the cropped windows. A significant moderate correlation of r = 0.6733 p < 0.01. Indicating the best fit according to my CEF is measuring similar rhythmic characteristics to that of the average distance per burst measurement. Furthermore, comparing the best fits to many voltage recordings that were produced by data augmentation is another piece of evidence that they are measuring similar characteristics.

With the 200 best-fit error values according to the CEF and their distance per burst Z-score were plotted against each other (Figure 4.15). A significant moderate correlation of r equals 0.6733 was measured. This indicates that the best fit according to the CEF is measuring similar rhythmic characteristics to that of the average distance per burst measurement. Furthermore, comparing the best fits to many voltage recordings that were produced by data augmentation is another piece of evidence that they are measuring similar characteristics. This shows this data augmentation method can give computational neuroscientists access to more recordings. Though as a caveat, data augmentation can't completely compensate for a lack of

data and is only meant to complement. When augmenting very little data it is likely to create a biased system.

4.6 Octa-parameter sweeps.

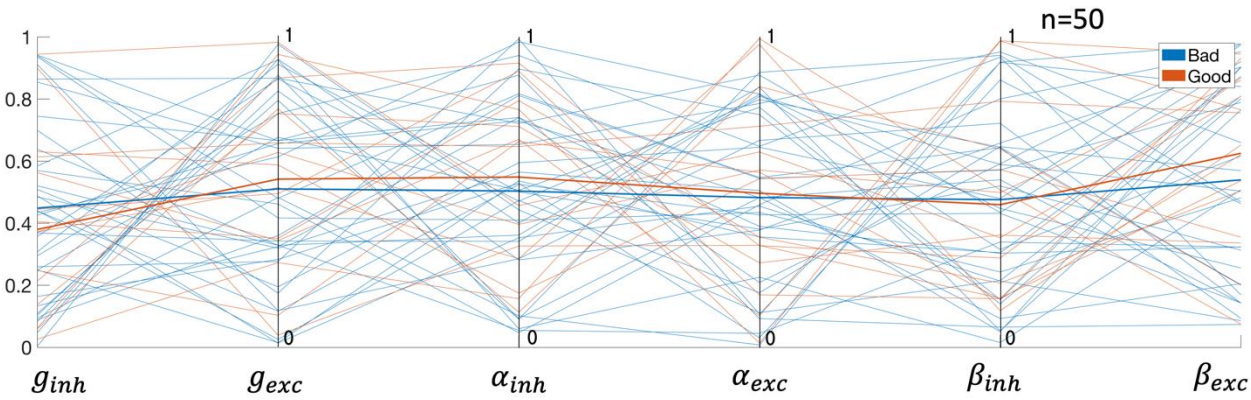

Figure 4.16 Parallel coordinate graph showing 6 of the 8 parameter values of 50 mathematical voltage time series. To show a single time series comparison in 8 parameter dimensions, there are 8 equally spaced vertical parallel axes. Each time series comparison in the octa-parameter space is represented as a polyline with vertices on the parallel axes. Each connected series of line segments represents the parameters of each time series. The parameters of each time series were chosen using uniformly distributed random sampling. Random sampling was used to avoid the convergence to single points on each vertex that obscures any differentiation between individual times series parameter sets. The eight parameters are the synaptic conductance of the inhibitory (g_{inh}) and excitatory synapses (g_{exc}), and the added alpha (α_{inh}, α_{exc}), beta (β_{inh}, β_{exc}), and synaptic threshold (V_{th-i}, V_{th-e}) of both the inhibitory and excitatory synapses.

With this the CEF was satisfactorily validated, and the next step was taken, increasing the number of parameters. Since one goal of the study is to study emergent rhythms, the number of parameters were set to eight synaptic parameters hence the name Octo-parameter. These eight parameters were chosen because previous studies already characterized the intracellular properties of Melibe. As before the synaptic conductance of the inhibitory and excitatory synapses was used, and now the alpha, beta, and synaptic threshold of both the inhibitory and excitatory synapses were added (Figure 4.16&Figure 4.17). G represents the maximal conductance of the synaptic current, whereas alpha, beta, and voltage threshold are part of the

synaptic probability equation. As previously mentioned, biologically, alpha corresponds to the strength of the binding of the neurotransmitters to the post-synaptic receptors. In contrast, beta corresponds to the decay from the combination of diffusion, enzymatic metabolizing or inactivation, and re-uptake into the presynaptic neuron of the neurotransmitters in the synaptic cleft. The voltage threshold is typically set around +20mV in the middle of spikes, between the spike threshold around −40mV (sodium channels open) and the spike peak of +40mV. To visualize the parameter space in 8-dimensions a parallel coordinate plot was used and is a common way to visualize high-dimensional data (Figure 4.16&Figure 4.17).

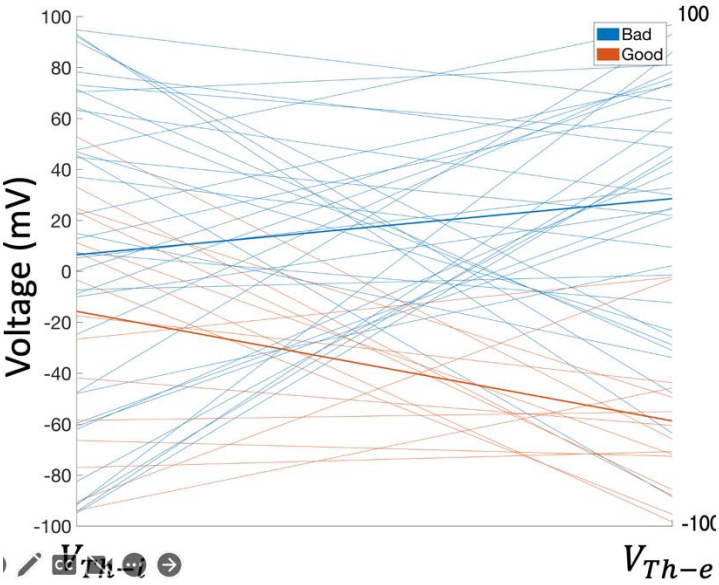

Figure 4.17 Parallel coordinate graph showing the final 2 parameter values of 50 mathematical voltage time series. To show a single time series comparison in 8 parameter dimensions, there are 8 equally spaced vertical parallel axes. Each time series comparison in the octa-parameter space is represented as a polyline with vertices on the parallel axes. Each connected series of line segments represents the parameters of each time series. The parameters of each time series were chosen using uniformly distributed random sampling. Random sampling was used to avoid the convergence to single points on each vertex that obscures any differentiation between individual times series parameter sets. The eight parameters are the synaptic conductance of the inhibitory (g_{inh}) and excitatory synapses (g_{exc}), and the added alpha (α_{inh}, α_{exc}), beta (β_{inh}, β_{exc}), and synaptic threshold (V_{th-i}, V_{th-e}) of both the inhibitory and excitatory synapses.

For this study in order to show a single time series comparison in 8 parameter dimensions, there are 8 equally spaced vertical parallel axes. Each time series comparison in the octa-parameter space is represented as a polyline with vertices on the parallel axes. In other words, each connected series of line segments represents the parameters of each time series. The parameters of each time series were chosen using uniformly distributed random sampling which means that there is an equal chance for any of the values to be observed, as opposed to a normal distribution. The reason for using random sampling and not a parameter sweep as was previously done is because using a parameter sweep on parallel coordinates would make the lines converge to single points on each vertex and obscure any differentiation between individual times series parameter sets. To clarify a parameter sweep is simply searching through the parameter space using a predetermined subset of values and trying all possible combinations. Random search, on the other hand, is generally faster and used if a larger or high dimensional space was searched, because it samples more diverse array combinations, as well as being faster and more control over the number of samples generated. For example, to do an 8-dimensional sweep of parameters using only two values (the minimum to be called a sweep) for each parameter would result in a minimum of 2^8 or 256 time-series parameter combinations. While random sampling can be set it to any number of time series parameter combinations. With this the number of time series was set to 50 and used k-means clustering to categorize the parameter combinations into good fits in orange and bad fits in blue. Then the average value was taken of each parameter of the good and bad fits which are shown as the thicker lines on the parallel coordinates.

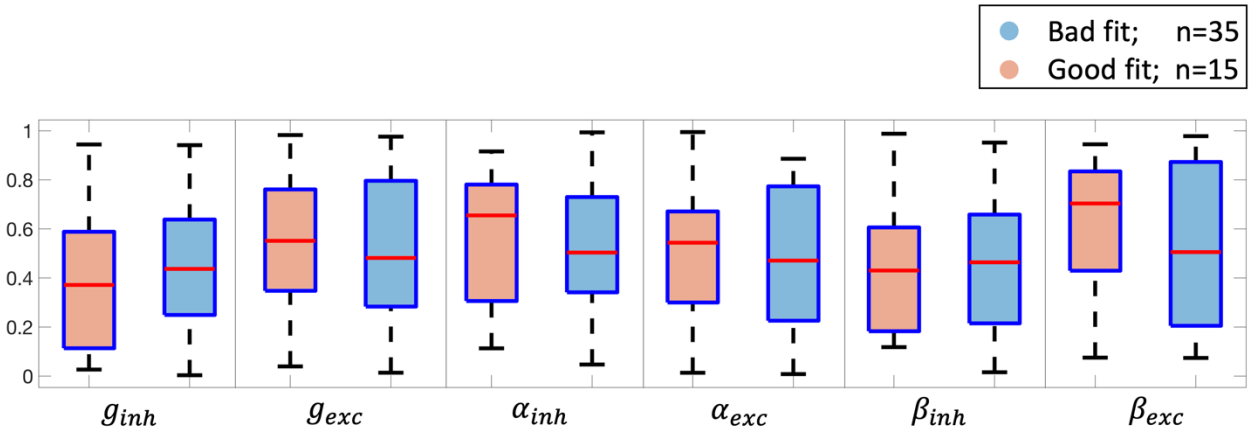

Figure 4.18 No significant differences in the first six parameters. Box plots of the good and bad fits showing their distributions. The categorized parameters in bad fit groups in blue and good in orange shown in box plots. The populations for each parameter had a Wilcoxon rank sum\ Mann-Whitney test performed on them. Relatively small sample size as to not amplify any difference to the point of significance for even the irrelevant differences.

The box plots of the parameters categorized into bad fit groups in blue and good in orange (Figure 4.18Figure 4.19). With the good and bad are grouped, to test the difference between the good and bad fit populations for each parameter, a Mann-Whitney test was performed. Again, a relatively small sample size was used for the same reason previously mentioned because the sample size can be made so large that it will amplify any difference to the point of significance even the irrelevant ones. The only significant difference was found between the excitatory synaptic threshold. Furthermore, the good fit range of the excitatory synaptic threshold is outside the typical range, In fact, most of the good fits are under the action potential threshold of -40mV. This is an interesting find because it indicates that there is a contralateral electric synapse between the Si3 neuron and its contralateral Si1 or Si2 which was not previously hypothesized by biological experiments.

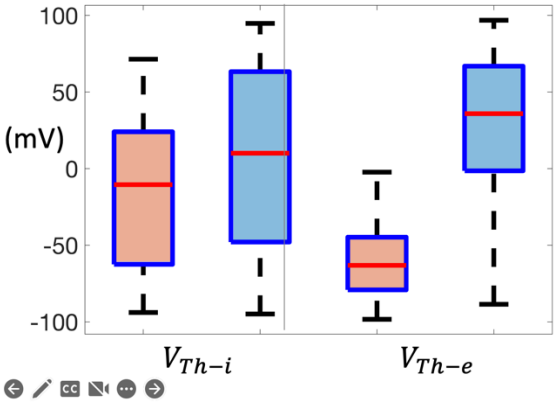

Figure 4.19 A significant difference in the synaptic threshold in the excitatory synapses. The good fit range of the excitatory synaptic threshold is outside the typical range. In fact, most of the good fits are under the action potential threshold of -40mV. Box plots of the good and bad fits showing their distributions. The categorized parameters in bad fit groups in blue and good in orange shown in box plots. The populations for each parameter had a Wilcoxon rank sum\ Mann-Whitney test performed on them. Relatively small sample size as to not amplify any difference to the point of significance for even the irrelevant differences.

Here is the hypothesized change to the configuration illustrated in the diagram (Figure 4.20). On the top left is the current reduced configuration it is changed to the diagram on the top right of the new hypothesized configuration. The biphasic response from the amalgamated Si 1,2,4 cell to Si3 is replaced with an electrical synapse and a fast inhibitory synapse. This is hypothesized from the biphasic response experiments shown in Figure 2.7 where the inhibition begins before the excitation and can now be explained with a combination of an electrical synapse and a fast inhibitory synapse. However, the electrical synapse can be added from either or both Si1s and Si2s to the contralateral Si3s of the diagram without any replacing of the biphasic synapse. In other words, the presence of an electrical synapse does not necessarily explain the biphasic response.

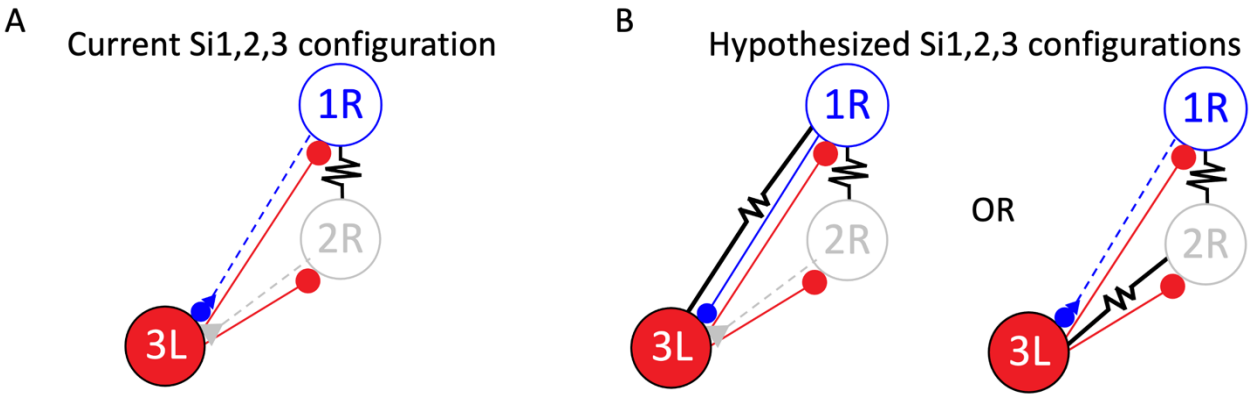

Figure 4.20 The hypothesized change to the configuration illustrated in the diagram. Here on the top left is the current reduced configuration it is changed to the diagram on the top right of the new hypothesized configuration. The biphasic response from the amalgamated Si 1,2,4 cell to Si3 is replaced with an electrical synapse and a fast inhibitory synapse. This is hypothesized from the biphasic response experiments you can see that the inhibition starts before the excitation this can be explained with a combination of an electrical synapse and a fast inhibitory synapse.

In addition to testing the difference between the good and bad groups, any correlation between the good fits and each of the parameters to show if there are any strong relationships between the parameters was done. As shown in the heatmap (Figure 4.21) there were no strong correlations between any of the parameters and some even show significance, but the correlation is near inexistant.

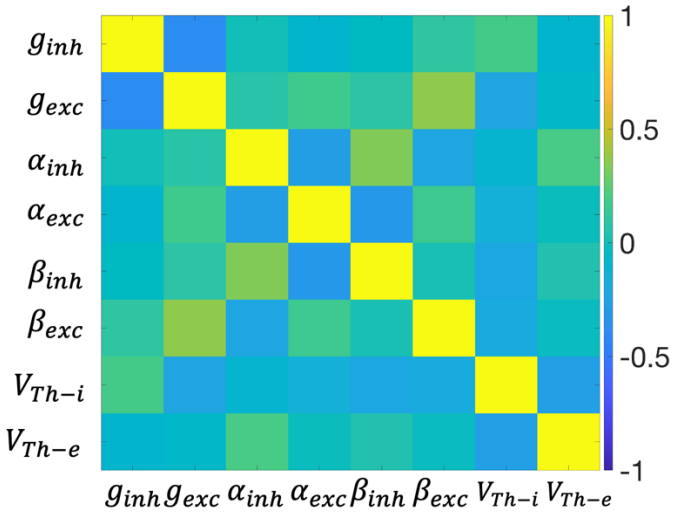

Figure 4.21 Heatmap showing any correlation in the good fits between each of the parameters. As shown in the heatmap here there were no strong correlations between any of the parameters and some even show significance, but the correlation is though still weak.

5 OTHER BLENDED SYSTEMS

To further explore the *blended* system Dendronotus iris CPG Si recordings were used to create several different configurations that test different HCO emergence models and perturbations. Figure 5.1 simplifies the same rhythmic generation seen in Dendronotus iris where a tonic spiking neuron excites mutually inhibiting neurons to burst in antiphase of each other. The biological recordings shown in black are from a Si1 cell and blended and excite to mutually inhibited mathematical neurons and as you can see, they create an antiphase bursting though neither of them fires in isolation.

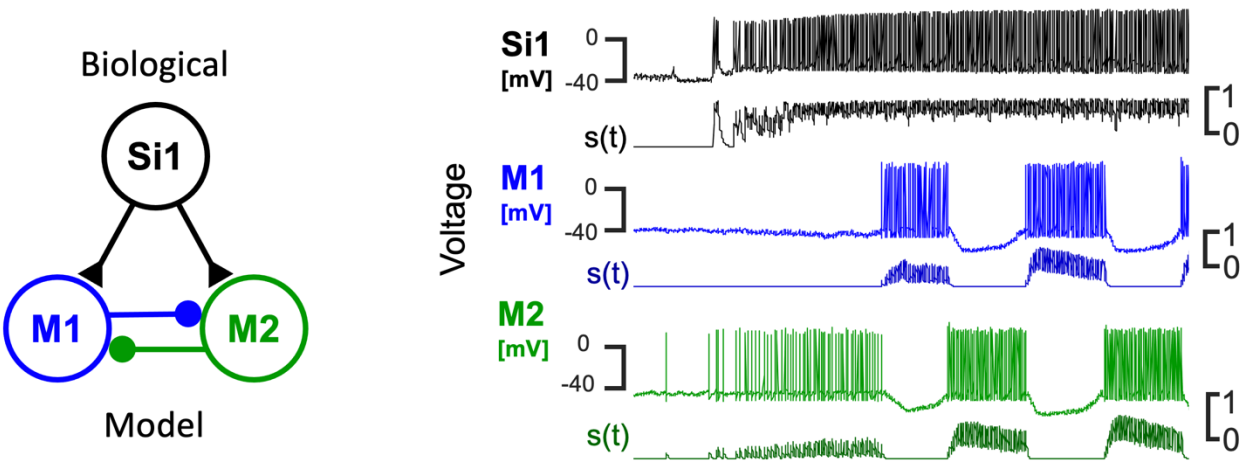

Figure 5.1 A blended system using Dendronotus Si1 voltage recording to create an HCO rhythm in mathematical neurons. A diagram of the blended configuration of the biological Si1 neuron excites two quiescent mathematical neurons (Left). A previously recorded voltage time series of Dendronotus swimming interneuron (Si1) with its respective blended synaptic release probability, shown over the two mathematical neurons' voltage time series and their respective synaptic release probability (Right). The inhibitory and excitatory synapses are denoted by • and ▲, respectively. The black synapses represent the mathematical synapses driven by the biological recordings from the Si1 neuron. With M1 (Blue) and M2 (Green) representing two mathematical neurons and Si1 representing the previously recorded swimming interneuron (Black).

In Figure 5.2 are the biological recordings of a bursting Si3 in black blended and exciting a quiescent mathematical neuron and inhibiting a tonic spiking mathematical neuron that is mutually inhibiting each other. And as you can see, they create an antiphase bursting though neither of them bursts in isolation. This is characteristic of a pacemaker configuration of bursting like those seen in the pyloric CPG. These two show the director paradigm of CPG models.

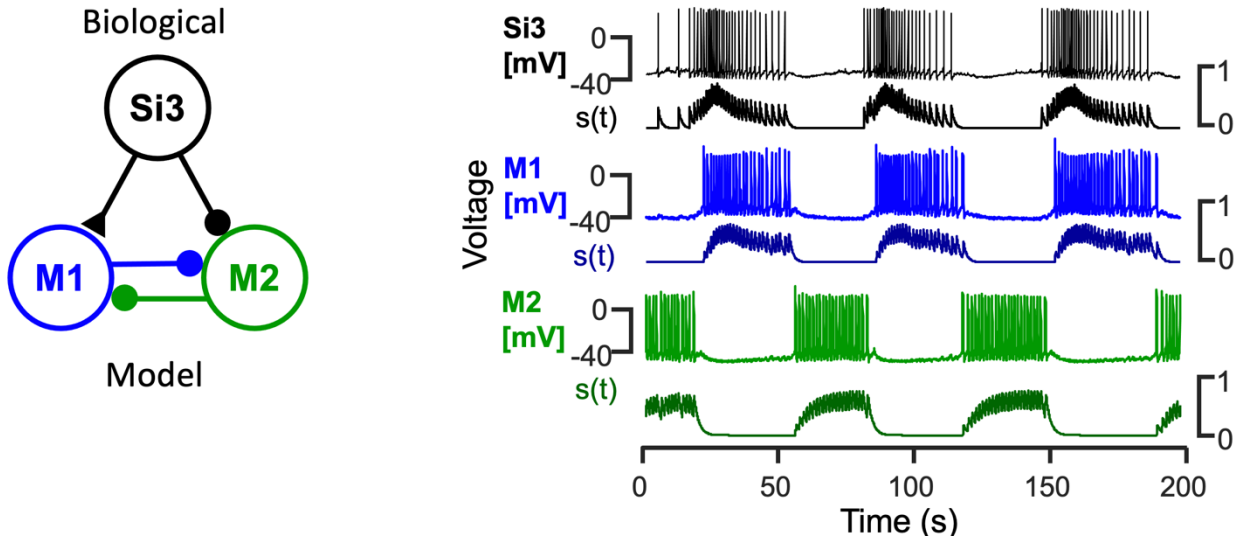

Figure 5.2 A blended system using Dendronotus Si3 voltage recording to create an HCO rhythm in mathematical neurons. A diagram of the blended configuration of the biological Si1 neuron excites one quiescent mathematical neuron and inhibits another tonic-spiking neuron (Left). A previously recorded voltage time series of Dendronotus swimming interneuron (Si3), with its respective blended synaptic release probability, shown over the two mathematical neurons' voltage time series and their respective synaptic release probability (Right). The inhibitory and excitatory synapses are denoted by • and ▲, respectively. The black synapses represent the mathematical synapses driven by the biological recordings from the Si1 neuron. With M1 (Blue) and M2 (Green) representing two mathematical neurons and Si3 representing the previously recorded swimming interneuron (Black).

Next is how a *blended* system reacts to perturbations seen in the biological recordings. In Figure 5.3 on the right is biological recordings from two Melibe Si1 cells that ipsilaterally inhibit tonic spiking mathematical neurons. One of the Si1 voltage recordings shows that the top voltage recording of the biological neuron was perturbed shortly after it begins bursting indicated by the red arrow. This causes the termination of the burst and the initiation of the Si1 neuron burst. The mathematical neurons replicate the activity of the mathematical ones, though they replicate the neuron that is not directly synapsed to them.

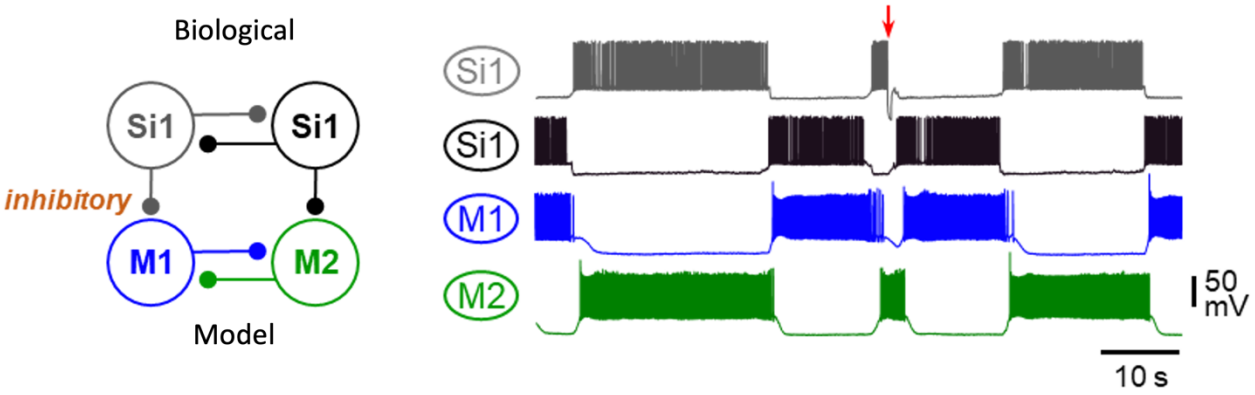

Figure 5.3 How a blended system with inhibitory synapses reacts to perturbations seen in the biological recordings. Here on the top is biological recordings from two Melibe Si1 cells that ipsilaterally inhibit tonic spiking mathematical neurons. One of the Si1 voltage recordings shows that the top voltage recording of the biological neuron was perturbed shortly after it begins bursting indicated by the red arrow. This causes the termination of the burst and the initiation of the Si1 neuron burst. The mathematical neurons replicate the activity of the mathematical ones, though they replicate the neuron that is not directly synapsed to them.

On the other hand, if the Si1s ipsilaterally excite quiescent mathematical neurons as seen in Figure 5.4 right the mathematical neurons replicate the activity the mathematical ones, though this time they replicate the neuron that is directly synapsed to them.

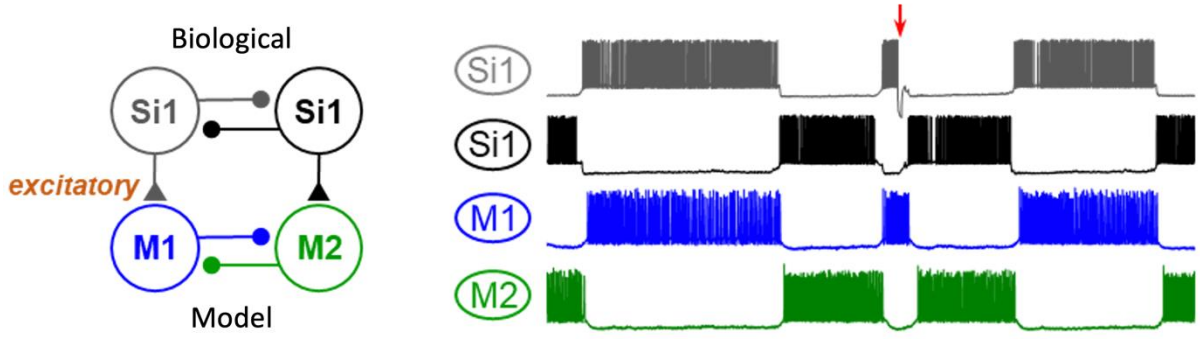

Figure 5.4 How a blended system with excitatory synapses reacts to perturbations seen in the biological recordings. The biological recordings from two Melibe Si1 cells that ipsilaterally inhibit excite quiescent mathematical neurons. One of the Si1 voltage recordings shows that the top voltage recording of the biological neuron was perturbed shortly after it begins bursting indicated by the red arrow. This causes the termination of the burst and the initiation of the Si1 neuron burst. The mathematical neurons replicate the activity the mathematical ones, though this time they replicate the neuron that is directly synapsed to them.

6 TESTING BLENDED SYSTEMS WITH CEF

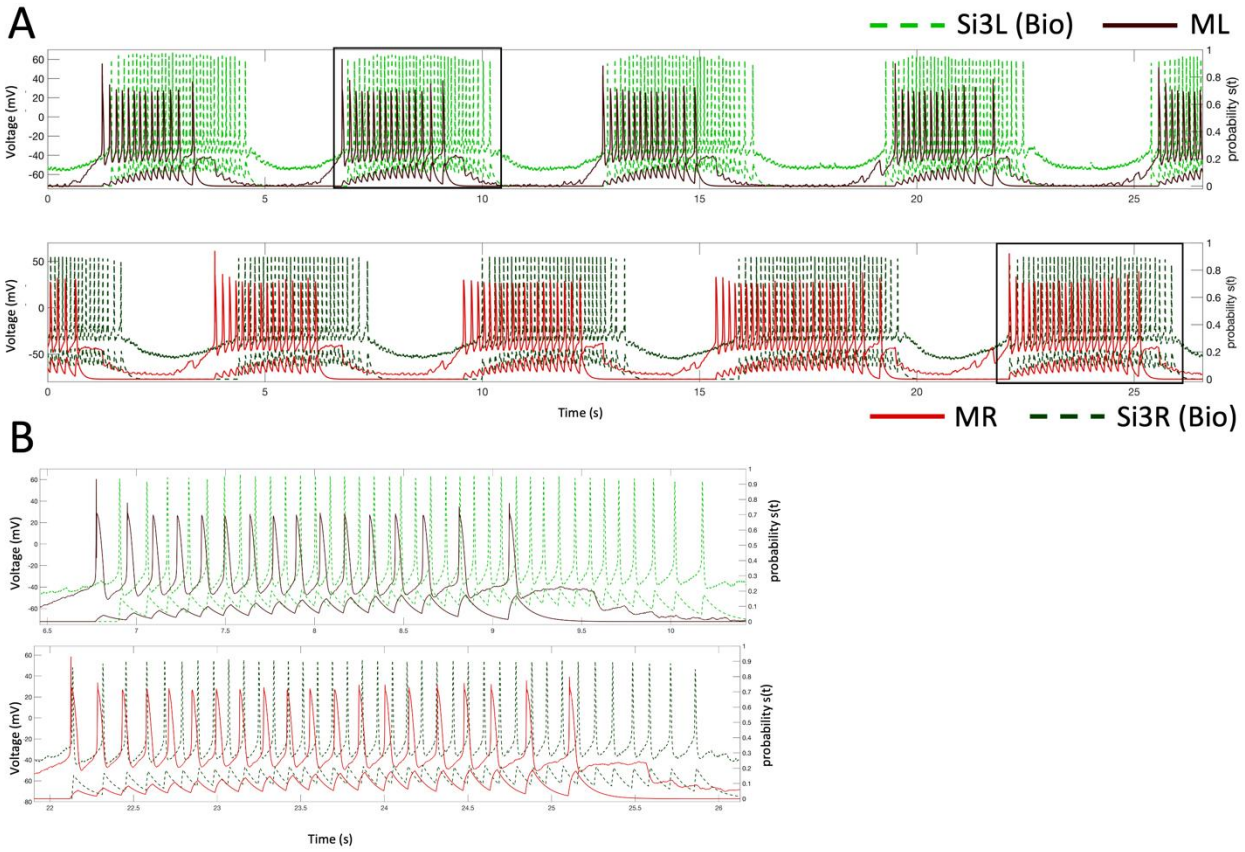

Figure 6.1 The normal swim case where math neuron voltage time series is superimposed on the biological voltage recordings of their respective Si3 neurons does not meet the threshold of a good fit. You can also see when zoomed in the action potentials in the mathematical neurons are thicker than the biological recordings. The error value according to the CEF is 0.2710. Which according to the previously mentioned cutoff of 2.2 would be considered a bad fit. So now we have an example of how a voltage time series can pass the eye test but not be considered a good fit. In the table, we can also see where the mathematical neuron has gone wrong in the weighted error value column. The synaptic distance is responsible for most of the error with the variance of the moving average difference being the least. This tells us that the phase is relatively close, but the voltage of the mathematical neuron is shifted lower relative to that of the biological recording.

First, let's take this previously shown *blended* system in the normal swim case (Figure 3.3). As mentioned before the mathematical neuron appears to pass the “eye test.” However, when we superimpose the math neuron voltage time series on the biological voltage recordings of their respective Si3 neurons the start and end of the bursts don’t look as good as was first

thought (Figure 6.1). You can also see when zoomed in the action potentials in the mathematical neurons are thicker than the biological recordings. The error value according to the CEF is 0.2710. Which according to the previously mentioned cutoff would be considered a bad fit. So now we have an example of how a voltage time series can pass the eye test but not be considered a good fit.

Table 1 Error values of hand-tuned normal blended system

Error type	Error value	Weighted error value
CEF	0.2710	
Synaptic	0.2180	0.1258
Spikes	0.4698	0.0452
Volt. MA	0.5848	0.0563
Variance diff.	0.0346	0.0067
Envelope	0.5661	0.0372

In Table 1, we can also see where the mathematical neuron has gone wrong in the weighted error value column. The synaptic distance is responsible for most of the error with the variance of the moving average difference being the least. This tells us that the action potential characteristics are responsible for most of the error while the phase is relatively close, but the voltage of the mathematical neuron is shifted lower relative to that of the biological recording.

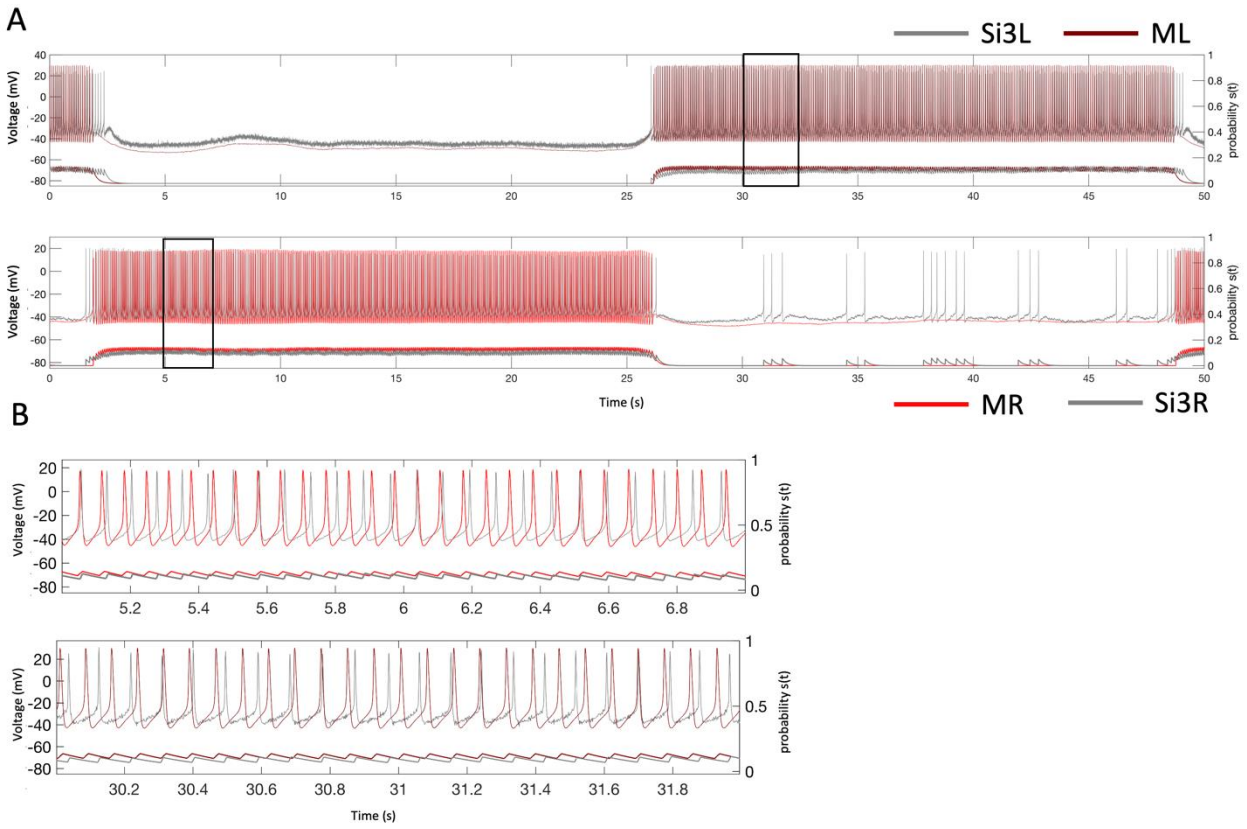

Figure 6.2 The curare case where math neuron voltage time series is superimposed on the biological voltage recordings of their respective Si3 neurons. For this case, we have an error value of 0.0730 which is low even lower than any of the other best fits found by the bi-parameter sweeps or octa-parameter sampling. This is possibly from using a limited number of parameters to tune in the sweeps and sampling specifically only using synaptic parameters, while the hand-tuned blended system had even the fast subsystem parameters tuned, which is responsible for the firing of action potentials among other things. When zoomed in the action potentials in the mathematical neurons are similar in shape to that of the biological recordings though not perfectly aligned. This gives us an example of how a hand-tuned blended system gives us a CEF good fit. In the table, we can still see where the mathematical neuron has gone wrong in the weighted error value column. Again, the synaptic distance is responsible for most of the error and in this case the envelope is the least. This tells us that the voltage of the mathematical neuron is not shifted either lower or higher relative to that of the biological recording but rather the spiking frequency is off.

Next, let's take the previously mentioned *blended* system in the curare case (Figure 3.5). Whose mathematical neurons had an apparent close similarity to the biological recordings and answering the question is it good enough? For this case, we have an error value of 0.0730 (Figure 6.2) which is low even lower than any of the other best fits found by the bi-parameter

sweeps or octa-parameter sampling. This is possibly from using a limited number of parameters to tune in the sweeps and sampling specifically only using synaptic parameters, while the hand-tuned *blended* system had even the fast subsystem parameters tuned, which as you may recall is responsible for the firing of action potentials among other things. When zoomed in the action potentials in the mathematical neurons are similar in shape to that of the biological recordings though not perfectly aligned. This gives us an example of how a hand-tuned *blended* system gives us a good fit according to the CET.

Table 2 Error values of hand-tuned curare blended system

Error type	Error value	Weighted error value
CEF	0.0730	
Synaptic	0.0861	0.0497
Spikes	0.1051	0.0101
Volt. MA	0.0981	0.0094
Variance diff.	0.0175	0.0034
Envelope	0.0115	0.0004

In Table 2, we can still see where the mathematical neuron has gone wrong in the weighted error value column. Again, the synaptic distance is responsible for most of the error and in this case the envelope is the least. This tells us that the action potential characteristics are responsible for most of the error and the voltage of the mathematical neuron is not shifted either lower or higher relative to that of the biological recording.

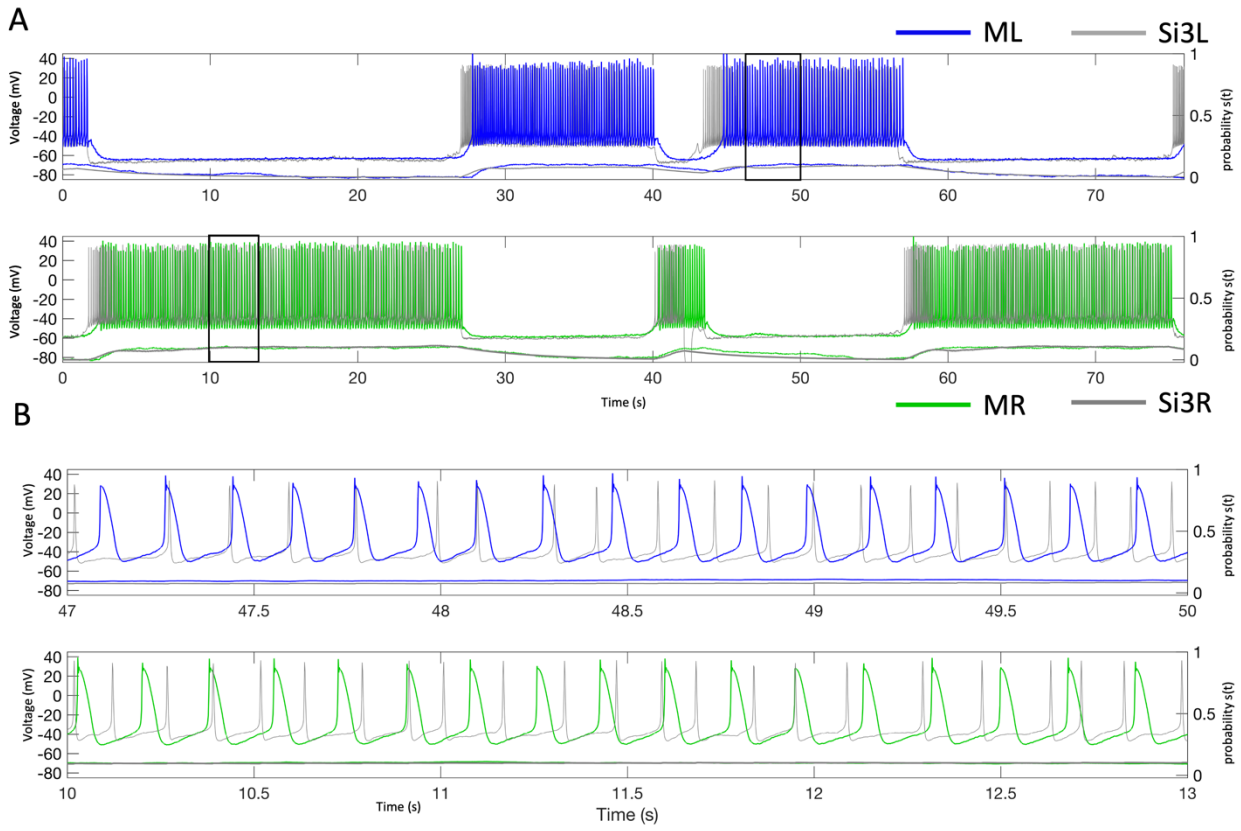

Figure 6.3 The inhibitory blended system where math neuron voltage time series is superimposed on the biological voltage recordings of their respective Si3 neurons. For this case, we have an error value of 0.0715 which is comparable to the hand-tuned curare case. When zoomed in the action potentials are thicker in shape than that of the biological recordings. This shows that the action potential shape could possibly not be represented by the CEF since the curare swim case also didn't have thicker action potentials but a similar CEF value. Again the synaptic distance is responsible for most of the error however the spike count error is close with the envelope being the least. This tells us that the spike frequency is off.

Next is the two other *blended* systems previously mentioned and their reaction to perturbations (Figure 5.3Figure 5.4). Here is with the biological Si1s inhibiting the mathematical neurons. For this case (Figure 6.3), we have an error value of 0.0715 which is comparable to the hand-tuned curare case. When zoomed in the action potentials in the mathematical neurons are thicker in shape than that of the biological recordings. This shows that the action potential shape could possibly not be represented by the CEF since the curare swim case also didn't have thicker action potentials but a similar CEF value.

Table 3 Error values of hand-tuned perturbed inhibitory synapsed blended system

Error type	Error value	Weighted error value
CEF	0.0715	
Synaptic	0.0423	0.0244
Spikes	0.2336	0.0225
Volt. MA	0.1616	0.0155
Variance diff.	0.0418	0.0080
Envelope	0.0270	0.0010

In Table 3, we can still see where the mathematical neuron has gone wrong in the weighted error value column. Again, the synaptic distance is responsible for most of the error however the spike count error is close with the envelope being the least. This tells us that the action potential characteristics are responsible for most of the error though likely from the spike frequency since there is a high error in spike count and the voltage of the mathematical neuron is not shifted either lower or higher relative to that of the biological recording.

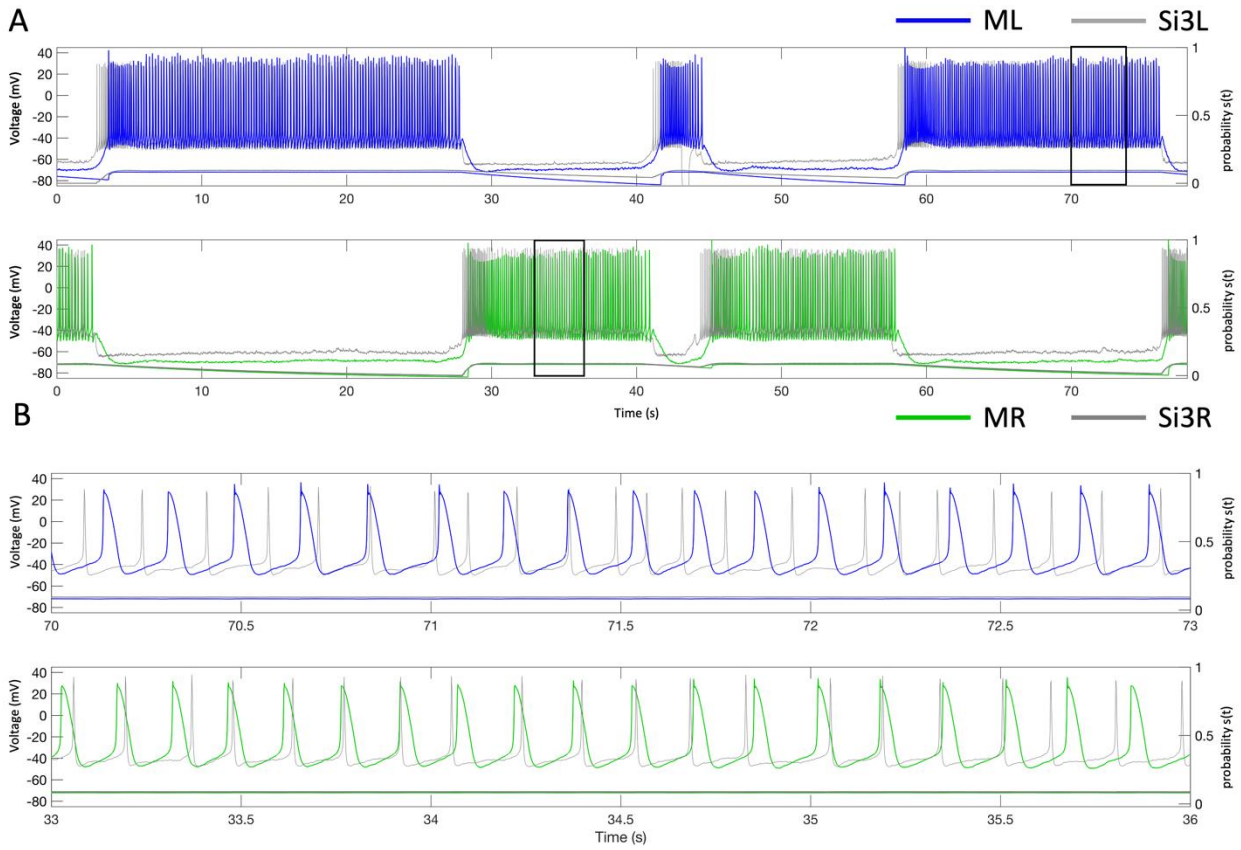

Figure 6.4 The excitatory blended system where math neuron voltage time series is superimposed on the biological voltage recordings of their respective Si3 neurons. For this case, we have an error value of 0.0727 which is comparable to the two previous cases. And like the previous case when zoomed in the action potentials in the mathematical neurons are thicker in shape than that of the biological recordings. In the table, we can see again the synaptic distance being responsible for most of the error with the envelope being the least and the higher than the previous variance difference. This tells us that the action potential characteristics are responsible for most of the error though likely from the spike frequency since there is a high error in spike count and the voltage of the mathematical neuron is not shifted either lower or higher relative to that of the biological recording though not as in phase as the previous cases as shown by the variance difference.

Next is when the biological Si1s are exciting the mathematical neurons (Figure 5.4). For this case (Figure 6.4), we have an error value of 0.0727 which is comparable to the two previous cases. And like the previous case when zoomed in the action potentials in the mathematical neurons are thicker in shape than that of the biological recordings.

Table 4 Error values of hand-tuned perturbed excitatory synapsed blended system

Error type	Error value	Weighted error value
CEF	0.0727	
Synaptic	0.0551	0.0318
Spikes	0.2172	0.0209
Volt. MA	0.0589	0.0057
Variance diff.	0.0703	0.0135
Envelope	0.0219	0.0008

In Table 4, we can see again the synaptic distance being responsible for most of the error with the envelope being the least and the higher than the previous variance difference. This tells us that the action potential characteristics are responsible for most of the error though likely from the spike frequency since there is a high error in spike count and the voltage of the mathematical neuron is not shifted either lower or higher relative to that of the biological recording though not as in phase as the previous cases as shown by the variance difference.

7 CONCLUSION

In Summary, to take one further step of simplification a blending of previously recorded voltage time series with mathematical neurons was done. This blending required the development of an ODE solver that we ourselves developed. And configured like that of the simplified Melibe's swimming CPG. The *blended* system was also shown to be able to act as rhythm directors like pacemakers and drivers of Dendronotus Si cells. As well as replicate the perturbations of biological recordings. Further showcasing the flexibility of the using *blended* systems. The CEF created could be used as an essential tool to create high throughput programs because of its convexity and ability to parallel the post hoc measurements. Since it was verified using different configurations, calculated mean, and variance of rhythmic characteristics, as well as recordings created from data augmentation. The form of data augmentation introduced can be generalized to other biological recordings or any time series really. With all these tools developed and expanding the parameter dimensions a hypothesis was posited that there is a contralateral electric synapse not previously included in the Melibe CPG model. Finally, I used the CEF on the hand-tuned *blended* systems and offered hypotheses of the deficiencies of each hand-tuned voltage time-series.

Our posited *blended* systems are built by connecting previously recorded and mathematical neurons. These systems can offer advantages in preliminary neuroscience research, specifically in the field of brain computer interface (BCI). Like *blended* systems BCIs interact with biological neurons, however instead of previously recorded neurons they connect to living ones. The most promising potential of BCI is their potential to restore vision, hearing, and locomotion. However, the current algorithms being developed do not capture the full picture of a biological neuron's qualitative voltage rhythmic activity.

To address this problem, we have created an error function that measures the difference in neural activity between the biological recording and mathematical time-series. We found that combining five functions via a weighted summation (CEF) results in a robust functionality that can differentiate between voltage time-series. Individually, these functions were shown to be insufficient to qualitatively mimic the target biological recording. The CEF we hypothesize should also give a perfect match if the CEF's value was zero.

Furthermore, because of the convex nature of the error function's parameter space, it can be used as the cost function in Artificial Neural Networks (ANN) to train a neural network to qualitatively mimic the voltage time series of a mathematical network with limited input parameters. We also used the error function to explore the likeness of a mathematical CPG that is driven by previously recorded biological CPG.

As mentioned in the previous section, the conductance parameters for the METs differed between the curare-bathed and normal biological CPG. The difference is not what we would expect to see since curare has no direct effect on non-cholinergic neurons and their synapses. However, since the curare *blended* system has very long inactive phases then the transitions from back and forth between inactive and active phases need not be immediate. In other words, the time series are more forgiving to weaker excitatory and inhibitory conductance. Therefore, the excitatory and inhibitory conductance parameters of the normal *blended* system should be expected and work on the curare *blended* system.

The error function described in this paper can offer developers of circuits that interact with biological neurons a more comprehensive error function. Ultimately, this can improve the automation of parameter optimization of mathematical neurons. However, the CEF can be

computationally expensive and further innovation in creating an error function could benefit the computational neuroscience field.

8 DATA AVAILABILITY

The error function code is available in GitHub repository (https://github.com/jbourahmahGSU/Voltage-recording-Error-function.git). An example of the blended system code that blends the *Melibe* recordings with the Si models neurons (https://github.com/jbourahmahGSU/Blended-System.git). Voltage recordings that were used are available upon request.

REFERENCES

[1] T Bal, F Nagy, and M Moulins. *The pyloric central pattern generator in crustacea: a set of conditional neuronal oscillators*. Journal of Comparative Physiology A,163 (6):715–727, 1988.

[2] E Marder and RL Calabrese. *Principles of rhythmic motor pattern generation*. Physiological reviews, 76 (3):687–717, 1996.

[3] A Selverston. Model neural networks and behavior. Springer Science & Business Media, 1985.

[4] RJ Calin-Jageman, MJ Tunstall, BD Mensh, and PS Katz, and WN Frost. *Parameter space analysis suggests multi-site plasticity contributes to motor pattern initiation in Tritonia*. Journal of Neurophysiology, 98 (4):2382– 2398, 2007.

[5] WN Frost and PS Katz. *Single neuron control over a complex motor program*. Proceedings of the National Academy of Sciences, 93 (1):422–426, 1996.

[6] PS Katz and SL Hooper. *Invertebrate central pattern generators*. Cold Spring Harbor Monograph Series, 49: 251, 2007.

[7] WB Kristan Jr, RL Calabrese, and WO Friesen. *Neuronal control of leech behavior*. Progress in neurobiology,76 (5):279–327, 2005.

[8] JM Newcomb, A Sakurai, JL Lillvis, CA Gunaratne, and PS Katz. *Homology and homoplasy of swimming behaviors and neural circuits in the Nudipleura (Mollusca, Gastropoda, Opisthobranchia)*. Proceedings of the National Academy of Sciences, 109 (Supplement 1):10669–10676, 2012.

[9] A Sakurai, JM Newcomb, JL Lillvis, and PS Katz. *Different roles for homologous interneurons in species exhibiting similar rhythmic behaviors*. Curr Biol, 21:1036, 2011.

[10] R Yuste, and JN MacLean, and J Smith, and A Lansner. *The cortex as a central pattern generator*. Nature Reviews Neuroscience, 6 (6):477–483, 2005.

[11] GP Krishnan, G Filatov, A Shilnikov, and M Bazhenov. *Electrogenic properties of the na+/k+ atpase control transitions between normal and pathological brain states*. Journal of neurophysiology, vol. 113, no. 9, pp. 3356–3374, 2015.

[12] M. Bazhenov, I. Timofeev, M. Steriade, and T. Sejnowski. *Spiking-bursting activity in the thalamic reticular nucleus initiates sequences of spindle oscillations in thalamic networks*. Journal of neurophysiology, vol. 84, no. 2, pp. 1076–1087, 2000.

[13] I. Timofeev, M. Bazhenov, T. Sejnowski, and M. Steriade, *Cortical hyperpolarization-activated depolarizing current takes part in the generation of focal paroxysmal activities*, Proceedings of the National Academy of Sciences, vol. 99, no. 14, pp. 9533–9537, 2002.

[14] TG Brown. *The intrinsic factors in the act of progression in the mammal*. Proceedings of the Royal Society of London. Series B, containing papers of a biological character, 84 (572):308–319, 1911.

[15] A. Hill, S. Van Hooser, and R. Calabrese, *Half-center oscillators underlying rhythmic movements*, The handbook of brain theory and neural networks (Arbib M, ed), pp. 507–510, 2003.

[16] S Grillner and P Wallen. *Central pattern generators for locomotion, with special reference to vertebrates*. Annual review of neuroscience, 8 (1):233–14261, 1985.

[17] R. M. Harris-Warrick, *Pattern generation*, Current opinion in neurobiology, vol. 3, no. 6, pp. 982–988, 1993.

[18] E. Marder, *Motor pattern generation*, Current opinion in neurobiology, vol. 10, no. 6, pp. 691–698, 2000.

[19] E. Marder and D. Bucher, *Central pattern generators and the control of rhythmic movements*, Current biology, vol. 11, no. 23, pp. R986–R996, 2001.

[20] E. Marder, D. Bucher, D. J. Schulz, and A. L. Taylor, *Invertebrate central pattern generation moves along*, Current Biology, vol. 15, no. 17, pp. R685–R699, 2005.

[21] Orlovsky, Grigori, T. G. Deliagina, and Sten Grillner, *Neuronal Control of Locomotion: From Mollusc to Man*, oxford university press, oxford, 1999. isbn 0198524056 (hbk), 322 pp." Clinical Neurophysiology, vol. 8, no. 111, pp. 1524–1525, 2000.

[22] A. I. Selverston and M. Moulins, *Oscillatory neural networks*, Annual review of physiology, vol. 47, no. 1, pp. 29–48, 1985.

[23] P. A. Getting, *Emerging principles governing the operation of neural networks*, Annual review of neuroscience, vol. 12, no. 1, pp. 185–204, 1989.

[24] O. Sporns and R. Kötter, "Motifs in brain networks," PLoS biology, vol. 2, no. 11, p. e369, 2004.

[25] J. P. Miller and A. I. Selverston, "Neural mechanisms for the production of the lobster pyloric motor pattern," in Model neural networks and behavior. Springer, 1985, pp. 37–48.

[26] WE Sherwood, R Harris-Warrick, J Guckenheimer. *Synaptic patterning of left-right alternation in a computational model of the rodent hindlimb central pattern generator*. Journal of computational neuroscience, 30 (2):323– 360, 2011.

[27] R. Milo, S. Shen-Orr, S. Itzkovitz, N. Kashtan, D. Chklovskii, and U. Alon, "Network motifs: simple building blocks of complex networks," Science, vol. 298, no. 5594, pp. 824–827, 2002.

[28] M. I. Rabinovich, P. Varona, A. I. Selverston, and H. D. Abarbanel, "Dynamical principles in neuroscience," Reviews of modern physics, vol. 78, no. 4, p. 1213, 2006.

[29] A. Bulloch and N. Syed, "Reconstruction of neuronal networks in culture," Trends in Neurosciences, vol. 15, no. 11, pp. 422–427, 1992.

[30] E. Marder, "Invertebrate neurobiology: Polymorphic neural networks," Current Biology, vol. 4, no. 8, pp. 752–754, 1994.

[31] P. S. Katz, "Evolution of central pattern generators and rhythmic behaviours," Philosophical Transactions of the Royal Society B, vol. 371, no. 1685, pp. 20 150 057– 20 150 057, 2016.

[32] D Alacam and AL Shilnikov. *Making a swim central pattern generator out of latent parabolic bursters*. International Journal of Bifurcation and Chaos, 25(07):1540003, 2015.

[33] S Jalil, D Allen, J Youker, and AL Shilnikov. *Toward robust phase-locking in Melibe swim central pattern generator models*. Chaos: An Interdisciplinary Journal of Nonlinear Science, 23 (4):3046105, 2013.

[34] A. Sakurai and P. Katz, "Distinct neural circuit architectures produce analogous rhythmic behaviors in related species," in Soc. Neurosci. Abstr, vol. 37, no. 04, 2011.

[35] A Sakurai, CA Gunaratne, and PS Katz. *Two interconnected kernels of reciprocally inhibitory interneurons underlie alternating left-right swim motor pattern generation in the mollusk Melibe leonina*. Journal of neurophysiology, 112 (6):1317–1328, 2014.

[36] P. S. Katz, “Comparison of extrinsic and intrinsic neuromodulation in two central pattern generator circuits in invertebrates,” Experimental Physiology, vol. 83, no. 3, pp. 281–292, 1998.

[37] J Best, A Borisyuk, J Rubin, D Terman, and M Wechselberger. *The dynamic range of bursting in a model respiratory pacemaker network*. SIAM Journal on Applied Dynamical Systems, 4 (4):1107–1139, 2005.

[38] I Belykh and AL Shilnikov. *When weak inhibition synchronizes strongly desynchronizing networks of bursting neurons*. Physical review letters, 101 (7):078102, 2008.

[39] H Koch, AJ Garcia III, and JM Ramirez. *Network reconfiguration and neuronal plasticity in rhythm-generating networks*. Oxford University Press, 2011.

[40] RL Calabrese, BJ Norris, A Wenning, TM Wright. *Coping with variability in small neuronal networks*. Oxford University Press E, 2011.

[41] E Marder. *Neuromodulation of neuronal circuits: back to the future*. Neuron, 76 (1):1-11, 2012.

[42] A. Sakurai and P. S. Katz, “Artificial synaptic rewiring demonstrates that distinct neural circuit configurations underlie homologous behaviors,” Current Biology, vol. 27, no. 12, pp. 1721–1734, 2017.

[43] WB Kristan. *Neuronal decision-making circuits*. Current Biology, 18 (19):R928–R932, 2008.

[44] KL Briggman and WB Kristan Jr. *Multifunctional pattern-generating circuits*. Annu. Rev. Neurosci., 31:271–294, 2008.

[45] J Wojcik, JTC Schwabedal, R Clewley, and AL Shilnikov. *Key bifurcations of bursting polyrhythms in 3-cell central pattern generators*. PloS one, 9 (4), 2014.

[46] A. Lundberg, “Half-centres revisited,” in Regulatory Functions of the CNS Principles of Motion and Organization. Elsevier, 1981, pp. 155–167.

[47] J. Gjorgjieva, D. Biron, and G. Haspel, “Neurobiology of caenorhabditis elegans locomotion: where do we stand?” Bioscience, vol. 64, no. 6, pp. 476–486, 2014.

[48] J. T. Buchanan, “Commissural interneurons in rhythm generation and intersegmental coupling in the lamprey spinal cord,” Journal of Neurophysiology, vol. 81, no. 5, pp. 2037–2045, 1999.

[49] Y. Arshavsky, T. Deliagina, G. Orlovsky, Y. Panchin, G. Pavlova, and L. Popova, “Control of locomotion in marine mollusc clione limacina. vi. activity of isolated neurons of pedal ganglia.” Experimental brain research, vol. 63, no. 1, pp. 106–112, 1986.

[50] XJ Wang and J Rinzel. *Alternating and synchronous rhythms in reciprocally inhibitory model neurons*. J. Neural Computation, 4 (1):84–97, 1992.

[51] F Skinner, N Kopell, and E Marder. *Mechanisms for oscillation and frequency control in networks of mutually inhibitory relaxation oscillators*. J. Comput. Neurosci, 1:69–87, 1994.

[52] S. Daun, J. E. Rubin, and I. A. Rybak, “Control of oscillation periods and phase durations in half-center central pattern generators: a comparative mechanistic analysis,” Journal of computational neuroscience, vol. 27, no. 1, p. 3, 2009.

[53] C. Zhang and T. J. Lewis, “Phase response properties of half-center oscillators,” Journal of computational neuroscience, vol. 35, no. 1, pp. 55–74, 2013.

[54] J. E. Rubin, N. A. Shevtsova, G. B. Ermentrout, J. C. Smith, and I. A. Rybak, “Multiple rhythmic states in a model of the respiratory cpg.”

[55] J Rubin and D Terman. *Geometric analysis of population rhythms in synaptically coupled neuronal networks*. Neural computation, 12 (3):597–645, 2000.

[56] FK Skinner, L Zhang, JL Velazquez, and PL Carlen. *Bursting in inhibitory interneuronal networks: a role for gap-junctional coupling*. Journal of neurophysiology, 81 (3):1274–1283, 1999.

[57] A. Sakurai and P. S. Katz, “The central pattern generator underlying swimming in dendronotus iris: a simple half-center network oscillator with a twist,” Journal of neurophysiology, vol. 116, no. 4, pp. 1728–1742, 2016.

[58] H. Ju, "Principles for Making Half-center Oscillators and Rules for Torus Bifurcation in Neuron Models." Dissertation, Georgia State University, 2020.

[59] S Jalil, I Belykh, and AL Shilnikov. *Fast reciprocal inhibition can synchronize bursting neurons*. Physical Review E, 81 (4):045201, 2010.

[60] S Jalil, I Belykh, and AL Shilnikov. *Spikes matter in phase-locking of inhibitory bursting networks*. Physical Review E, 85:36214, 2012.

[61] D Perkel and B Mulloney. *Mechanism of postinhibitory rebound in molluscan neurons*. Science, 185 (4146):181–183, 1974.

[62] JD Angstadt, JL Grassmann, KM Theriault, and SM Levasseur. *Mechanisms of postinhibitory rebound and its modulation by serotonin in excitatory swim motor neurons of the medicinal leech*. Journal of comparative physiology A, 191 (8):715–732, 2005.

[63] N Kopell and GB Ermentrout. *Mechanisms of phase-locking and frequency control in pairs of coupled neural oscillators*. Handbook of dynamical systems, 2:3–54, 2002.

[64] Katz, Paul, Sten Grillner, Rachel Wilson, Alexander Borst, Ralph Greenspan, György Buzsáki, Kevan Martin, Eve Marder, William Kristan, and Rainer Friedrich. "Vertebrate versus invertebrate neural circuits." (2013): R504-R506.

[65] Alacam, Deniz, "Modeling Rhythm Generation in Swim Central Pattern Generator of Melibe Leonina." Dissertation, Georgia State University, 2017.

[66] Katz, Paul S. "Neuromodulation Intrinsic to the Central Pattern Generator for Escape Swimming in Tritonia a." *Annals of the New York Academy of Sciences* 860.1 (1998): 181-188.

[67] Sasaki, Kosei, et al. "Feeding CPG in Aplysia directly controls two distinct outputs of a compartmentalized interneuron that functions as a CPG element." *Journal of Neurophysiology* 98.6 (2007): 3796-3801.

[68] Spencer, Gaynor E., et al. "Changes in the activity of a CPG neuron after the reinforcement of an operantly conditioned behavior in Lymnaea." *Journal of Neurophysiology* 88.4 (2002): 1915-1923.

[69] S. Thompson and W. Watson, “Central pattern generator for swimming in melibe,” J. Exp. Biol., vol. 208, no. 7, p. 1347, 2005.

[70] E. Bullmore and O. Sporns, “Complex brain networks: graph theoretical analysis of structural and functional systems,” Nature Reviews Neuroscience, vol. 10, no. 3, p. 186, 2009.

[71] F. Azam, “Biologically inspired modular neural networks,” Ph.D. dissertation, Virginia Tech, 2000.

[72] D. Meunier, R. Lambiotte, and E. T. Bullmore, “Modular and hierarchically modular organization of brain networks,” Frontiers in neuroscience, vol. 4, p. 200, 2010.

[73] AL Shilnikov, R Gordon, I Belykh. *Polyrhythmic synchronization in bursting networking motifs*. Chaos: An Interdisciplinary Journal of Nonlinear Science, 18 (3):037120, 2008.

[74] J Wojcik, R Clewley, and AL Shilnikov. *Order parameter for bursting polyrhythms in multifunctional central pattern generators*. Physical Review E, 83 (5):056209, 2011.

[75] JTC Schwabedal, AB Neiman, and AL Shilnikov. *Robust design of polyrhythmic neural circuits*. Physical Review E, 90 (2):022715, 2014.

[76] JTC Schwabedal, DE Knapper, and AL Shilnikov. *Qualitative and quantitative stability analysis of penta-rhythmic circuits*. Nonlinearity, 29 (12):3647, 2016.

[77] AA Prinz, D Bucher, and E Marder. *Similar network activity from disparate circuit parameters*. Nature Neuroscience, 7 (12):1345–1352, 2004.

[78] AA Prinz, V Thirumalai, and E Marder. *The functional consequences of changes in the strength and duration of synaptic inputs to oscillatory neurons*. Journal of Neuroscience, 23 (3):943–954, 2003.

[79] Pusuluri, Krishna, "Complex Dynamics in Dedicated / Multifunctional Neural Networks and Chaotic Nonlinear Systems." Dissertation, Georgia State University, 2020.

[80] C Van Vreeswijk, LF Abbott, and GB Ermentrout. *When inhibition not excitation synchronizes neural firing*. Journal of computational neuroscience,1 (4):313–321, 1994.

[81] J Scully, JNH Bourahmah, D Bloom, and AL Shilnikov. *Pairing cellular and synaptic dynamics into building blocks of rhythmic neural circuits*. submitted for publication.

[82] K Matsuoka. *Mechanisms of frequency and pattern control in the neural rhythm generators*. Biological cybernetics, 56 (5-6):345–353, 1987.

[83] RO Dror, CC Canavier, RL Butera, JW Clark, and JH Byrne. *A mathematical criterion based on phase response curves for stability in a ring of coupled oscillators*. Biological cybernetics, 80 (1):11–23, 1999.

[84] CC Canavier, DA Baxter, JW Clark, and JH Byrne. *Multiple modes of activity in a model neuron suggest a novel mechanism for the effects of neuromodulators*. Journal of Neurophysiology, 72 (2):872–882, 1994.

[85] AA Prinz, and CP Billimoria, and E Marder. *Alternative to hand-tuning conductance-based models: construction and analysis of databases of model neurons*. Journal of neurophysiology, 90 (6):3998–4015, 2003.

[86] N Kopell and B Ermentrout. *Chemical and electrical synapses perform complementary roles in the synchronization of interneuronal networks*. Proceedings of the National Academy of Sciences, 101 (43):15482–15487, 2004.

[87] M Hagglund, KJ Dougherty, L Borgius, S Itohara, T Iwasato, and O Kiehn. *Optogenetic dissection reveals multiple rhythmogenic modules underlying locomotion*. Proceedings of the National Academy of Sciences, 110 (28):11589-11594, 2013.

[88] RE Plant. *Bifurcation and resonance in a model for bursting nerve cells*. Journal of mathematical biology, 11 (1):15–32, 1981.

[89] RE Plant and M Kim. *Mathematical description of a bursting pacemaker neuron by a modification of the Hodgkin-Huxley equations*. Biophysical journal, 16 (3):227–244, 1976.

[90] RE Plant and M Kim. *On the mechanism underlying bursting in the Aplysia abdominal ganglion R15 cell*. Mathematical Biosciences, 26 (3-4):357–375, 1975.

[91] ES Levitan and IB Levitan. *Serotonin acting via cyclic AMP enhances both the hyperpolarizing and depolarizing phases of bursting pacemaker activity in the Aplysia neuron R15*. Journal of Neuroscience, 8 (4):1152–1161, 1988.

[92] C. Canavier, J. Clark, and J. Byrne, "Simulation of the bursting activity of neuron R15 in aplysia: Role of ionic currents, calcium balance, and modulatory transmitters," J Neurophysiology, vol. 66, no. 6, pp. 2107–2124., 1991.

[93] R. Bertran, "A computational study of the effects of serotonin on a molluscan burster neuron," Biol. Cybern., vol. 69, pp. 257–267, 1993.

[94] R. Butera, J. W. J. Clark, C. C. Canavier, D. A. Baxter, and J. H. Byrne, "Analysis of the effects of modulatory agents on a modeled bursting neuron: Dynamic interactions between voltage and calcium dependent systems," J Comput Neurosci., vol. 2, no. 1, pp. 19–44, 1995.

[95] R. Butera, "Multirhythmic bursting," Chaos, vol. 8, no. 1, pp. 274–284, 1998.

[96] F. Sieling and R. Butera, "Aplysia R15 neuron," Scholarpedia, vol. 6, no. 10, p. 4181, 2011.

[97] L. Ji, J. Zhang, X. Lang, and X. Zhang, "Coupling and noise induced spiking-bursting transition in a parabolic bursting model," Chaos: An Interdisciplinary Journal of Nonlinear Science, vol. 23, no. 1, p. 013141, 2013.

[98] MH Hennig. *Modelling Synaptic Transmission*. ANC, Informatics, University of Edinburgh, 2008.

APPENDICES

Appendix A

The governing equation of the Si model neuron derived by Kirchhoff's Current Law and is the Hodgkin-Huxley model with additional currents,

$$C_m \frac{dV}{dt} = -I_I - I_K - I_h - I_{KCa} - I_T - I_{leak} - \Sigma I_{syn}.$$

The Hodgkin-Huxley (HH) model describes the currents across the neuronal membrane through different channels, including an inward sodium (Na+) and calcium (Ca2+) current (I_I),

$$I_I = g_I m_\infty^3 h(V - E_I),$$

where E_I =30mV for the reversal potential and g_I= 4nS for its maximal conductance, and the gating variable is

$$m_\infty(V) = \frac{\alpha_m(V)}{\alpha_m(V) + \beta_m(V)},$$

$$\alpha_m(V) = 0.1\frac{50 - V_s}{1 + e^{(50-V_s)/10}}, \quad \beta_m(V) = 4e^{(25-V_s)/18}.$$

The h variable is defined as

$$\frac{dh}{dt} = \frac{h_\infty(V) - h}{\tau_n(V)},$$

$$h_\infty(V) = \frac{\alpha_h(V)}{\alpha_h(V) + \beta_h(V)} \quad \text{and} \quad \tau_h(V) = \frac{12.5}{\alpha_h(V) + \beta_h(V)},$$

$$\alpha_h(V) = 0.07e^{(25-V_s)/20}, \quad \text{and} \quad \beta_h(V) = \frac{1}{1 + e^{(55-V_s)/10}},$$

$$V_s = \frac{127V + 8265}{105}.$$

The next current in the HH potassium (K+) current (I_K),

$$I_k = g_k n^4(V - E_k),$$

$$\frac{dn}{dt} = \frac{n_\infty(V) - n}{\tau_n(V)}, \quad n_\infty(V) = \frac{\alpha_n(V)}{\alpha_n(V) + \beta_n(V)},$$

$$\tau_n(V) = \frac{12.5}{\alpha_n(V) + \beta_n(V)}$$

$$\alpha_n(V) = 0.01\frac{55 - V_s}{e^{(55-V_s)/10} - 1}, \quad \beta_n(V) = 0.125e^{(45-V_s)/80},$$

where E_K =-75mV for the reversal potential and g_K= 0.3nS.

The additional currents of the Si model are the slow TTX-resistant sodium-calcium current (I_T),

$$I_T = g_T x(V - E_I)$$

where E_I =30mV for the reversal potential and g_T= 4nS for the maximal conductance, and the activation variable being

$$\frac{dx}{dt} = \frac{x_\infty(V + \Delta_x) - x}{\tau_x},$$

$$x_\infty(V) = \frac{1}{1 + e^{-0.15(V+50-\Delta_x)}},$$

with the time constant τ_x= 100 ms. The second added current is the outward calcium dependent potassium current (I_{KCa}),

$$I_{KCa} = g_{KCa}\frac{Ca}{Ca + 0.5}(V - E_K),$$

where E_K =-75mV for the reversal potential and g_{KCa}= 0.03nS for the maximal conductance and

$$\frac{dCa}{dt} = \rho[K_c\, x\, (E_{Ca} - V + \Delta_{Ca}) - Ca],$$

with ρ=0.00015ms^{-1} and K_c=0.00425mV^{-1}.

leak current (I_{leak}),

$$I_{leak} = g_L(V - E_L),$$

Next, is the hyperpolarized-activated depolarizing h-current (I_h), with E_h =70mV for the reversal potential and g_h= 0.0006nS for the maximal conductance

$$\mathrm{I_h} = \mathrm{g_h}\frac{\mathrm{y(V-E_h)}}{(1+\mathrm{e}^{-(\mathrm{V-63})/7.8})^3},$$

and the activation variable being

$$\frac{\mathrm{dy}}{\mathrm{dt}} = \mathrm{g_h}\frac{\mathrm{y(V-E_h)}}{(1+\mathrm{e}^{-(\mathrm{V-63})/7.8})^3}.$$

and synaptic current (I_{syn}), from another neuron

$$\mathrm{I_{syn}} = \mathrm{g_{syn}S(V_{post}-E_{rev})},$$

with S being governed by

$$\frac{\mathrm{dS}}{\mathrm{dt}} = \frac{\alpha(1-\mathrm{S})}{1+\mathrm{e}^{-\mathrm{k(V_{pre}-V_{th})}}} - \beta\mathrm{S}.$$

Appendix A.1

The square root of the sum of squares (SRSS):

$$||\mathrm{X}|| = \sqrt{\sum_{\mathrm{i=1}}^{\mathrm{N}} |\mathrm{X_i}|^2}.$$

Formulas of the error functions:

Spike count difference, where m is the number of spikes of either the biological voltage recording or the that of the model neuron,

$$\Delta_{\mathrm{spikes}} = \left|\mathrm{m}_{\mathrm{spike}}^{\mathrm{bio}} - \mathrm{m}_{\mathrm{spike}}^{\mathrm{mod}}\right|,$$

Synaptic distance, where the SRSS of the difference between the biological voltage recording S variable and the model neuron are taken,

$$||S||_2 = \sqrt{\sum_{i=1}^{N} \left(S_i^{bio} - S_i^{mod}\right)^2},$$

Voltage moving average distance, where the SRSS of the difference between the moving average of the biological voltage recording and the model neuron are taken,

$$||\widehat{V}|| = \sqrt{\sum_{i=1}^{N} \left(\widehat{V}_i^{bio} - \widehat{V}_i^{mod}\right)^2},$$

With the moving average of the voltage is defined as,

$$\widehat{V} = \frac{1}{k} \sum_{i=N-k+1}^{N} V_i,$$

Variance of the difference in the moving average, with μ being the mean of $\left|\widehat{V}_i^{bio} - \widehat{V}_i^{mod}\right|$

$$s^2 = \frac{1}{N-1} \sqrt{\sum_{i=1}^{N} \left(\left|\widehat{V}_i^{bio} - \widehat{V}_i^{mod}\right| - \mu\right)^2},$$

Sigmoidal of the envelope distance

$$||E|| = f_\sigma(||L|| + ||U||);$$

SRSS of the lower envelopes difference

$$||L||_2 = \sqrt{\sum_{i=1}^{N} \left(L_i^{bio} - L_i^{mod}\right)^2},$$

SRSS of the upper envelopes difference

$$||U||_2 = \sqrt{\sum_{i=1}^{N} \left(U_i^{bio} - U_i^{mod}\right)^2},$$

And the sigmoidal function used

$$f_{\sigma}(x) = \left(1 + e^{(-a(x-c))}\right)^{-1}.$$

The weighted sum used for the combination of the error functions into a combined error function

$$WS = w_1 \Delta_{spikes} + w_2|S| + w_3|\widehat{V}| + w_4 s^2 + w_5|E|,$$

Where w_1= 0.10, w_2= 0.58, w_3= 0.10, w_4= 0.19, w_5= 0.03.